Measurement Technology for Micro-Scale Aerodynamics

by

Michael James Martin

A dissertation submitted in partial fulfillment
of the requirements for the degree of
Doctor of Philosophy
(Aerospace Engineering)
in The University of Michigan
2007

Doctoral Committee:

Associate Professor Luis P. Bernal, Co-Chair
Professor Iain D. Boyd, Co-Chair
Associate Professor Katsuo Kurabayashi
Associate Professor Peter D. Washabaugh

For my parents

Acknowledgements

I would like to begin by thanking Professor Boyd for his guidance, and his patience, during my graduate career at Michigan. Much of what got accomplished in this thesis was a result of his willingness to let me take work into areas outside of the original scope of the research, while insisting that it remain relevant to engineering problems. I hope that this work repays his trust that something was getting accomplished during periods of the thesis where no immediate results were emerging

The rest of the committee also played key roles in this thesis. Professor Bernal was an early participant in this work. Without his generous guidance through experimental design, it is unlikely that this work would have gone from theoretical to practical. Professor Kurabayashi provided a valuable introduction to micro-systems design. Professor Washabaugh's impact on this thesis began when I was a teaching assistant for his instrumentation class, an experience that sharpened my thinking on experimental measurement.

Other members of the research group have been extremely helpful over the course of my time in Michigan, providing sound advice on everything from paper formatting to automotive repair. Dr. Quanhua Sun, my former officemate, and the "late-night crew" of Justin Koo, Matt McNenly, and Anton Vanderwyst seem to have born much of the load, but thanks go out to Dave Berger, Jeremy Boerner, Jon Burt, Dr. Chunpei Cai, Yungjun Choi, Dr. Jerry Emhoff, Andrew Lofthouse, Jose Padilla, Andy Porwitzky, Leo Scalabrin,

Tom Schwartzentruber, and John Yim. Dr. (now Professor) Andrew Christlieb also provided useful advice on the numerics in Chapter 2. Additional late night (or mid-day) moral support came from my office mates, Dr. Mitchell Walker, Rob Lobia, Tom Liu, and Kristina Lemmer.

Device fabrication required training and advice from numerous individuals in the Michigan Nanofabrication Facility. I apologize in advance if I have neglected anyone, or failed to properly identify the source of advice behind the clean-room mask. Rob White, my clean-room mentor, was incredibly helpful, taking time away from his thesis work to show me the ropes. All of the staff was helpful, but Katherine Beach, Aaron Glatzer, Ning Gulari, Cedric Whitney, and Bill Knudsen were actively involved in making my process work. An extra thanks goes out to Brian VanDerElzen, for not throwing me out of the MNF the umpteenth time my wafers broke in the STS. Finally, Linda Chow, Tim Lin, Helena Chan, Jing Wang, Juinbai Wang, Tim Harpster, Chao Fan, and numerous others provided both advice, and good company while waiting for long processes to finish.

Making the micro-scale tunnel work required the skills of numerous individuals within the aerospace engineering department. Terry Larrow, the departmental machinist, worked miracles in getting metal to form into the contraction section of the tunnel, and then to produce the nylon test section. Dave McLean provided valuable assistance in getting the electronics working. Tom Griffin, Eric Kirk, and Chris Chartier were extremely helpful in getting the vacuum system connected and operational. Finally, Mike Muller and John Mullin provided valuable advice on taking measurements at small scales. Li Liu was generous in helping untangle the mysteries of structural analysis.

A huge thanks goes out to the administrative staff of the Aerospace Engineering department for their help in navigating the University of Michigan bureaucracy. While few could ever hope to match the vast skill and experience Margaret Fillion acquired in guiding graduate students through red tape, Denise Phelps has definitely done her share in making grad student life easier. Sharon Baurle, Cindy Collins, Heidi DiVirglio, Cynthia Enoch, Denny Laird, Michelle Shepard, Suzanne Smith, and Lisa Szuma have all been extremely helpful at one time or another in the process.

Finally, my family and friends have been extremely supportive throughout my time in graduate school. Thanks, mom, dad, Dan, Chris, and Mary.

Table of Contents

List of Figures

List of Tables

List of Symbols

A	Beam Cross-Sectional Area
A_{ij}	Coefficient ij of response matrix for resistor A
a	Iteration Coefficient
B_{ij}	Coefficient ij of response matrix for resistor B
b	Iteration Coefficient
C	Wind Tunnel Contraction Ratio
C_D	Drag Force
c_p	Specific Heat
c	Airfoil chord
D	Diameter of turbulence suppression honeycomb
E	Elastic Modulus
F_D	Drag Force
F_X	Force in x-direction
F_Y	Force in y-direction
f	Force per unit length
f	Non-dimensional Stream function
G	Shear Elastic Modulus
G	Amplifier Gain
h	Wind tunnel height
I_x	Moment of Inertia about the x-axis
I_y	Moment of Inertia about the y-axis
K_1	Non-equilibrium parameter based on boundary-layer scaling
Kn	Knudsen Number
Kn_x	Knudsen Number based on x
Kn_δ	Knudsen Number based on boundary layer thickness δ
L	Length
L_A	Length of sensor A
L_B	Length of sensor B

L_W	Length of airfoil mounting region
J	Polar Moment of Intertia
M_Z	Torque per length about the z-axis
Nu	Nusselt Number
Nu_x	Nusselt number based on x
P	Static Pressure
P	Power
Pr	Prandtl Number
q’	Turbulent velocity fluctuation
R	Ideal Gas Constant
R	Electrical Resistance
Re	Reynolds Number
Re_c	Reynolds Number based on chord c
Re_h	Reynolds Number based on tunnel height h
Re_x	Reynolds Number based on x
Re_δ	Reynolds Number based on boundary layer thickness δ
S_{ij}	Coefficient ij of sensitivity matrix S
T	Temperature
T_D	Thickness of device layer of SOI wafer
T_g	Temperature of gas
T_H	Thickness of oxide layer of SOI wafer
T_{OX}	Thickness of handle layer of SOI wafer
T_w	Wall temperature
T_∞	Free-stream temperature
T*	Non-dimensional temperature
t	Thickness
u	Velocity in the x-direction
u’	Turbulent velocity fluctuation in the x-direction
u_{gas}	Velocity of gas at wall interface

u_o	Free-stream velocity in the x-direction
u_{slip}	Slip velocity at wall
u_{wall}	Wall velocity
u*	Non-dimensional velocity in the x-direction
$\bar{u}$	Average x-velocity in tunnel test section
V	Voltage
V'	RMS Voltage Fluctuation
$V(noise)'_{rms}$	RMS Voltage Fluctuation resulting from electrical noise
$V(turb)'_{rms}$	RMS Voltage Fluctuation resulting from fluid turbulence noise
v	Velocity in the y-direction
u'	Turbulent velocity fluctuation in the y-direction
v*	Non-dimensional velocity in the y-direction
w	Width
W_A	Width of sensor A
W_B	Width of sensor B
w'	Turbulent velocity fluctuation in the z-direction
x*	Non-dimensional coordinate in the x-direction
y	Non-dimensional coordinate in the y-direction
α	Thermal conductivity
β	Combined Knudsen Number and Tangential Momentum Accommodation Coefficient
ΔP	Dynamic Pressure
$\Delta\rho_x$	Change in electrical resistivity in the x-direction
$\Delta\rho_y$	Change in electrical resistivity in the y-direction
$\Delta\rho_z$	Change in electrical resistivity in the z-direction
$\Delta\rho_{xy}$	Change in electrical cross-resistivity in the xy-direction
$\Delta\rho_{xz}$	Change in electrical cross-resistivity in the xz-direction
$\Delta\rho_{yz}$	Change in electrical cross-resistivity in the yz-direction
δ	Boundary layer thickness
δ*	Boundary layer displacement thickness

ε	Experimental Uncertainty
η	Non-dimensional y coordinate
η_{99}	Non-dimensional boundary layer thickness
θ	Boundary layer momentum thickness
λ	Mean Free Path of gas
μ	Viscosity
π_{ij}	Component ij of the piezoresistive matrix
ρ	Density of gas
ρ_x	Electrical resistivity in the x-direction
ρ_y	Electrical resistivity in the y-direction
ρ_z	Electrical resistivity in the z-direction
ρ_{xy}	Electrical cross-resistivity in the xy-direction
ρ_{xz}	Electrical cross-resistivity in the xz-direction
ρ_{yz}	Electrical cross-resistivity in the yz-direction
σ	Tangential Momentum Accommodation Coefficient
σ_{max}	Maximum stress
σ_{crit}	Critical beam stress for buckling
σ_{xx}	Compressive stress in the x-direction
σ_{yy}	Compressive stress in the y-direction
σ_{zz}	Compressive stress in the z-direction
τ_{wall}	Shear stress at wall
τ_{xy}	Shear stress in the x-y plane
τ_{xz}	Shear stress in the x-z plane
τ_{yz}	Shear stress in the y-z plane
υ	Kinematic Viscosity
Φ	Beam Angle of Twist
Ψ	Stream Function
ω	Natural Frequency

CHAPTER 1

GAS FLOW FOR MICRO-FLIGHT: PREVIOUS WORK

1.1. Introduction

As micro-systems technology improves, there is a growing interest in building flying machines using micro-and nano-technology (McMichael, 1997). Technologies such as micro-propulsion (Bayt, 1999) and micro-power (Epstein, 1997) systems may make this technology feasible. Micro-scale flyers would have applications for military battlefield surveillance, as well as search-and-rescue operations. However, while many of the component technologies are under development, the fluid mechanics at these scales is not well understood. This limits the ability to design flying devices at length scales of millimeters and below.

The flow regime in which nano-fliers will exist is a low-Reynolds number, and possibly high Knudsen number, region. This means that low-Reynolds number effects may exist alongside continuum breakdown. While non-equilibrium effects have been studied in micro-system applications such as micro-channels (Arkilic, 1997), and gas bearings (Frechette, 2000), it is not clear how much of this work scales to external flow applications such as micro-flight.

Even without considering non-equilibrium effects, flight at these scales is not well understood. Reviews of previous work on insect flight (Wang, 2005) shows that study at these scales has been limited by the lack of appropriate experimental methods.

Computational efforts have been limited by difficulty in identifying the correct physical models to use for biological flight.

Therefore, preparing to study aerodynamics at the micro- and nano- scales will require review of two separate fields of fluid mechanics investigation: rarefied flows in microsystems, and insect flight. This chapter will review previous work in these areas.

1.2. Rarefied Slip Flows at the Micro-scale: Early Work

The experimental study of rarefied flows begins with a study in 1875 by Kundt and Warburg, physicists at Kaiser Wilhelm University, who studied the damping in air of a vibrating disk, and discovered that the measured damping decreased at low pressures. Adopting an idea popular at the time in research of liquid flows, they ascribed the decreased damping to slip at the boundary between the disk and the gas. (Knudt, 1876)

Kundt and Warburg then modeled the slip as being equal to a coefficient of slip multiplied by the gradient of velocity at the wall. They then observed that the slip coefficient was inversely proportional to the pressure of the gas. The first calculations of mean free path had been made about 20 years earlier (Clasius, 1857), which allowed Kundt and Warburg to appreciate that the slip coefficient was directly proportional to the mean free path of the gas.

These results were then confirmed by the creation of a model for slip flow based on kinetic theory by James Clerk Maxwell, the 19th century Scottish physicist (Maxwell, 1879). The equation Maxwell obtained showed that the slip depended upon the velocity gradient normal to the wall $\partial u/\partial n$, the mean free path of the gas λ, and a tangential momentum accommodation coefficient σ, intended to model the collision of the gas molecule with the wall. An accommodation coefficient of 1 represented full

accommodation, also termed diffuse reflection, in which the molecules were "absorbed" into the wall, and then ejected at a random direction at the temperature of the wall. An accommodation coefficient of 0 represented the opposite extreme, termed specular reflection, in which the molecules bounce directly off of the wall retaining all of their tangential momentum and kinetic energy. A value in between suggested that a portion of the molecules were fully accommodated, with the remainder reflected specularly off the wall. Maxwell then added a second term, to account for thermal transpiration, or the tendency of gas molecules to creep from cold to hot along a wall with a temperature gradient. This term took into account the density of the fluid ρ, the viscosity of the fluid μ, and the temperature of the gas T_g, and the temperature gradient along the wall. The resulting equation has remained in use for first-order analysis of slip flows ever since:

$$u_{slip} = u_{gas} - u_{wall} = \lambda \frac{2-\sigma}{\sigma} \left. \frac{\partial u}{\partial n} \right|_{wall} + \frac{3}{4} \frac{\mu}{\rho T_g} \left. \frac{\partial T}{\partial s} \right|_{wall} \tag{1.1}$$

Additional experimental confirmation of this came first from the work of Knudsen, who measured the flow of hydrogen, oxygen, and carbon dioxide through circular glass tubes (Knudsen, 1909) and Gaede, who performed similar experiments using hydrogen and nitrogen (Gaede, 1913). Knudsen also went on to characterize the flow around spheres, while Gadsen attempted to characterize the flow between two flat plates.

A key result of this work was the characterization of flow regimes, using what was later named the Knudsen number in Knudsen's honor. This non-dimensional number is the ratio of the mean free path of the gas to the characteristic length scale of the flow, and can be used to characterize the importance of non-equilibrium effects:

$$Kn = \lambda / L \tag{1.2}$$

Because Knudsen performed his experiments in internal geometries, where the diameter of the channel was also proportional to the gradient length scale of the flow, the diameter of the channel was usually the characteristic length scale of the flow. More recent work suggested that for external flow geometries, a boundary layer thickness, or other gradient length scale, was appropriate. (Schaaf, 1954)

Later research expanded these results to characterize four distinct flow regimes based on Knudsen number, as given in table 1 below (Karniadakis, 2002). In all cases, the equations used for rarefied flow regimes are valid for lower Knudsen number, or less rarefied, regimes.

Knudsen Number Range	Flow Regime	Governing Equations
$Kn \leq .01$	Continuum Flow	Navier Stokes Equations with No-slip BC
$0.1 \leq Kn \leq .01$	Slip Flow	Navier Stokes Equations with Slip BC
$10 \leq Kn \leq 0.1$	Transition Flow	Burnett Equations ($Kn < 0.5$) Boltzmann Equation
$Kn \geq 10$	Free Molecular Flow	Boltzmann Equation

Table 1.1. Flow Regimes based on Knudsen Number

A second application of the Knudsen number comes in non-dimensionalization of the boundary conditions. If thermal transpiration is disregarded, this term could also be successfully used in non-dimensionalizing equation (1.1), just as Reynolds number is often used to non-dimensionalize the Navier-Stokes equations:

$$u^*_{slip} = Kn\frac{2-\sigma}{\sigma}\left.\frac{\partial u^*}{\partial n^*}\right|_{wall} = \beta\left.\frac{\partial u^*}{\partial n^*}\right|_{wall} \tag{1.3}$$

where u^* is u divided by the characteristic velocity of the flow, and n^* is the distance from the wall in the tangential direction normalized by the mean free path. Because the

Knudsen number term and the accommodation coefficients both appear in the slip coefficient, they are sometimes simply combined into the single coefficient β.

Additional experimental work (Timiriazeff, 1913, Millikan, 1923) focused on measuring rarefied flow between two coaxial cylinders, with the outer cylinder rotating. Measuring the torque on the inner cylinder allowed determination of the shear stress, just as in a conventional viscometer. Measuring the deviation from the continuum model for shear stress then allowed determination of the coefficient of accommodation for various gas/solid combinations. These supplemented the measurements of accommodation coefficients that could be found from Knudsen's work.

The results of Kundt, Warburg, Maxwell, Knudsen, Gadsen, Timiriazeff, and Millikan, while physically extremely interesting, fell under the category of pure physical research instead of engineering. Fundamentally, they represent part of an attempt to understand how gases, while composed of discrete molecules, could be modeled as a continuum. When combined with the development of modern kinetic theory, in the works of Maxwell and Boltzmann, they created a framework for connecting the molecular nature of gases with the large-scale behavior.

Rarefied gas dynamics became a field of engineering interest with the coming of the space age. The need to understand the behavior of spacecraft in the upper atmosphere led to the development of a large body of work on rarefied gas dynamics, including the development of a numerical method for simulating the Boltzmann equation, the direct simulation Monte Carlo, or DSMC, method. The work done during this period focused mainly on high Reynolds number, and high Mach number, flows, instead of the low speed flows studied by earlier researchers. (Bird, 1994)

One set of experimental measurements with potential value for microflight as a study of drag on a flat plate in a vacuum tunnel conducted by Schaaf and Sherman (Schaaf, 1954.) Schaaf and Sherman measured the drag on flat plates at high-vacuum conditions. This work showed that there was an experimentally detectable change in the drag force on an airfoil at transitional Knudsen numbers. The results suggested that drag increased in rarefied flows at low Reynolds numbers, and increased at higher Reynolds numbers. While most of their data was taken at supersonic flow conditions, the Knudsen and Reynolds number values of their subsonic measurements are plotted in figure 1.1.

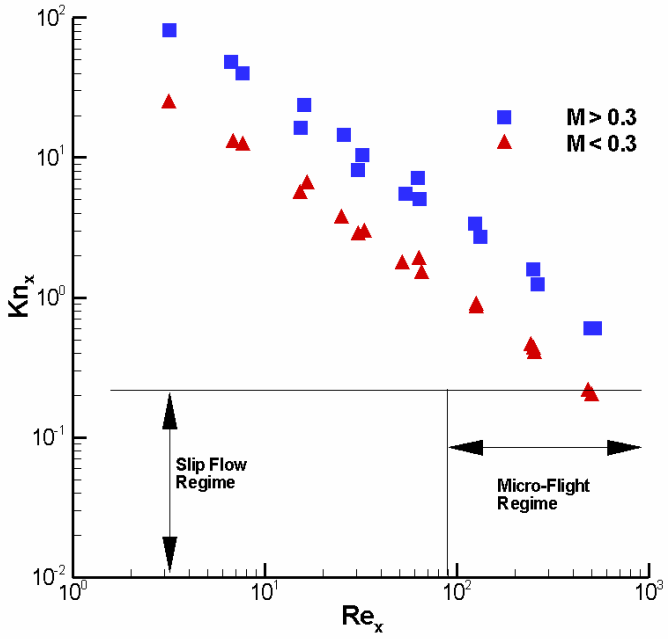

Figure 1.1. Knudsen versus Reynolds Number Values for Slip-Flow Measurements over a Flat Plate

There are two limitations to using this data to determine the limits of contiunuum theory for micro-flight. The first is that the data barely includes the slip flow regime. The second limitation is that it is impossible to separate out Reynolds number and Knudsen number effects within this data, since the Reynolds number and Knudsen number do not

seem to be independent of each other. Characterizing this flow regime requires the ability to separately control Knudsen number and Reynolds number.

1.3. Rarefied Gas Dynamics and MEMS: Early Work

Simultaneous to these developments in the study of rarefied flows, the foundations of the field of micro-electro-mechanical systems were being laid. Richard Feynman's oft-quoted 1959 talk "There's plenty of room at the bottom" first suggested the idea of micromachinery. (Feynman, 1992) The fabrication methods used for the development of integrated circuits made manufacture of devices at these scales feasible. The first true MEMS device, an accelerometer, was developed at Stanford University in 1979 (Roylance, 1979). Additional early work on MEMS devices, including pressure transducers (Sze, 1994), gyroscopes (Yazdi, 1998), and other sensors, continued through the 1980s and 1990s.

The first studies of fluid mechanics in microsystems were inspired by the use of micro-channels for handling of biological samples, and for air cooling of systems. Initial studies showed that airflows through these channels often fell in the slip-flow regime (Harley, 1995).

The integration of micro-sensors, especially pressure sensors, into microchannels led to the discovery of a non-linear pressure drop within the micro-channels, with apparent pressure drop decreasing as air flow continued on through the channel (Pong, 1994). This phenomenon was investigated in more detail, and modeled by separate research groups at UCLA (Pong, 1994) and MIT (Arkilic, 1997.)

Both investigators found that the non-linear pressure drops were driven by compressibility effects within the fluid. The small size of the channel led to large

frictional losses, and pressure drops, along the channel. These then led to density changes along the channel, and non-linear pressure drops in the channel.

If slip flow effects are included in these models, the result is to reduce friction, while increasing the heat transfer. The decreased frictional losses actually lead the pressure profile in the channel to become more linear (Arkilic, 1997).

Two sets of analytic results exist for slip flow in microchannels that include the effects of changing density in the flow. In both cases, the velocity of the gas along the channel increases as the pressure and density decrease, due to continuity. The Knudsen number also increases, as the mean free path increases. The result of these two effects is that rarefied flow effects increase along the channel.

In a simplified model (Pong, 1994), the flow is treated as locally self-similar. Even though the slip velocity increases along the wall, this effect is considered to be gradual enough that the normal velocity in the flow is zero. In a perturbation solution (Arkilic, 1997), these changes are considered, with continuity requiring a net flow from the centerline of the channel to the wall region, and a resultant change in shear stress.

Confirming these models proved to be experimentally difficult. Experimental apparatus either gave accurate measurements of pressure along the channel (Pong, 1994)), or of the flow rate along the channel (Arkilic, 1997). Both pieces of data are necessary for accurate measurement of the momentum accommodation coefficient, which is needed for generalized results. By making assumptions about the pressure distribution within the channel, Arkilic et al. were able to calculate a momentum accommodation coefficient of approximately 0.8 for air and crystalline silicon, while Pong, et al. calculated a value of 1.2 for nitrogen and polynitride. This value is higher than the

theoretical maximum of 1.0. An accommodation coefficient greater than 1.0 suggests that the gas molecule actually gains tangential momentum during the collision with the wall, and is likely to be a non-physical result. This discrepancy might be a result of surface roughness. However, all of these numbers should be considered unique for the surfaces of the experiment, due to micromachining processes.

1.4. Additional MEMS-Scale Work- Complex Geometries

Several additional micro-channel geometries using airflow have been fabricated and studied experimentally, generally as part of power-MEMS projects. These include gas bearings (Frechette, 2000), radial compressors and turbines (Epstein, 1997), and micro-machined rocket nozzles (Bayt, 1999). Several bio-MEMS applications have involved gas flow, either because of a need to sample air for environmental monitoring, or to use air as a working fluid within analysis. A few of the geometries studied for these applications have included filter screens (Yang, 2001), Y-junctions with liquid (Hu, 2002), and rapid contractions (Lee, 2002).

With the exception of gas bearings, these applications have not lent themselves to the same analytic approaches used for micro-channels. Obtaining experimental results has also been difficult, since the flow diagnostics available are extremely limited. The most commonly used flow diagnostic for macro-scale fluid mechanics, Particle Image Velocimetry, or PIV, is in its infancy for MEMS applications, and to date has only been used reliably for liquid flows (Meinhart, 1999). A molecular based technique known as molecular tagging velocimetry (Lemptert, 2002) is under development for gas flows, but currently has resolution in the tens of microns, well above the scale of this study.

The result is that there are still relatively few experimental results for micro-scale air flows. A few general characteristics of these flows are understood- in additional to the potential for slip, they are characterized by large velocity gradients, leading to large frictional losses, and often large pressure changes. Because of this, compressible flow effects must often be taken into account, even at relatively low velocities. The large frictional losses may lead to viscous heating effects that must be included in the modeling of the system. The small length scales also lead to high heat transfer, leading to an assumption of isothermal flow for most cases.

1.5. Micro-flyer development

The development of microtechnology has led to serious consideration of micro-flyers. Miniaturization of components (McMichael, 1997), as well as the creation of possible micro-propulsion systems (Ho, 2003), has made micro-scale flyers a real possibility. Current micro-flyers have dimensions in the range of centimeters, masses in the range of grams, and Reynolds numbers of approximately 100. As technology improves, it is realistic to expect that all of these values will decrease, and it is possible that components will have dimensions on the order of tens of microns. The potential use of micro-scale rotorcraft also could lead to components at this scale (Miki, 2002). The potential of these applications is one of the major reasons for study of low speed external rarefied flows.

1.6. Steady Low Reynolds Number External Flows

Several solutions exist for flow at finite Reynolds number over a flat plate. The most familiar of these is the Blasius solution, for a laminar boundary layer dominated by viscous terms (Blasius, 1908). For higher speed flows, an Oseen flow solution, which

attempts to approximate momentum terms that are discarded by the Blasius solution, (Panton, 1996) also exists. The Oseen equations have also been solved with a slip-flow boundary condition. (Miura, 1983) Finally, flow over a flat plate can be solved for free molecular flow conditions (Liu, 1959). However, none of these solutions accurately describe the Reynolds number and Knudsen number ranges covered in this study.

1.7. Insect Flight Studies at the Micro-Scale: Quasi-Steady Analysis

The fluid mechanics of airfoils at extremely low Reynolds numbers has been studied extensively as part of studies of insect flight. While measurement at these length scales is extremely difficult, analysis and computation both show that unsteady effects are crucial to understanding insect flight. (Wang, 2005) While insect flight is an unsteady flow phenomena, "quasi-steady" analysis have been attempted, where the insect wing is treated as a steady airfoil at given part of its flapping motion, and the results integrated over time to obtain the flight characteristics. While this approach has been shown to be inaccurate studies of steady flow over low-Reynolds number airfoils have been performed to gain physical insight into low-Reynolds number effects.

Sunada, Sakaguchi, and Kawachi attempted to investigate low-Reynolds number behavior for 4 cm chord airfoils by towing them slowly through a water tank. This approach allows accurate Reynolds number scaling, but does not allow Mach number or Knudsen number effects to appear in the results. The results for low-Reynolds number steady flight show that airfoil geometries used at higher Reynolds numbers do not give optimal performance at lower Reynolds numbers (Sunada, 1997). A study of airfoil geometries at Reynolds numbers of approximately 400 showed that performance depended heavily on two factors: the thickness of the leading edge of the airfoil, and the

angle of attack of the trailing edge. Performance was optimized by keeping the leading edge as thin as possible, and the trailing edge angle of attack as large as possible without separation. The contour of the airfoil itself was relatively unimportant.

1.8. Existing Fabrication Technology

The discovery that contour shape does not matter at low Reynolds numbers is an extremely useful finding, given the limitations of current microfabrication technology. Because conventional micromachining processes are planar in nature, creating a complex contoured surface is extremely difficult. Using planar processes can be used to create airfoil-like structures of the thickness of a silicon wafer, from 500 to 10000 microns. This has been demonstrated by the fabrication of compressor and turbine blades for power MEMS applications (Epstein, 1997).

Contoured airfoils may also be produced by a process currently under development known as "grey-scale" lithography, which does allow for the creation of contoured shapes. Therefore, it is possible that actual micro-flyer designs will have the capability of using contoured airfoils. (Waits, 2003)

1.9. Development of Computational Methods for Low-Reynolds Number External Flows with Rarefied Flow Effects

Because of the difficulty in experimental study of micro-scale flows, much of the work to date has been on computational methods. When there are weak non-equilibrium effects in the flow, Navier-Stokes solvers can be used to study the flow, so long as all the physical effects mentioned earlier are incorporated.

When strong non-equilibrium effects need to be incorporated, four sets of computational methods are available:

1. Solution of Navier-Stokes equations with slip conditions

2. Solution of higher-order equations such as the Burnett Equations
3. Solution of the Boltzmann Equation through particle methods, such as Direct Simulation Monte Carlo (DSMC)
4. Hybrid methods, combining one or more of the above.

Solving the Navier-Stokes equations with slip flow conditions is the easiest of these options (Karniadakis, 2002). However, as shown in table (1.1), this approach is only reliable for Knudsen numbers of 0.1 or less. Additionally, use of slip flow conditions can only capture breakdown of equilibrium at the wall. If equilibrium breakdown occurs in vortices being shed from the wall, for instance, they will not be captured by this model.

Using higher-moment equations, such as the Burnett equations, offers the possibility of capturing these effects. The Burnett equations represent a perturbation of the Navier-Stokes equations designed to incorporate the change in the stress tensor due to non-equilibrium effects (Balakrishnan, 1999). The Burnett equations reduce to the Navier-Stokes equations for axial flows, meaning that results for the micro-channel flows studied experimentally are identical to the slip-flow solutions. However, it is possible that in more complex flows, the Burnett flow may provide a more accurate solution.

A third option for including non-equilibrium effects is the use of particle methods. Particle techniques, such as the direct simulation Monte Carlo Method (Bird, 1994) model gas flows by simulating a statistically meaningful number of gas molecules, and their collisions. This is a commonly used approach for high-speed rarefied flows when the gas is a dilute gas. A gas is dilute when the distance between the gas molecules is large relative to the size of the molecules. When the direct simulation Monte Carlo

method is implemented, it provides a solution consistent with the Boltzmann equation, which represents the highest order description of dilute gas flow.

However, for subsonic flows, such as those commonly occurring in microsystems, DSMC requires the simulation of a large number of particles. Because DSMC is a statistical method, there is a statistical velocity scatter in the results. If we divide this statistical scatter by the flow velocity, then the relative error in the velocity is a function of the Mach number, and the sample size, as show in equation (1.4) (Sun, 2003)

$$\frac{\text{velocity scatter}}{u} \approx \frac{1}{u}\sqrt{\frac{2RT}{N}} \approx \frac{1}{M\sqrt{N}} \tag{1.4}$$

where M is the Mach number, and N is the number of particles per cell in the simulation. Because micro-flows generally occur at extremely low mach numbers, the number of particles required to simulate a micro-flow accurately may increase beyond what can be realistically used in an engineering simulation.

Two approaches have been taken to solve this problem. The first is to apply a filter to the results from a simulation that may not otherwise be converged, removing statistical fluctuations (Kaplan, 20002). The second approach, which has been developed into the Information Preservation (IP) method, tracks both an "information" velocity and particle velocities (Sun, 2003).

A fourth approach that may be used in simulation of rarefied flows is to combine two or more of the approaches listed above, using the computationally expensive methods only in areas where continuum theory is breaking down (Karniadakis, 2002, Sun, 2004).

While all of these approaches have been computationally implemented, there are relatively few experimental approaches for codes to be validated against. A particular

weakness is that most existing experimental results are heavily axial flows, meaning that many of the effects that are only captured by higher order equations are not significant

1.10. Thesis Organization

Reviewing the results for MEMS scale rarefied flows, micro-flight, and rarefied flow, a gap in the engineering understanding becomes apparent. There are no test results, and only unvalidated computational results, that indicate how an airfoil will behave at low Reynolds number, low Mach number, and moderate Knudsen number. If we wish to create engineering tools for the design of nano-scale fliers, this gap must be filled. This thesis will focus on the development of measurement techniques for aerodynamics in this regime.

In Chapter 2, a theoretical model, based on adding a slip boundary condition to the Blasius boundary layer equations, was used to determine which conditions could result in detectable rarefied flow effects. Because of the novel nature of these experiments, a unique flow testing facility was designed, fabricated and validated, as described in Chapter 3. Simultaneously, an integrated microdevice, including both a micro-machined flat plate airfoil and a piezoresistive force sensor, was designed, as described in Chapter 4. Chapter 5 describes the fabrication and validation of this device. Chapter 6 reviews the challenges in integrating these technologies, and lays out a road-map for future work.

CHAPTER 2

MOMENTUM AND HEAT TRANSFER IN A LAMINAR BOUNDARY LAYER WITH SLIP FLOW

2.1. Introduction

To allow design of experimental facilities for the study of rarefied flow over micro-airfoils, a scaling law needs to be developed to allow prediction of rarefied flow effects. This chapter details the development of scaling law for rarefied flow over an airfoil based on boundary layer theory. The momentum and heat equations are solved for a Blasius boundary layer with a slip flow condition, and predictions are made for changes in skin friction, heat transfer, and other flow properties based in these results.

2.2. Previous Results

Several previous investigators have attempted to study rarefied flow in a boundary layer. A first-order solution, based on integral methods, of the boundary layer equations suggests that the boundary layer thins as a result of slip effects (Lin, 1951). However, integral methods were unable to show any changes in skin friction. A more extensive study (Kogan, 1969) was unable to make any quantitative estimates of how slip boundary conditions affected the rarefied boundary layer. Computational studies have also been made of external flow conditions, such as flat plate airfoils (Sun, 2004). These studies have shown that non-equilibrium effects will change the skin friction on a flat plate in slip flow.

2.3. Boundary Layer Governing Equations

As shown in Figure 2.1, flow over a plate can be described as consisting of a uniform external flow region, and a boundary layer of finite thickness.

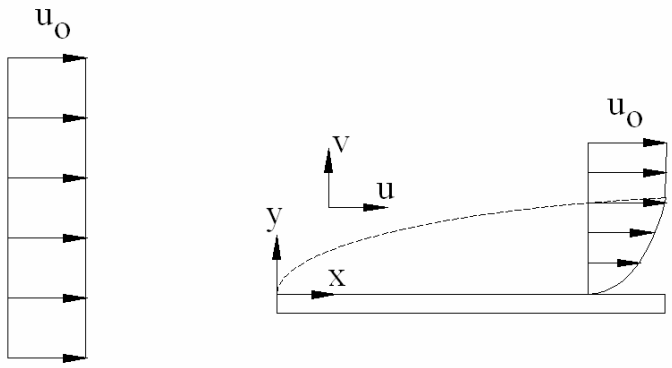

Figure 2.1. Boundary Layer flow over a flat plate

The flow is governed by the continuity equation, and conservation of momentum in the x-direction:

$$\frac{\partial \rho}{\partial t} + \frac{\partial \rho u}{\partial x} + \frac{\partial \rho v}{\partial y} = 0 \tag{2.1}$$

$$\frac{\partial u}{\partial t} + u\frac{\partial u}{\partial x} + v\frac{\partial u}{\partial y} = -\frac{\partial P}{\partial x} + \upsilon\left[\frac{\partial^2 u}{\partial x^2} + \frac{\partial^2 u}{\partial y^2}\right] \tag{2.2}$$

where u is the velocity in the x-direction, v is the velocity in the y-direction, P is the pressure, ρ is the density, and υ is the kinematic viscosity.

This flow was first studied extensively by Blasius (Blasius, 1908) who assumed steady, incompressible, laminar flow, no significant gradients of pressure in the x-direction, and that velocity gradients in the x-direction are small compared to velocity gradients in the y-direction. Based on these assumptions, equations (2.1) and (2.2) then simplify into the boundary-layer equations given below:

$$\frac{\partial u}{\partial x}+\frac{\partial v}{\partial y}=0 \tag{2.3}$$

$$u\frac{\partial u}{\partial x}+v\frac{\partial u}{\partial y}=\upsilon\frac{\partial^2 u}{\partial y^2} \tag{2.4}$$

The velocities u and v will be functions of the stream function Ψ:

$$u=\frac{\partial\Psi(x,y)}{\partial y} \tag{2.5}$$

$$v=-\frac{\partial\Psi(x,y)}{\partial x} \tag{2.6}$$

These equations can then be transformed, using the non-dimensionalizations and non-dimensional stream functions given below:

$$x^*=x/L \tag{2.7}$$

$$y^*=\frac{y}{(\upsilon\,\mathrm{L/uo})^{1/2}} \tag{2.8}$$

$$u^*=u/u_o \tag{2.9}$$

$$v^*=\frac{v}{(\upsilon\,u_o/x)^{1/2}} \tag{2.10}$$

$$\eta=\frac{y^*}{(x^*)^{1/2}}=\frac{y/(\upsilon\,\mathrm{L/uo})^{1/2}}{(\mathrm{x/L})^{1/2}}=\frac{y}{(\upsilon\,\mathrm{x/uo})^{1/2}} \tag{2.11}$$

$$u^*=\frac{u}{u_o}=f'(\eta) \tag{2.12}$$

$$v^*=\frac{v}{(\upsilon\,u_o/x)^{1/2}}=0.5\,[\eta\,f'(\eta)-f(\eta)] \tag{2.13}$$

where L is the length of the flat plate

A governing equation for *f* can be found by substituting these results into the x-momentum equation (2.2):

$$f'''(\eta) = -0.5\, f(\eta)\, f''(\eta) \tag{2.14}$$

For flow at non-rarefied length scales, the boundary conditions for the problem are no-slip, and no through flow at the wall, and $u = u_o$ as y approaches infinity. In non-dimensional variables, these become:

$$u^*(y=0) = 0 \Rightarrow f'(\eta = 0) = 0 \tag{2.15}$$

$$v^*(y=0) = 0 \Rightarrow f(\eta = 0) = 0 \tag{2.16}$$

$$u^*(y \to \infty) = 1 \Rightarrow f'(\eta \to \infty) = 1 \tag{2.17}$$

Based on these boundary conditions, Blasius was able to solve the problem using a shooting method, which gave an initial value of 0.33206 for *f"*.

Using this result, Blasius calculated the self-similar laminar boundary layer, with a velocity profile and non-dimensional shear stress.

When the flow becomes rarefied, the no-slip condition given by equation (2.15) is replaced by the slip-flow condition given as equation (1.3). If we use the non-dimensionalizations given in (2.7) through (2.13), this condition can be non-dimensionalized to obtain

$$f'(0) = \frac{(2-\sigma)}{\sigma}\, \mathrm{Kn_x}\, \mathrm{Re}_x^{1/2}\, f''(0) = \mathrm{K}_1\, f''(0) \tag{2.18}$$

where Kn_x and Re_x are the Knudsen and Reynolds numbers based on x, and K_1 is a non-dimensional parameter that describes the behavior at the surface:

$$K_1 = \frac{(2-\sigma)}{\sigma} Kn_x \, Re_x^{1/2} \tag{2.19}$$

In physical terms, equation (2.18) states that the non-dimensional wall slip velocity will be a function of a non-equilibrium term K_1, and the non-dimensional wall shear stress. Because K_1 is a function of x, K_1 will decrease as we move along the wall in the flow direction.

Recent research (Wantanabe, 1998) suggests that as length scales in liquid flows approach the continuum limit, a similar slip condition may apply. This slip condition is generally given as

$$u_{slip} = \beta \left. \frac{\partial u}{\partial n} \right|_{wall} \tag{2.20}$$

where β is the slip length for the liquid. The existence of liquid slip, as well as the appropriate length scales for β, are still subjects of controversy within the fluid mechanics community (Stone, 2005). Experimental measurements (Meinhart, 2002) suggest that the slip length for hydrophobic surfaces with water are on the order of 1 μm, suggesting that liquid flows with boundary layer thicknesses of 100 μm or less may encounter slip. To accommodate this possibility, this solution can easily be modified to cover liquid slip by using a modified definition of K_1:

$$K_1 = \frac{\beta}{x} Re_x^{1/2} \tag{2.21}$$

2.4. Formulation of Boundary Layer Equations with Slip Flow

The revised boundary condition suggests that self-similarity will be lost, and the velocity will be a function of both η and K_1. While the definition of u* is unchanged, the

definition of v* must be modified to incorporate the derivative of the stream function with respect to K_1:

$$v^* = \frac{v}{(\upsilon u_o / x)^{1/2}} = 0.5\left[\eta \frac{\partial f(\eta, K_1)}{\partial \eta} - f(\eta, K_1) + K_1 \frac{\partial f(\eta, K_1)}{\partial K_1}\right] \tag{2.22}$$

When combined with the fact that all derivatives in x will now include a K_1 term, this means that the ordinary differential equation given in (2.14) becomes a partial differential equation, as described in (2.23):

$$\frac{\partial^3 f}{\partial \eta^3} = -0.5\, f \frac{\partial^2 f}{\partial \eta^2} - 0.5 K_1 \frac{\partial}{\partial \eta}\left[\frac{\partial f}{\partial \eta}\frac{\partial f}{\partial K_1}\right] \tag{2.23}$$

The additional term, incorporating K_1, incorporates the loss of self-similarity. The no-slip governing equation will be recovered when K_1 is equal to zero. To solve in the slip domain, the partial differential equation must be solved over the entire slip flow region, as well as into the transitional and free-molecular flow regions. This can be accomplished using a marching code, beginning from large values of K_1, and marching the code until K_1 approaches zero. Because large values of K_1 correspond to small values of x, this approach marches in the flow direction, similar to existing boundary layer codes. (White, 1991)

2.5. Numerical Solution of Boundary Layer Equations with Slip Flow

Equation (2.23) is discretized using center-difference approximations for all derivatives with respect to η. In order to simplify the expression as much as possible, *f'* is substituted for $\partial f/\partial \eta$:

$$f'_{i,j} = \frac{f_{i,j+1} - f_{i,j-1}}{2\Delta\eta} + O\left((\Delta\eta)^2\right) \tag{2.24}$$

Equation (2.23) then becomes

$$\frac{\partial^2 f'}{\partial \eta^2} = -0.5\, f \frac{\partial f'}{\partial \eta} - 0.5 K_1 \frac{\partial}{\partial \eta}\left[f' \frac{\partial f}{\partial K_1} \right] \tag{2.25}$$

For the mixed derivative, a first-order upwind expression is used, as shown in equation (2.26):

$$\frac{\partial}{\partial \eta}\left[f' \frac{\partial f}{\partial K_1} \right]_{i,j} = \frac{1}{\Delta \eta} \frac{1}{\Delta K_1} \left[f'_{i,j} \left(f_{i,j} - f_{i-1,j} \right) - f'_{i,j-1} \left(f_{i,j-1} - f_{i-1,j-1} \right) \right] \tag{2.26}$$

This yields the following expression for $f_{i-1,j}$:

$$\begin{aligned} f_{i-1,j} &= f_{i,j} + \frac{f'_{i,j-1}}{f'_{i,j}} \left(f_{i-1,j-1} - f_{i,j-1} \right) \\ &+ \frac{2\Delta K_1}{K_1 f'_{i,j}} \left(\frac{f'_{i,j+1} - 2.0\, f'_{i,j} + f'_{i,j-1}}{\Delta \eta} + \frac{f_{i,j}}{4.0} \left(f'_{i,j+1} - f'_{i,j-1} \right) \right) \end{aligned} \tag{2.27}$$

When K_1 is extremely large, flow is uniform in the x-direction, giving the initial conditions:

$$f'|_{K_1 \to \infty} = 1 \tag{2.28}$$

$$f|_{K_1 \to \infty} = \eta \tag{2.29}$$

Along the wall, the boundary conditions are the no-through-flow condition given by (2.16) and the slip condition given by (2.18):

$$f(\eta = 0) = 0 \tag{2.16}$$

$$\left. \frac{\partial f}{\partial \eta} \right|_{\eta=0} = K_1 \left. \frac{\partial^2 f}{\partial \eta^2} \right|_{\eta=0} \tag{2.18}$$

The slip condition is implemented through the following first-order approximation

$$f'_{i,1} = \frac{K_{1i}\, f'_{i,2}}{\left(K_{1i} + \Delta \eta_{wall} \right)} + O\left(\frac{(\Delta \eta)^2}{(\Delta \eta + K_{1i})} \right) \frac{\partial^2 f'}{\partial \eta^2} \tag{2.30}$$

The proposed scheme is conditionally stable. The following stability criteria apply:

$$\Delta K_1 \le \frac{7(\Delta\eta)^2 K_1}{3} \tag{2.31}$$

$$\Delta K_1 \le \frac{\left(1 + f'_{i,j}\right)\Delta\eta\, K_1}{2 f_{i,j}} \tag{2.32}$$

This algorithm is used with a starting K_1 value ranging from 100 to 200, and $\Delta\eta$ varying from 0.0001 to 0.005, to produce the results given.

2.6. Computational Results

The values of the stream function *f* for K_1 ranging from 0 to 10, which includes the entire slip-flow region, are show as figure 2.2:

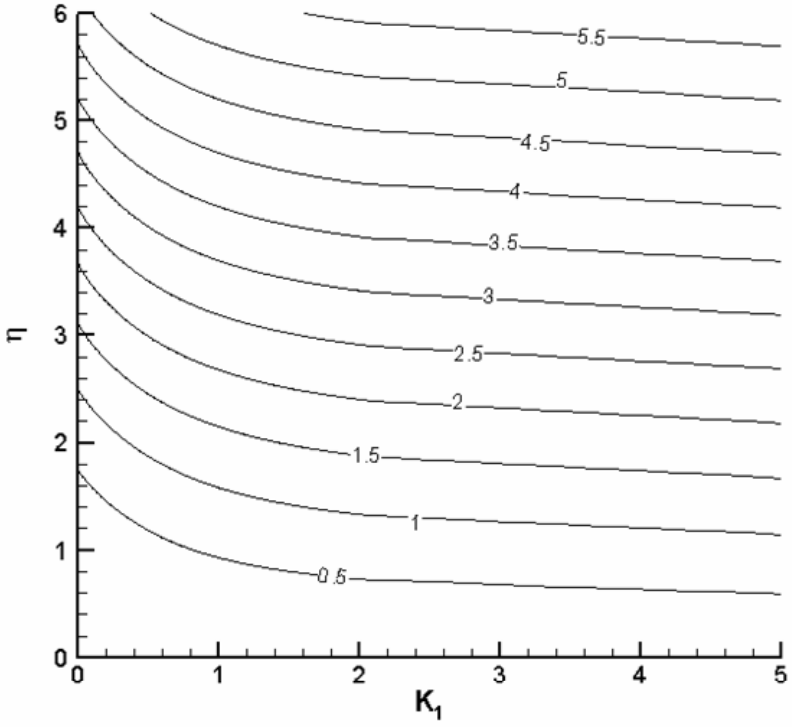

Figure 2.2. *f* as a function of K_1 and η

This figure shows that, for any value of η in the boundary layer, *f* decreases as the flow becomes more rarefied.

Values of u* and v* are shown as figures 2.3 and 2.4:

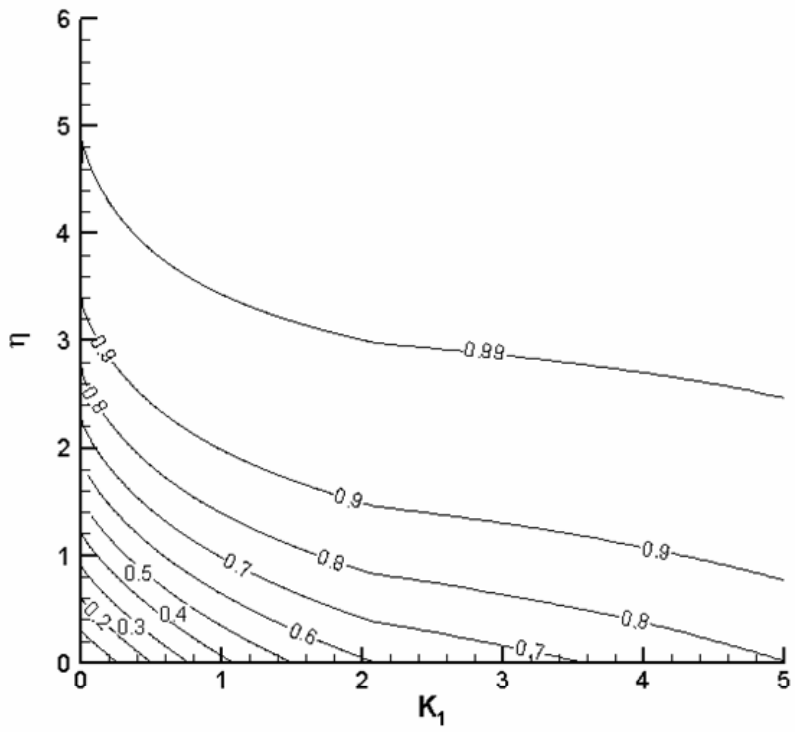

Figure 2.3. u* as a function of K_1 and η

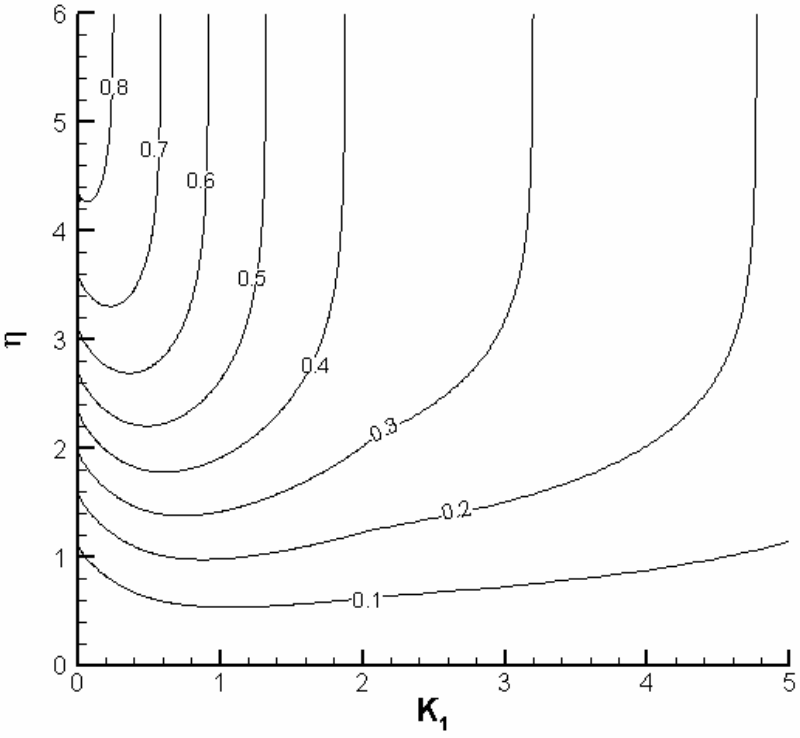

Figure 2.4. v* as a function of K_1 and η

These results show that, at any given vertical position η in the boundary layer, u* will increase, and v* will decrease, as the flow becomes more rarefied.

The non-dimensional friction, or $f''(0)$, is shown in Figure 2.5:

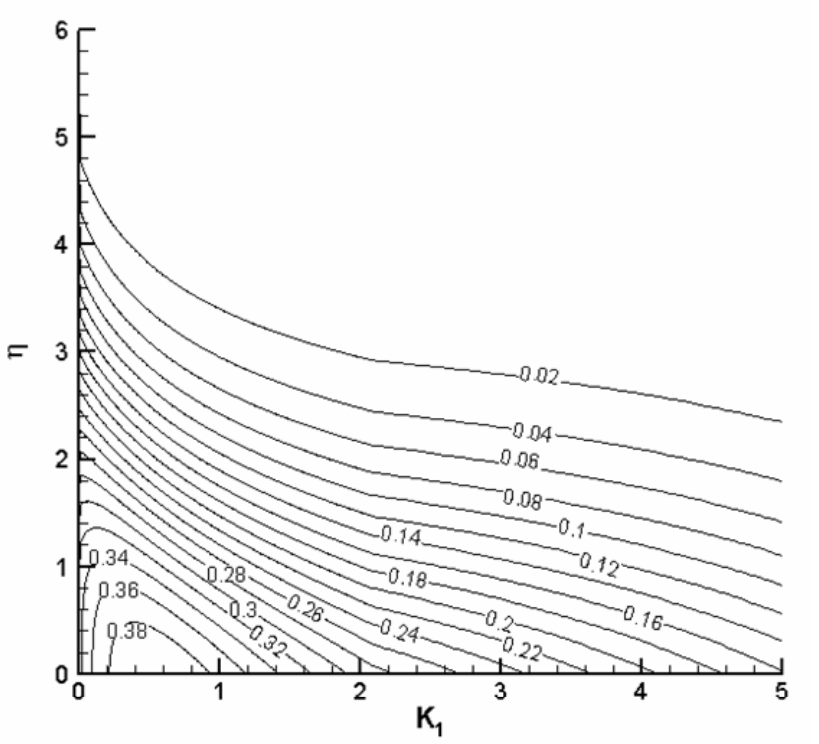

Figure 2.5. Non-dimensional friction *f*' as a function of K_1 and η

Figure 2.5 shows the surprising result that the friction in the flow peaks not at the no-slip condition, but at a value of K_1 of approximately 0.50. This is a result of the loss of self-similarity in the flow.

Closer inspection of the velocity contours shows that the y-velocity v* also peaks locally for values of K_1 less than 1.0. This gives some insight into the reason for this local increase in friction.

As the flow proceeds along the plate, the value of K1 decreases, and the slip velocity along the wall also decreases. Continuity requires that fluid move away from the wall. This can be seen in the values of the stream function. When combined with the additional right-hand term given in equation 2.22, the two-dimensional nature of the flow leads to a local increase in friction. This means that the two-dimensional effects in a boundary layer with slip can not be ignored, and may lead to an unexpected increase in skin friction.

The non-dimensional wall shear stress $f''(0)$ is shown as figure 2.6:

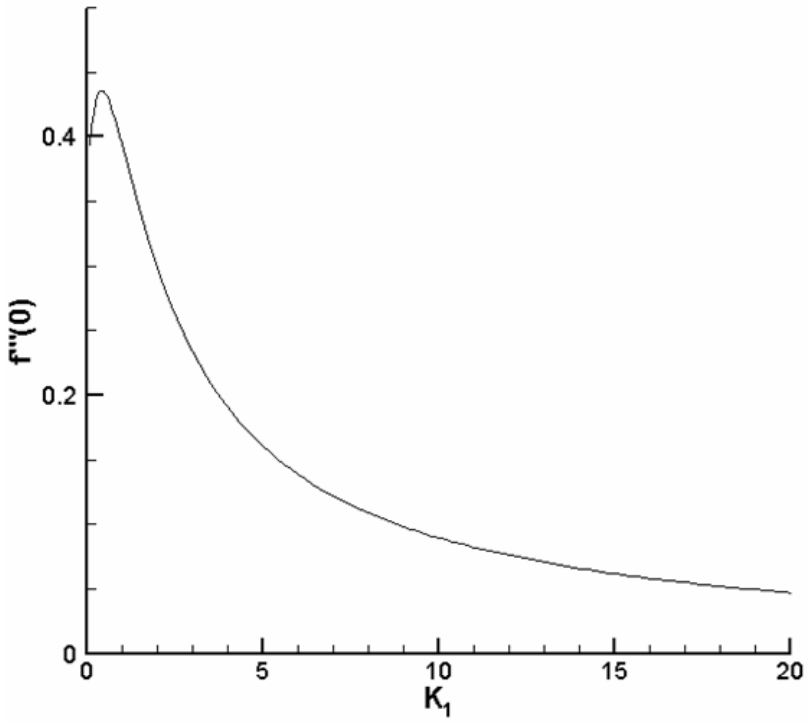

Figure 2.6. $f''(0)$ versus K_1

$f''(0)$ has a peak value of .4358 when K_1 is equal to 0.0467. The two-dimensional effects cause a peak local friction of approximately 25 percent greater than the no-slip value. $f''(0)$ returns to the no-slip value as K1 approaches 0, and asymptotically approaches zero as K_1 approaches infinity.

Figure 2.7 shows $f'(0)$, or the non-dimensional slip velocity, as a function of K_1. These results show that the wall velocity asymptotically approaches the free stream velocity as rarefaction increases.

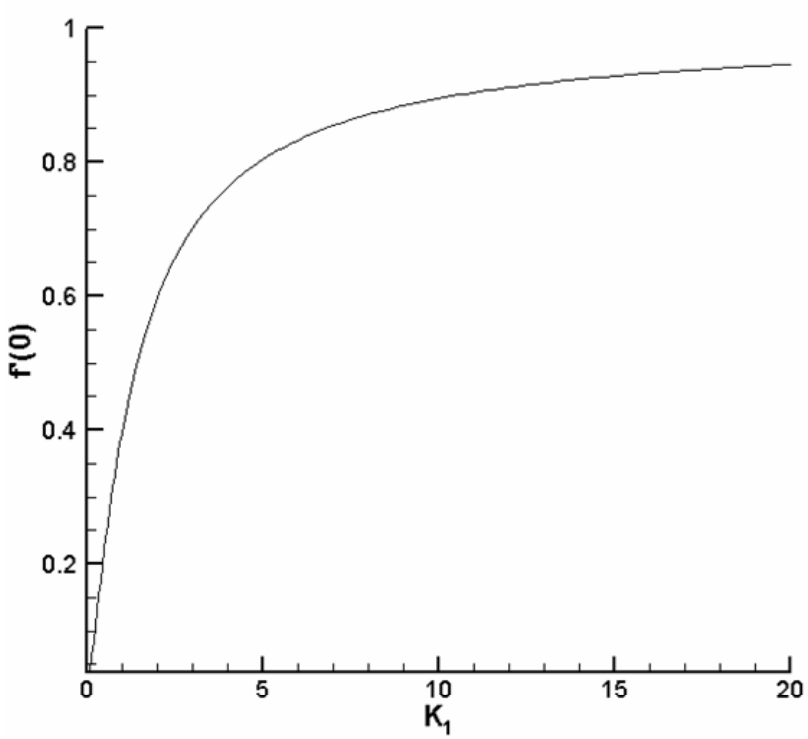

Figure 2.7. u^*_{wall} versus K_1

As the Knudsen number approaches zero, K_1 also approaches zero, where the no-slip condition and the classical boundary layer solution are recovered. As the Knudsen number becomes large, K_1 approaches infinity, and the non-dimensional slip velocity approaches 1, indicating 100 percent slip at the wall.

Figures 2.8 and 2.9 show the normalized x and y velocity profiles in the boundary layer for various values of K_1:

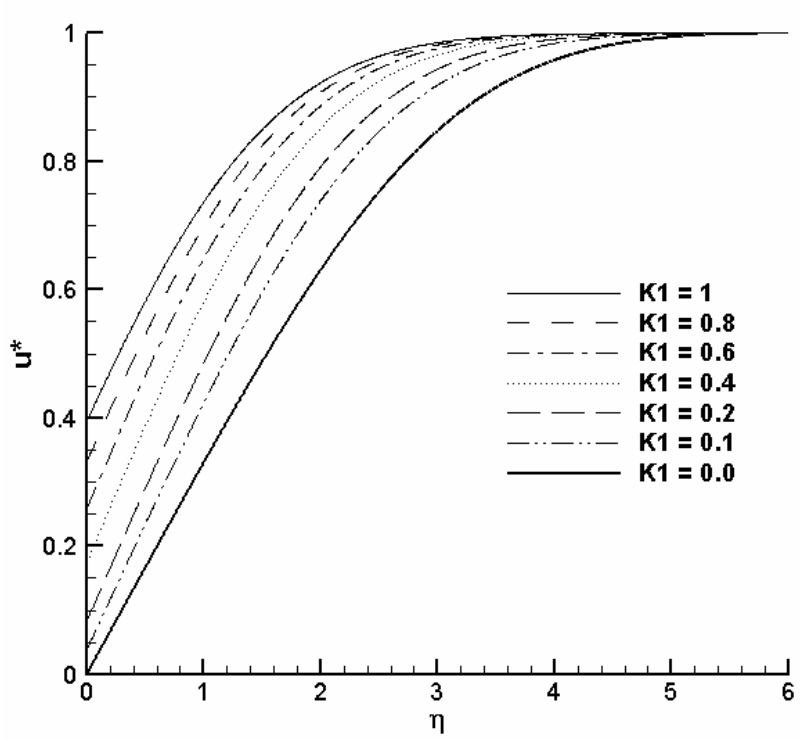

Figure 2.8. u* versus η for various values of K_1

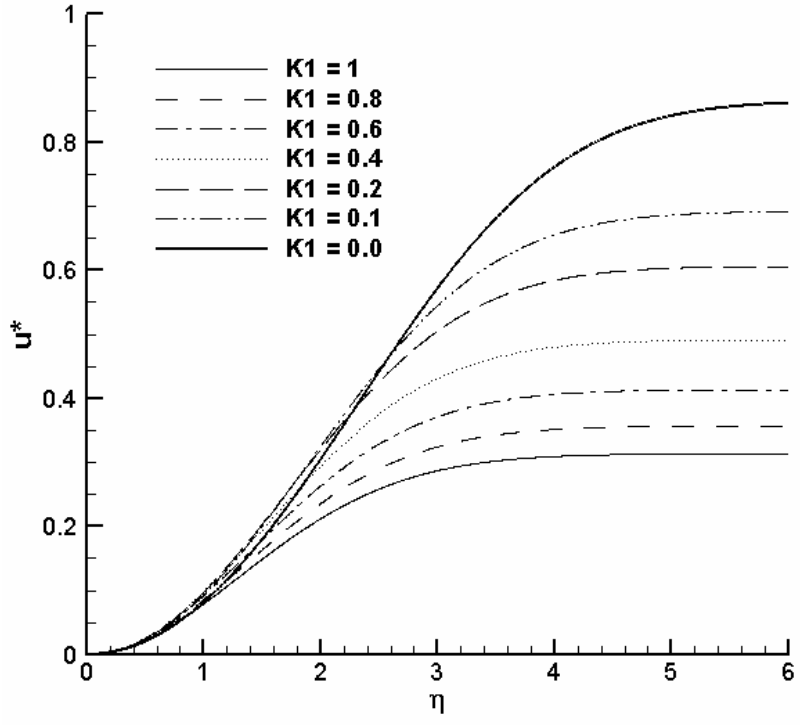

Figure 2.9. v* versus η for various values of K_1

The figures show that as the tangential components of the velocity increase, the normal components decrease.

One result that can be seen in Figure 2.8 is that even as the wall velocity changes drastically, the overall boundary layer thickness does not change as rapidly. The physical thickness of the boundary layer is given by equation (2.33):

$$\frac{\delta_{99}}{x} = \eta_{99}\,\mathrm{Re}_x^{1/2} \tag{2.33}$$

Equation (2.32) can be substituted into (2.18) to obtain an expression for K_1 based on boundary layer thickness:

$$K_1 = \frac{(2-\sigma)}{\sigma}\frac{Kn_\delta}{\eta_{99}} \tag{2.34}$$

For equilibrium flows, η_{99} is a constant with a value of 5.0. For a non-equilibrium boundary layer, η_{99} varies along the plate. Figure 2.10 shows the value of η_{99}, where u* is equal to 0.99, as a function of K_1. As the non-dimensional wall slip velocity increases to greater than 0.99, the boundary layer thickness becomes zero. This occurs at values of K_1 greater than 80.

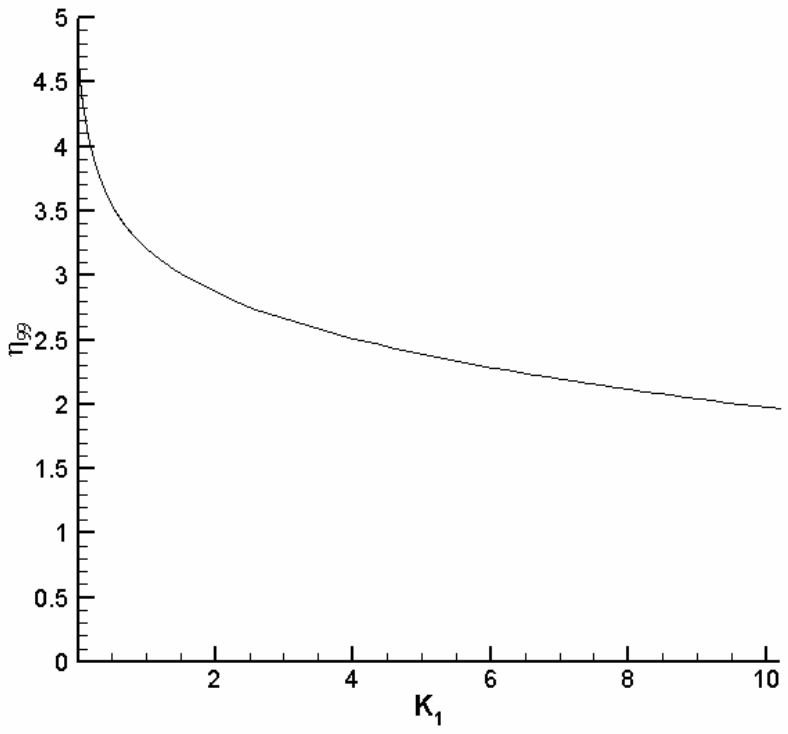

Figure 2.10. η_{99} versus K_1

The non-equilibrium behavior at the wall, as measured by K_1, is proportional to the boundary layer thickness, which is a measure of the velocity gradient near the wall. If the form of K_1 given in equation (2.34) is used, K_1 is a function of η_{99}, which is a function of K_1. However, we can see from figure 2.10 that η_{99} does not change by orders of magnitude as a result of these effects, meaning the original form of K_1 will still be used for flow characterization.

The displacement thickness and momentum thickness of the boundary layer will also vary with K_1. The displacement thickness, which measures the amount of the fluid displaced from the boundary layer, is defined as

$$\delta^* = \int_o^\infty \left(1 - \frac{u}{u_o}\right) dy \tag{2.35}$$

This can be converted into non-dimensional co-ordinates:

$$\frac{\delta^*}{\sqrt{u_o \upsilon / x}} = \int_o^\infty (1 - f')d\eta \tag{2.36}$$

The momentum thickness, which measures the amount of momentum removed from the boundary layer, is defined as

$$\theta = \int_o^\infty \frac{u}{u_o}\left(1 - \frac{u}{u_o}\right)dy \tag{2.37}$$

This can be expressed in non-dimensional form:

$$\frac{\theta}{\sqrt{u_o \upsilon / x}} = \int_o^\infty f'(1 - f')d\eta \tag{2.38}$$

The momentum thickness and displacement thickness as functions of K_1 are plotted as figures 2.11 and 2.12:

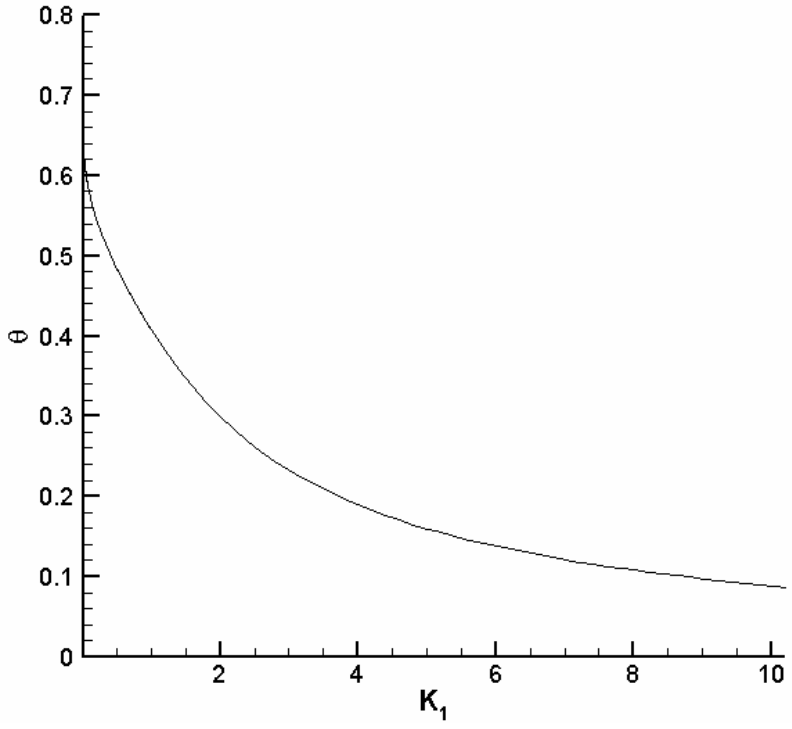

Figure 2.11. Momentum Thickness versus K_1

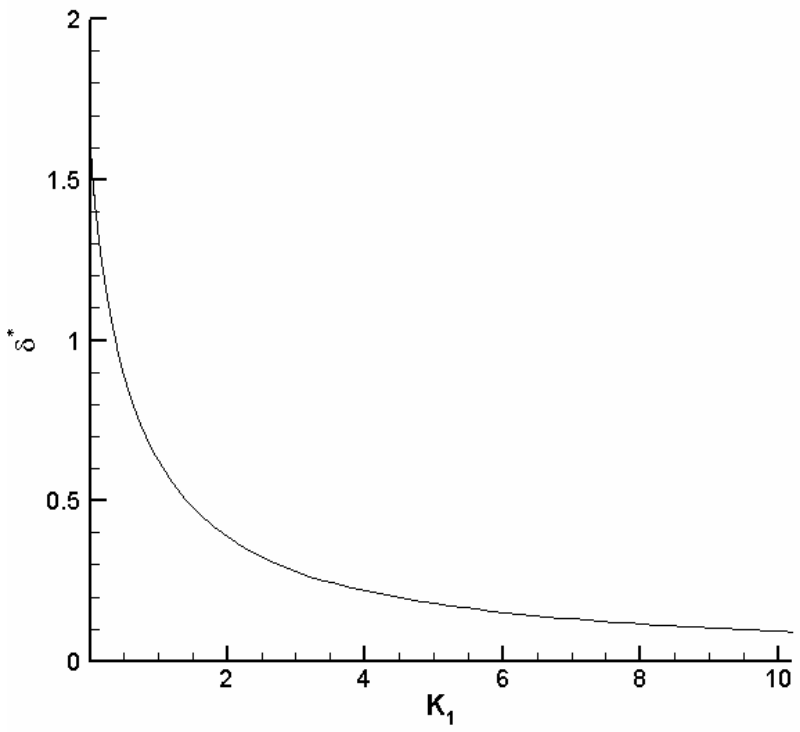

Figure 2.12. Velocity Thickness versus K_1

The results of this analysis can also be used to predict possible transition to turbulence within a rarefied boundary layer. A Reynolds number based on velocity thickness is calculated, as shown in equation (2.38):

$$\mathrm{Re}_{\delta} = \frac{\rho \bar{u} \delta^*}{\mu} \tag{2.39}$$

Previous researchers have found that laminar boundary layers become unstable when Re_{δ} approaches 520 (White, 1991). Since the effect of slip is to decrease δ^*, this suggests that transition to turbulence may be delayed in a rarefied boundary layer.

2.7. Calculation of Drag Force

There are two engineering reasons to be interested in rarefied flow over a flat plate: decreases in skin friction, and increases in heat transfer along the surface.

The wall friction for a laminar boundary layer is given by the expression below:

$$\tau_{wall} = \mu\left(\frac{\partial v}{\partial x} + \frac{\partial u}{\partial y}\right) = \mu\frac{\partial u}{\partial y} = \frac{\rho^{1/2}\mu^{1/2}\, u_o^{3/2}}{x^{1/2}} f''(0) \tag{2.40}$$

The friction is proportional to the value of $f''(0)$ given in Figure 2.16. Equation (2.40) can be integrated over the entire plate to obtain the net viscous drag force:

$$F_D = \rho^{1/2}\mu^{1/2}\, u_o^{3/2} \int_0^c \frac{f''(0)}{x^{1/2}}\, dx \tag{2.41}$$

The drag coefficient is defined as:

$$C_D = \frac{F_D}{L\dfrac{\rho U^2}{2}} \tag{2.42}$$

where F_D is the drag per unit span of the airfoil.

For a flat plate with no-slip, the drag coefficient can be obtained by integrating the Blasius result to obtain:

$$C_D = 1.328\, Re_L^{-1/2} \tag{2.43}$$

For a flat plate with slip, the result must be obtained numerically. By substituting the definition of K_1 into (2.41), and performing the appropriate change of variables, we obtain

$$C_D = 4.0\, Re_L^{-1/2}\, K_1 \int_{K_1}^{\infty} \frac{f''(0)}{K_1^2}\, dK_1 \tag{2.44}$$

The drag coefficient based on this integral is plotted as figure (2.13).

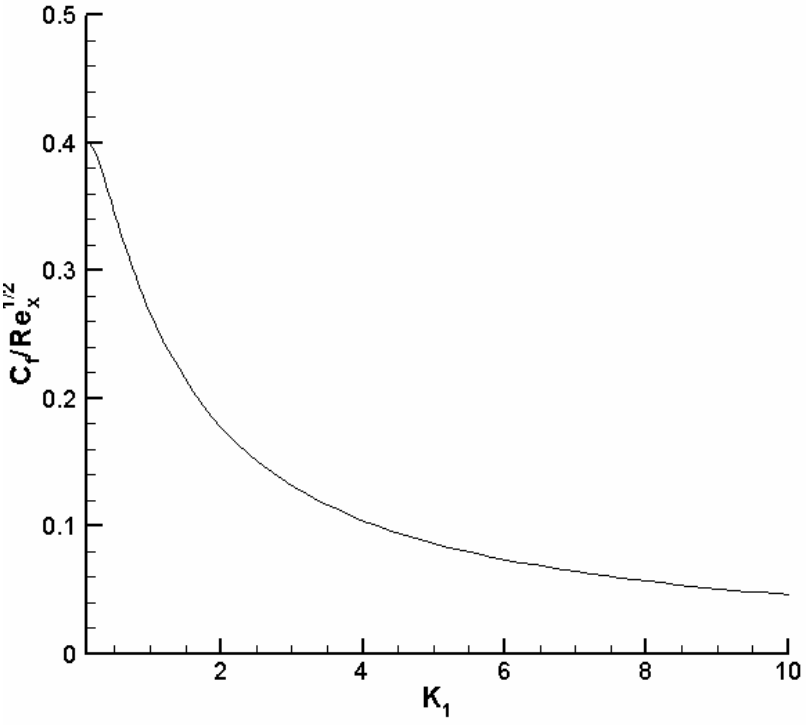

Figure 2.13. Drag Coefficient vs K_1

The percent change in drag due to rarefied flow effects compared to the no-slip solution is plotted as figure 2.14.

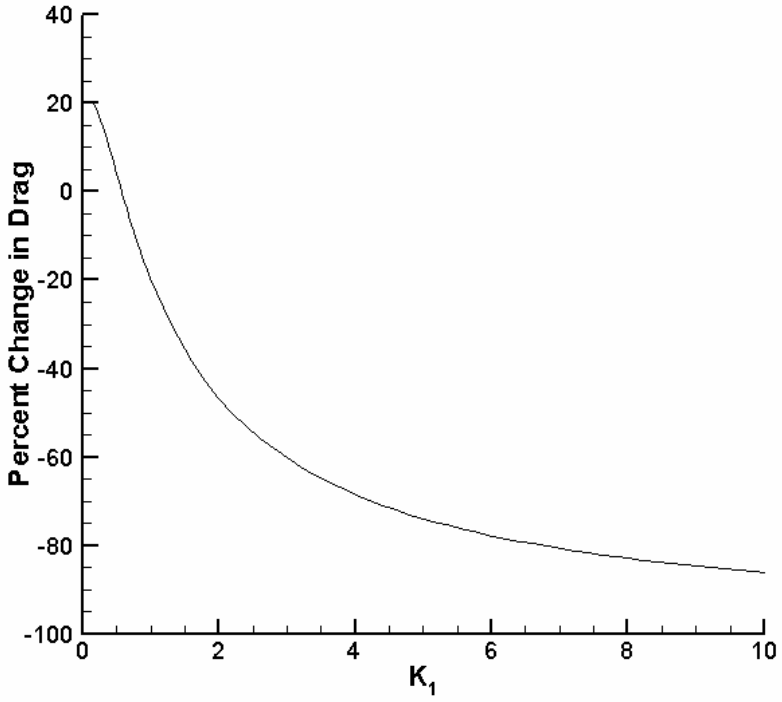

Figure 2.14. Change in Drag Coefficient vs. K_1

These results show a slight increase in drag for slightly rarefied flows, and then a large decrease in drag at higher Knudsen numbers.

2.8. Drag Values for 40 and 100 micron chord Airfoils

Two sample airfoil chords will be studied to estimate the drag forces: a 40-micron airfoil, and a 100-micron airfoil. Tables 2.1 and 2.2 show the estimated values of K_1 as a function of pressure and velocity for each of these airfoils, assuming air at a temperature of 25º C. The momentum accommodation coefficient used is 0.8, the measured value for silicon. (Arkilic, 1995)

u (m/s)	P (atm)					
	0.15	0.2	0.4	0.6	0.8	1.0
30	4.86×10^{-2}	4.21×10^{-2}	2.98×10^{-2}	2.43×10^{-2}	2.11×10^{-2}	1.88×10^{-2}
40	5.62×10^{-2}	4.86×10^{-2}	3.44×10^{-2}	2.81×10^{-2}	2.43×10^{-2}	2.18×10^{-2}
50	6.28×10^{-2}	5.44×10^{-2}	3.85×10^{-2}	3.14×10^{-2}	2.72×10^{-2}	2.43×10^{-2}
60	6.88×10^{-2}	5.96×10^{-2}	4.21×10^{-2}	3.44×10^{-2}	2.98×10^{-2}	2.66×10^{-2}
70	7.43×10^{-2}	6.43×10^{-2}	4.55×10^{-2}	3.72×10^{-2}	3.22×10^{-2}	2.88×10^{-2}
80	7.94×10^{-2}	6.88×10^{-2}	4.86×10^{-2}	3.97×10^{-2}	3.44×10^{-2}	3.08×10^{-2}
90	8.43×10^{-2}	7.30×10^{-2}	5.16×10^{-2}	4.21×10^{-2}	3.65×10^{-2}	3.26×10^{-2}
100	8.88×10^{-2}	7.69×10^{-2}	5.44×10^{-2}	4.44×10^{-2}	3.85×10^{-2}	3.44×10^{-2}

Table 2.1. K_1 for a 40-micron airfoil

u (m/s)	P (atm)					
	0.15	0.2	0.4	0.6	0.8	1.0
30	3.08×10^{-2}	2.66×10^{-2}	1.88×10^{-2}	1.54×10^{-2}	1.33×10^{-2}	1.19×10^{-2}
40	3.55×10^{-2}	3.08×10^{-2}	2.18×10^{-2}	1.78×10^{-2}	1.54×10^{-2}	1.38×10^{-2}
50	3.97×10^{-2}	3.44×10^{-2}	2.43×10^{-2}	1.99×10^{-2}	1.72×10^{-2}	1.54×10^{-2}
60	4.35×10^{-2}	3.77×10^{-2}	2.66×10^{-2}	2.18×10^{-2}	1.88×10^{-2}	1.69×10^{-2}
70	4.70×10^{-2}	4.07×10^{-2}	2.88×10^{-2}	2.35×10^{-2}	2.03×10^{-2}	1.82×10^{-2}
80	5.02×10^{-2}	4.35×10^{-2}	3.08×10^{-2}	2.51×10^{-2}	2.18×10^{-2}	1.95×10^{-2}
90	5.33×10^{-2}	4.61×10^{-2}	3.26×10^{-2}	2.66×10^{-2}	2.31×10^{-2}	2.06×10^{-2}
100	5.62×10^{-2}	4.86×10^{-2}	3.44×10^{-2}	2.81×10^{-2}	2.43×10^{-2}	2.18×10^{-2}

Table 2.2. K_1 for a 100-micron airfoil

These tables show that 40 and 100-micron airfoils may experience slip effects. Figures 2.15 and 2.16 show the expected viscous drag per span on 40 and 100-micron airfoils. The result calculated in equation (2.40) is multiplied by 2 to account for the airfoil having 2 sides.

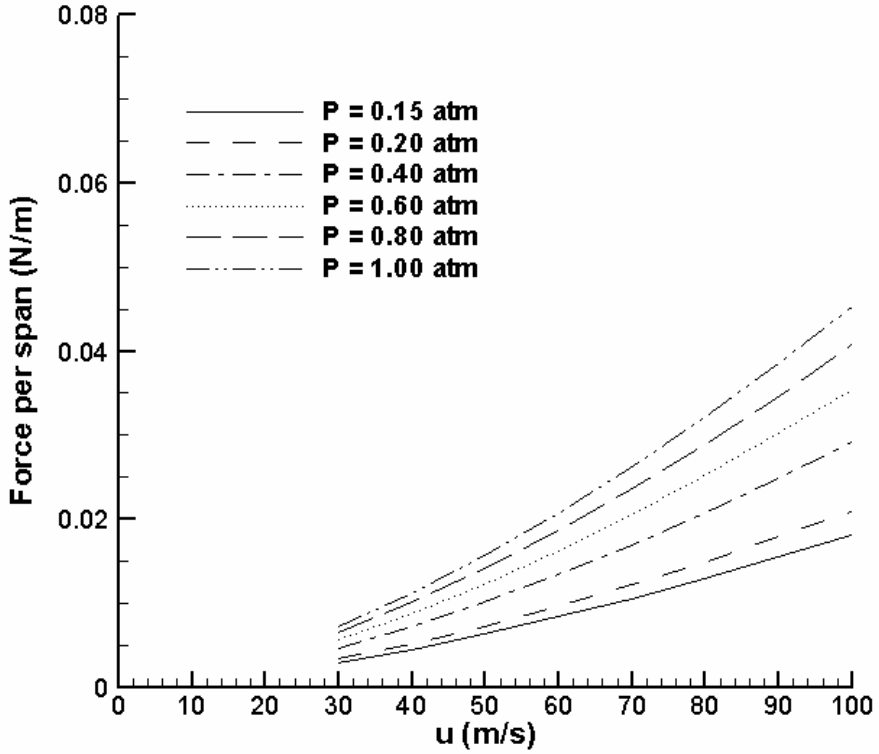

Figure 2.15. Drag Force per span, 40 μm chord airfoil

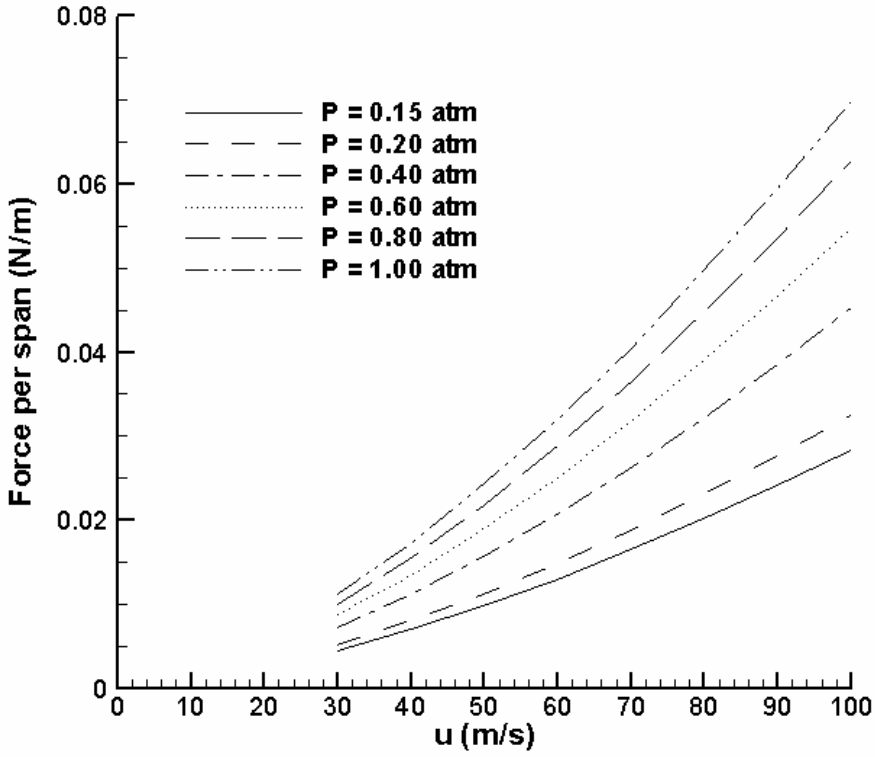

Figure 2.16. Drag Force for per span, 100 μm chord airfoil

2.9. Heat Transfer in Slip Flow Solution

Once the velocity profile is calculated, the heat transfer in a slip flow can be calculated using the same approach that is used in the non-slip solution (Incropera, 2001.) The equation for conservation of energy in a boundary layer with steady flow is given as:

$$u\frac{\partial T}{\partial x}+v\frac{\partial T}{\partial y}=\frac{\alpha}{\rho\, c_p}\frac{\partial^2 T}{\partial y^2} \tag{2.45}$$

where α is the thermal conductivity of the gas, and c_p is the specific heat of the gas

A non-dimensional temperature T* can be defined using the stream temperature T_∞ and the surface temperature T_S:

$$T^*=\frac{T-T_s}{T_\infty-T_s} \tag{2.46}$$

If we assume that T* is a function of η and K_1, and apply the appropriate non-dimensionalizations, (2.46) can be re-written as:

$$0 = \frac{\partial^2 T^*}{\partial \eta^2} + \Pr\left[\left(\frac{\eta u^*}{2} - v^*\right)\frac{\partial T^*}{\partial \eta} + K_1 u^* \frac{\partial T^*}{\partial K_1}\right] \tag{2.47}$$

where Pr is the Prandtl number of the fluid.

The heat transfer equations are discretized using center-difference approximations in the η direction, and a forward difference approximation in the K_1 direction, similar to the method used to solve the momentum equation. This results in the expression:

$$T^*_{i-1,j} = [a+b]T^*_{i,j+1} + [1-2.0a]T^*_{i,j} + [a+b]T^*_{i,j-1} \tag{2.48}$$

where

$$a = \frac{\Delta K_1}{\Pr u^* K_1 (\Delta\eta)^2} \tag{2.49}$$

and:

$$b = \frac{\Delta K_1}{2u^* K_1 \Delta\eta}\left(\frac{\eta u^*}{2} - v^*\right) \tag{2.50}$$

The stability criterion requires that all coefficients remain positive:

$$\Delta K_1 \leq= \frac{\Pr K_1 f'_{i,j} (\Delta\eta)^2}{4.0} \tag{2.51}$$

$$\Delta\eta \leq \frac{4.0 \Pr}{f_{i,j}} \tag{2.52}$$

Correct solution of boundary layer heat transfer will require use of appropriate wall boundary conditions. The thermal boundary conditions for slip flow of a gas will differ from those of slip flow of a liquid, and the two cases will be considered separately.

2.9.1. Heat Transfer in Gas Flows with Slip

The same rarefied flow effects that produce a velocity jump at the surface for gas flows will also produce a temperature jump. The temperature jump boundary condition (Maxwell, 1867) is given as

$$T_{gas} - T_{wall} = \frac{\lambda}{\Pr}\frac{2-\sigma_T}{\sigma_T}\frac{2\gamma}{\gamma+1}\left.\frac{\partial T}{\partial n}\right|_{wall} \tag{2.53}$$

where σ_T is the thermal accommodation coefficient, and γ is the specific heat ratio of the gas.

Equation (2.53) can be non-dimensionalized to obtain:

$$T^*(\eta = 0) = \frac{1}{\Pr}\frac{2-\sigma_T}{\sigma_T}\frac{2\gamma}{\gamma+1}Kn_x \,\mathrm{Re}_x^{1/2}\left.\frac{\partial T^*}{\partial \eta}\right|_{wall} \tag{2.54}$$

Data on thermal accommodation coefficients is extremely limited (Karniadakes, 2002), but the thermal accommodation coefficient and the momentum accommodation coefficients appear to be approximately equal. If this assumption is used, then equation (2.51) simplifies to

$$T^*(\eta = 0) = \frac{1}{\Pr}\frac{2\gamma}{\gamma+1}K_1\left.\frac{\partial T^*}{\partial \eta}\right|_{wall} \tag{2.55}$$

The boundary condition far from the wall will be

$$T(\infty) = T_\infty \tag{2.56}$$

In non-dimensional form, this becomes:

$$T^*(\infty) = 1 \tag{2.57}$$

At large values of K_1, the temperature jump will become infinitely large, and the gradients at the wall will be negligible, giving a uniform temperature field:

$$T^*(K_1 \to \infty) = 1 \tag{2.58}$$

Figures 2.17, 2.18, and 2.19 show the wall temperature as a function of K_1 and Pr for values of γ of 4/3, 1.4, and 5/3. The Prandtl numbers selected represent typical values for gases. These results show the temperature jump is a substantial percentage of the temperature difference for the flow in the slip flow regime. They also show that while the Prandtl number has a noticeable effect on the wall heat transfer, the effect of varying the specific heat ratio is almost negligible.

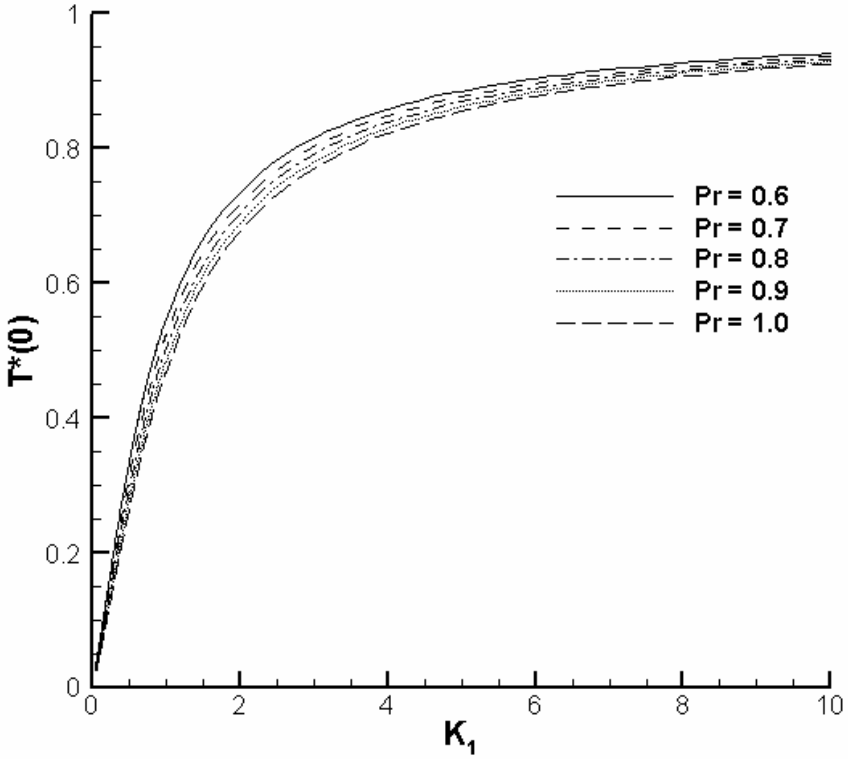

Figure 2.17. T*(0) vs. K_1 for $\gamma = 4/3$

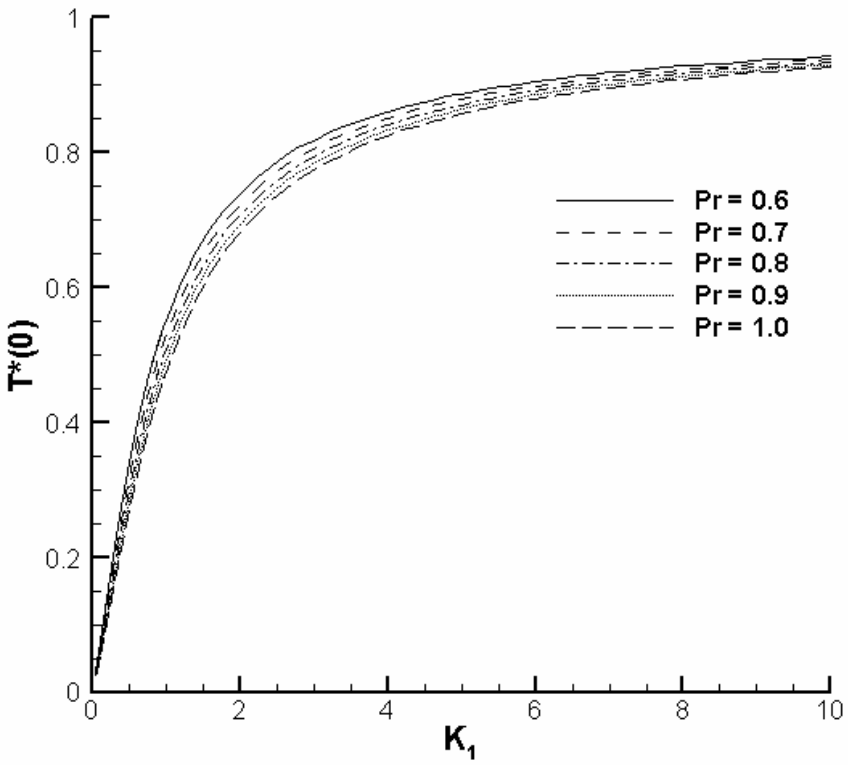

Figure 2.18. T*(0) vs. K_1 for $\gamma = 1.4$

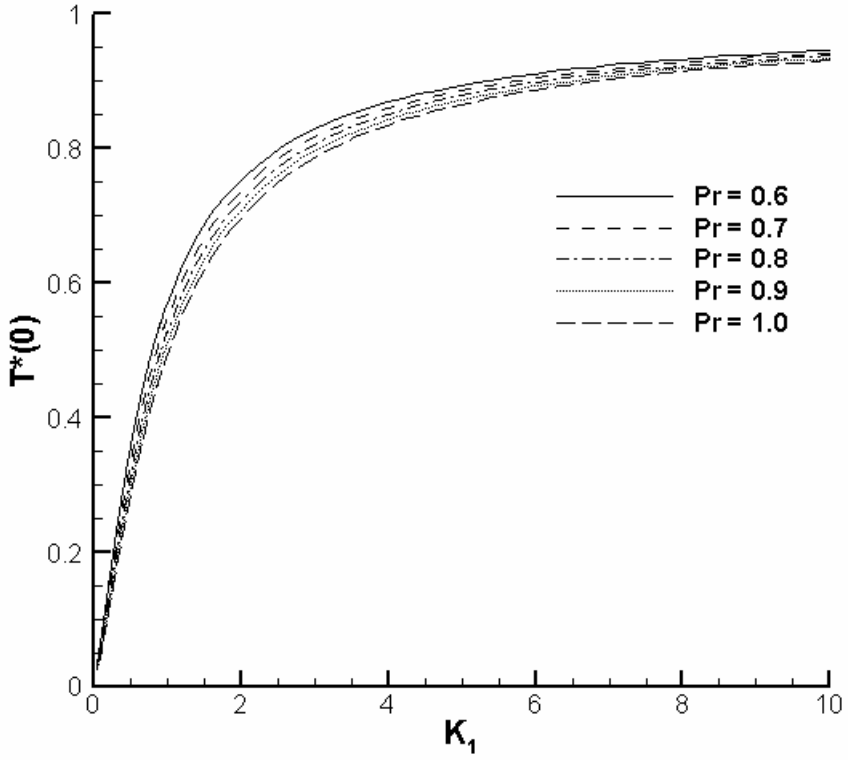

Figure 2.19. T*(0) vs. K_1 for $\gamma = 5/3$

The heat transfer coefficient h is proportional to the local temperature derivative at the wall:

$$h = \frac{q_s''}{T_s - T_\infty} = \frac{T_\infty - T_\infty}{T_s - T_\infty} k \left.\frac{\partial T^*}{\partial y}\right|_{y=0} = k\left(\frac{\rho u_\infty}{\mu x}\right)^{1/2} \left.\frac{dT^*}{d\eta}\right|_{\eta=0} \tag{2.59}$$

For the no-slip condition, the local temperature derivative at the wall approximated by the following correlation:

$$\left.\frac{dT^*}{d\eta}\right|_{\eta=0} = 0.332\,\mathrm{Pr}^{1/3} \tag{2.60}$$

Figures 2.20, 2.21, and 2.22 show the wall temperature derivative as a function of K_1 and Pr for values of γ of 4/3, 1.4, and 5/3. As with the wall temperature results, the non-dimensional temperature derivative changes noticeably with Prandtl number. The effect of varying specific heat ratio is negligible.

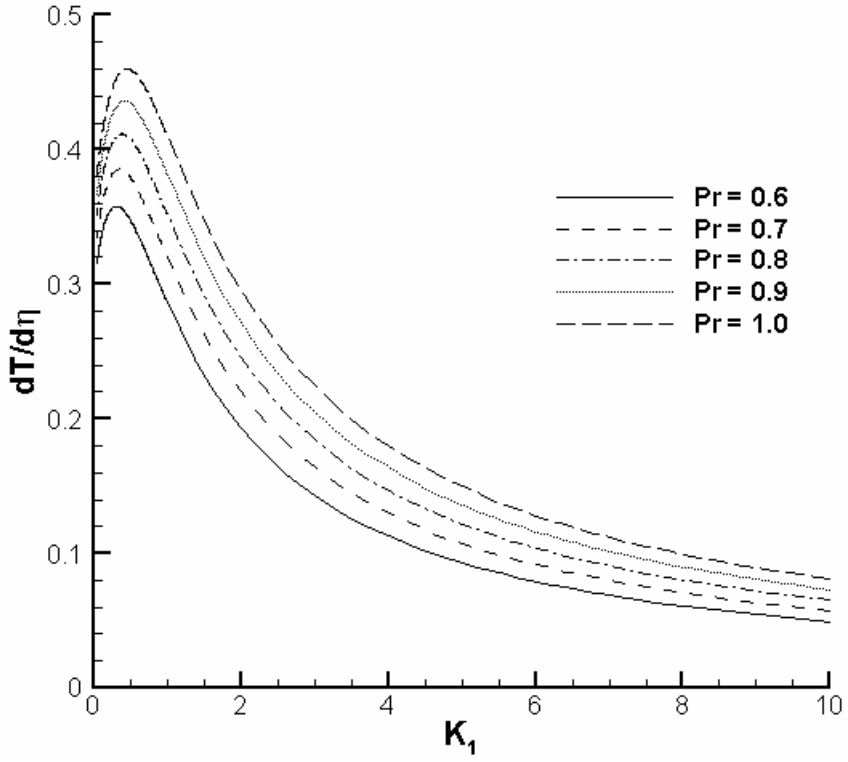

Figure 2.20. dT*(0)/dη vs. K_1 for γ = 4/3

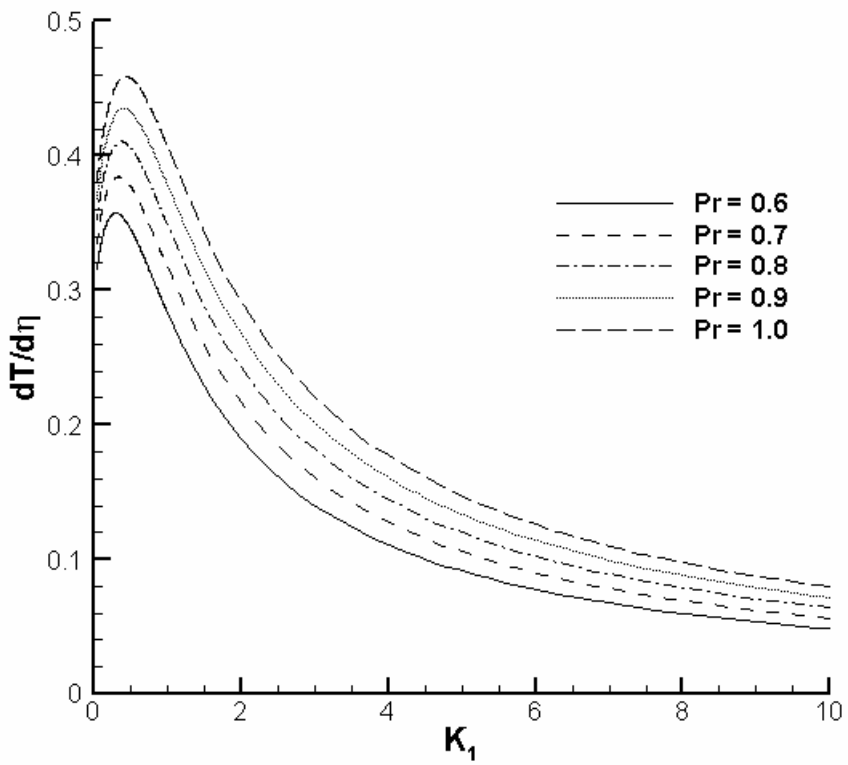

Figure 2.21. dT*(0)/dη vs. K_1 for γ = 1.4

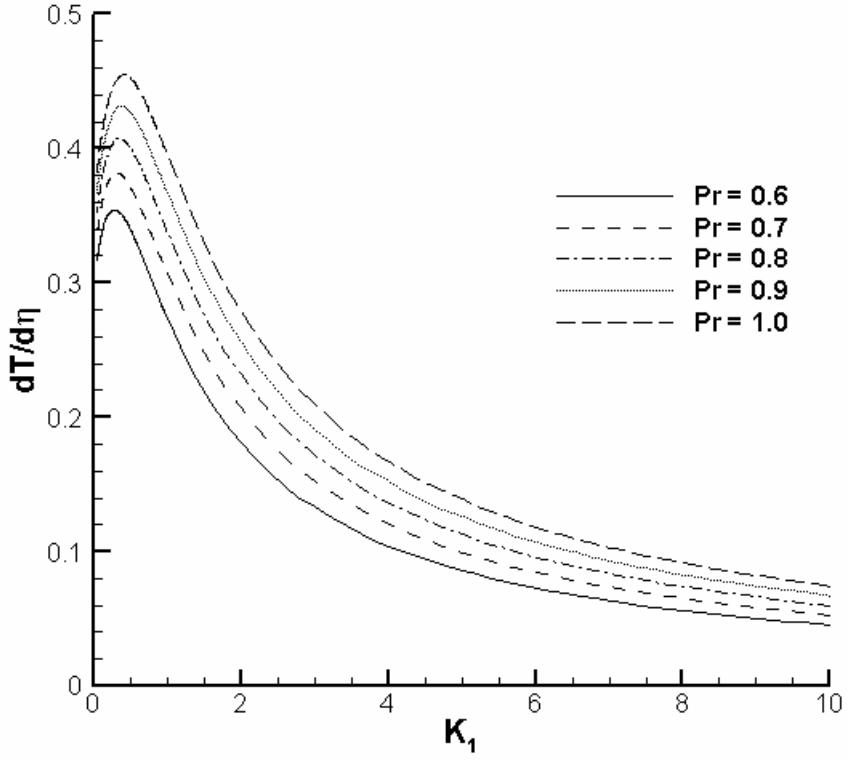

Figure 2.22. dT*(0)/dη versus K_1 for γ = 5/3

When these results are compared with the no-slip results, it is clear that heat transfer at the wall will decrease in highly rarefied flows, and increase under moderately rarefied conditions. For slightly rarefied flows, the increased velocity near the surface more than offsets the reduced heat transfer due to the temperature jump. For flows with larger Knudsen numbers, the heat transfer result is dominated by the temperature jump condition. The decreased heat transfer at higher Knudsen numbers agrees qualitatively with experimental results for heat transfer in heated cylinders at Knudsen numbers of 0.2 and less (Baldwin, 1960).

In order to find the total heat transfer within the rarefied boundary layer, we integrate over the entire plate:

$$\bar{h} = \frac{1}{L}\int_o^L k\left(\frac{u_o}{\upsilon x}\right)^{1/2} \frac{dT^*(0)}{d\eta}\, dx \tag{2.61}$$

Substituting the definition of K_1 into equation (2.60) transforms the equation into:

$$\overline{Nu}_L = 2\,\mathrm{Re}_L^{1/2}\, K_1 \int_{K_1}^{\infty} \frac{dT'(0)}{K_1^2}\, dK_1 \tag{2.62}$$

Figure shows values of this integral as a function of K_1 and Pr. Because previous result show that the effect of specific heat ratios is negligible, only one plot is shown.

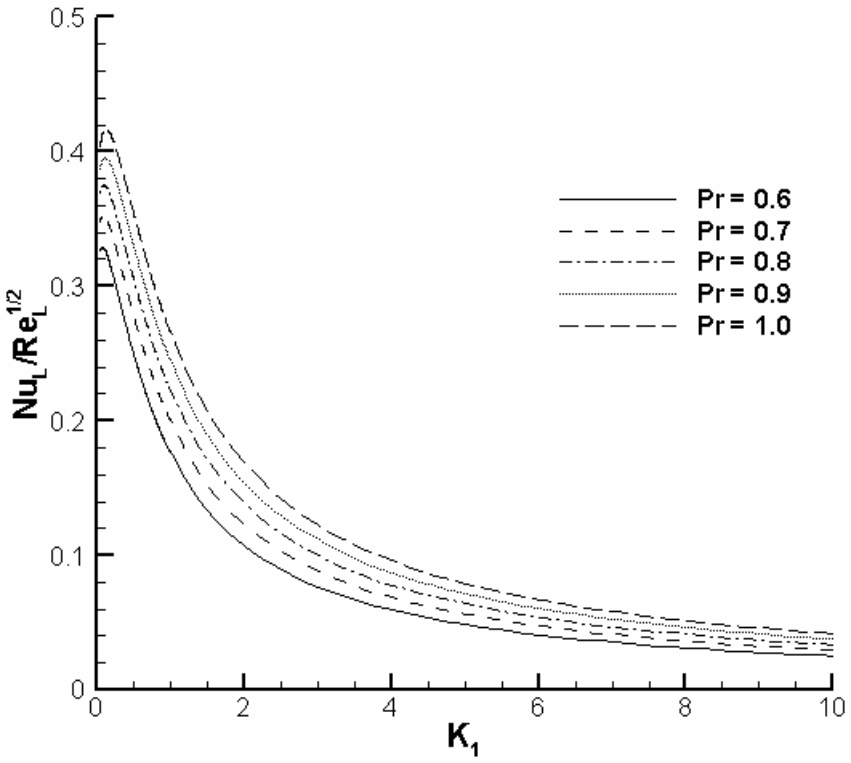

Figure 2.23. Average Nusselt Number versus K_1

These results can be compared with the no-slip value for Nusselt Number:

$$\overline{Nu}_L = 0.664\,\mathrm{Re}_L^{1/2}\,\mathrm{Pr}^{1/3} \tag{2.63}$$

Equation 2.63 gives the values for the Nusselt Number shown in table 2.3:

Prandtl Number	$Nu_L/Re_L^{1/2}$
0.6	0.5600
0.7	0.5896
0.8	0.6164
0.9	0.6411
1	0.6640

Table 2.3. No-Slip Values of Nusselt Number for Boundary Layer Flows

When the result in table 2.3 are compared to figure 2.23 shows that the change in heat transfer for a slip boundary layer can be 35 percent compared to equilibrium values. While local heat transfer increases in moderately rarefied regions, the thermal jump term

causes the local heat transfer to decrease in highly rarefied regions. When integrated, this generally causes a decrease in average heat transfer.

2.9.2. Heat Transfer in Liquid Flows with Slip

For liquid flows with slip, there will be no temperature jump, and the temperature boundary condition at the wall will be the same as for non-slip flows:

$$T^*(\eta = 0) = 0 \tag{2.64}$$

Using this boundary condition will require a new thermal boundary condition for flows with large slip velocities. If we assume that the slip velocity is equal to the free-stream velocity, the velocity approaches uniform flow, and the steady-state energy equation becomes

$$\frac{\partial^2 T^*}{\partial \eta^2} + \frac{\mathrm{Pr}}{2}\eta\frac{\partial T^*}{\partial \eta} = 0 \tag{2.65}$$

This equation can be solved as an ordinary differential equation. The solution to this equation is used as the boundary condition at large values of K_1:

$$T^*(K_1 \to \infty) = erf\left[\sqrt{\mathrm{Pr}}\,\eta/2\right] \tag{2.66}$$

Using these boundary conditions, the heat transfer of a liquid boundary layer with wall slip was computed for Prandtl numbers of 1.0, 2.0, 3.0, 4.0, and 5.0. These Prandtl numbers were selected to cover the wide range of Prandtl numbers encountered in liquids. The derivative of temperature at the wall as a function of K_1 is shown as figure 2.24:

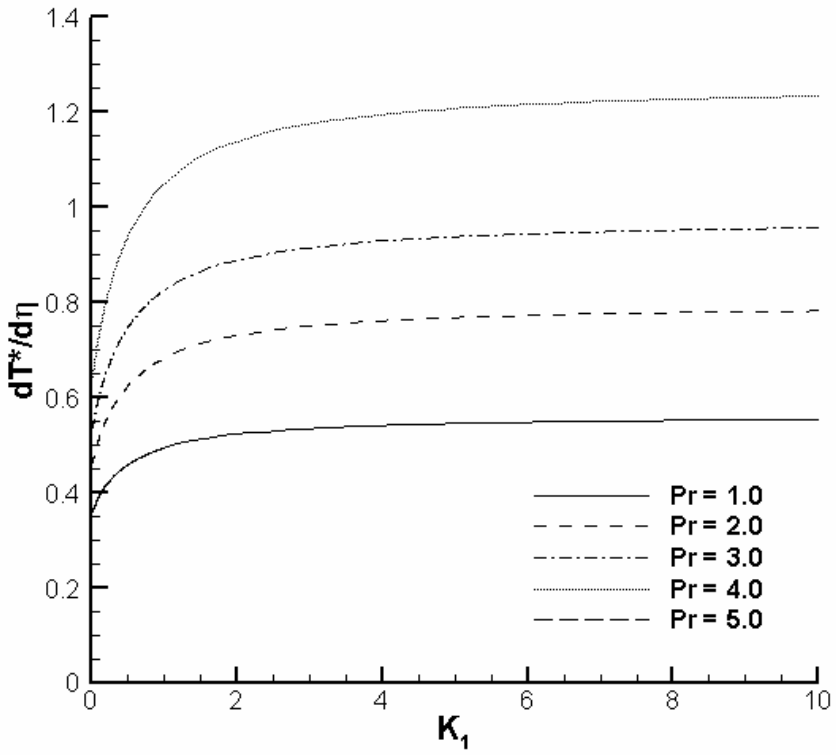

Figure 2.24. dT*(0)/dη verses K_1 for Liquid Flows

Figure 2.24 shows that for a slip flow without a temperature drop, the derivative at the wall, and the wall heat transfer, will always increase as a result of slip. Figure 2.25 shows a similar trend for the average heat transfer over the entire surface:

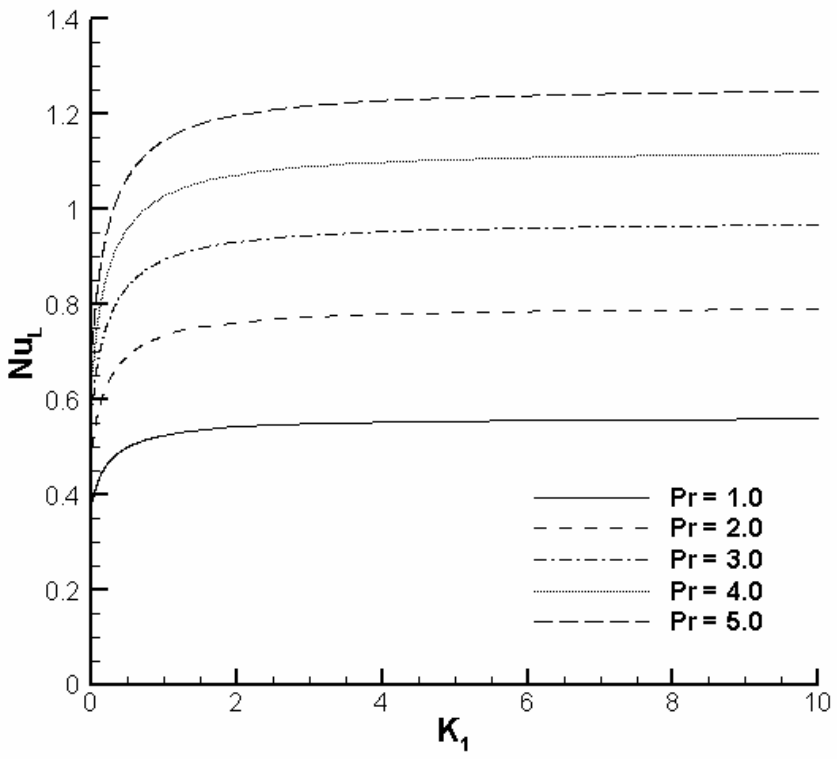

Figure 2.25. Average Nusselt Number versus for Liquid Flows

2.10. Solution of Boundary Layer Slip for Complex Geometries

The solution procedures outlined here may be expanded to cover other cases of a boundary layer with slip. The Blasius solution described in this chapter is a special case of a class of flows known as Falkner-Skan flow, which can also be solved using boundary layer methods. (Falkner and Skan, 1931)

2.10.1. Revisions to the Governing Equations

As shown in Figure 2.26, flow over the top of a wedge can be modeled as an external flow U(x) with a pressure gradient given by the inviscid flow solution. The angle of the wedge is given as $\beta\pi$.

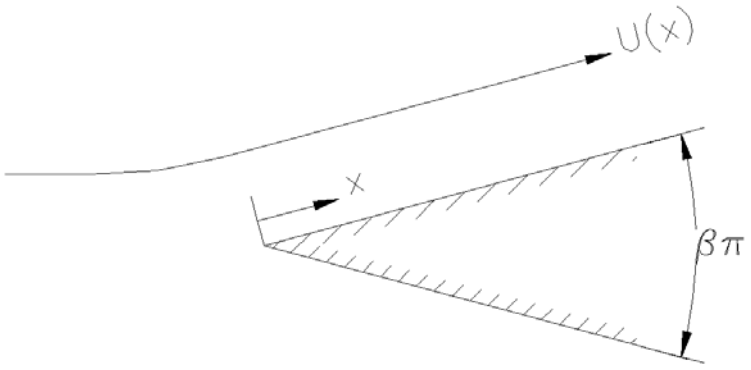

Figure 2.26. Boundary Layer Flow Over a Wedge

The external flow velocity and pressure gradients are given by:

$$U(x) = u_1 x^m \tag{2.67}$$

$$\frac{\partial P}{\partial x} = -\rho U(x)\frac{dU(x)}{dx} = -m\rho u_1^2 x^{2m-1} \tag{2.68}$$

where U is the external velocity, P is the pressure, ρ is the density, and x is the position along the wedge. The coefficient u_1 is a function of the flow geometry.

The exponent m is a function of the angle β:

$$m = \frac{\beta}{2-\beta} \tag{2.69}$$

The flow near the wedge is governed by the boundary layer equations. The equation for continuity is identical to the flat-plate case:

$$\frac{\partial u}{\partial x} + \frac{\partial v}{\partial y} = 0 \tag{2.3}$$

The momentum equation includes a term for the pressure gradient, which is now non-zero:

$$u\frac{\partial u}{\partial x}+v\frac{\partial u}{\partial y}=-\frac{1}{\rho}\frac{dP(x)}{dx}+\upsilon\frac{\partial^2 u}{\partial y^2} \tag{2.70}$$

These equations can then be transformed, using the non-dimensionalizations and non-dimensional stream functions developed by Falkner and Skan. These non-dimensionalizations are similar to, but not identical to, those used by Blasius. A non-dimensional flow coordinate η is formed by combining x and y with the other flow variables:

$$\eta = y\sqrt{\frac{m+1}{2}\frac{u_1}{\upsilon}}x^{\frac{m-1}{2}} \tag{2.71}$$

The non-dimensional stream function $f(\eta)$ is found from the dimensional stream function ψ:

$$\psi(x,y)=\sqrt{\frac{2}{m+1}}\sqrt{u_1\upsilon}x^{\frac{m+1}{2}}f(\eta) \tag{2.72}$$

The non-dimensional velocities are given as:

$$u^*=\frac{u}{U(x)}=f'(\eta) \tag{2.73}$$

$$v^*=\frac{v}{\sqrt{\frac{2}{m+1}\upsilon u_1 x^{m-1}}}=\left[f(\eta)-\frac{m-1}{m+1}\eta f'(\eta)\right] \tag{2.74}$$

A governing equation for f can be found by substituting these non-dimensionalizations into the x-momentum equation (5):

$$f'''(\eta)+f(\eta)\,f'(\eta)+\beta(1-(f'(\eta))^2)=0 \tag{2.75}$$

The boundary conditions are identical to those of the flat-plate case. However, the scaling of the non-equilibrium parameter changes slightly:

$$f'(0) = \frac{(2-\sigma_M)}{\sigma_M}\sqrt{\frac{\mathrm{m}+1}{2}}\ \frac{\lambda}{\mathrm{x}}\sqrt{\frac{\mathrm{x}U(\mathrm{x})}{\upsilon}}\ f''(0) = \mathrm{K}\ f''(0) \tag{2.76}$$

The new non-equilibrium parameter K is defined as:

$$K = \frac{(2-\sigma_M)}{\sigma_M}\sqrt{\frac{\mathrm{m}+1}{2}}\ \frac{\lambda}{\mathrm{x}}\sqrt{\frac{\mathrm{x}U(\mathrm{x})}{\upsilon}} = \frac{(2-\sigma_M)}{\sigma_M}\sqrt{\frac{\mathrm{m}+1}{2}}\ \lambda\sqrt{\frac{\mathrm{u}_1}{\upsilon}}x^{\frac{m-1}{2}} \tag{2.77}$$

Just as in the flat plate case, the revised boundary condition suggests that self-similarity will be lost, and the velocity will be a function of both η and K. While the definition of u* is unchanged, the definition of v* must be modified to incorporate the derivative of the stream function with respect to K. The revised definition of v* is

$$v^* = \frac{v}{(\upsilon U(\mathrm{x})/x)^{1/2}} = -\left[\frac{m-1}{m+1}\left(\eta\frac{\partial f(\eta,K)}{\partial\eta} + K\frac{\partial f(\eta,K)}{\partial K}\right) + f(\eta,K)\right] \tag{2.78}$$

When all other derivatives in x are re-written to include a K term, the ordinary differential equation given in (2.74) is replaced by a partial differential equation:

$$\frac{\partial^3 f}{\partial\eta^3} + f\frac{\partial^2 f}{\partial\eta^2} + \beta\left(1-\left(\frac{\partial f}{\partial\eta}\right)^2\right) + K(1-\beta)\frac{\partial}{\partial\eta}\left[\frac{\partial f}{\partial\eta}\frac{\partial f}{\partial K}\right] = 0 \tag{2.79}$$

Equation (2.78) uses the same boundary conditions as the flat-plate case.

Stagnation flow is a special case of Falkner-Skan flow. At β =1, stagnation flow is recovered. When this happens, the final non-equilibrium term disappears, making (2.79) into an ordinary differential equation identical to the no-slip governing equation:

$$f''' + ff'' + 1 - f'^2 = 0 \tag{2.80}$$

Inspection of the definition of K shows that when m is equal to 1, K is independent of x:

$$\mathrm{K}_1 = \frac{(2-\sigma_M)}{\sigma_M}\sqrt{\frac{1+1}{2}}\frac{\lambda}{\mathrm{x}}\sqrt{\frac{\mathrm{xu}_1 x^1}{\upsilon}} = \frac{(2-\sigma_M)}{\sigma_M}\lambda\sqrt{\frac{\mathrm{u}_1}{\upsilon}} \tag{2.81}$$

These results suggest that stagnation flow is in fact self-similar under rarefied flow conditions. Analysis of a stagnation point with a no-slip condition shows that the boundary layer thickness is constant. Because the boundary layer thickness is constant, the velocity gradient at the wall, and the amount of slip, will also be constant.

For a stagnation point flow, the solution to the boundary layer equations is also a solution of the full Navier-Stokes equations (White, 1991). This suggests that the results of this analysis are also a solution of the Navier-Stokes equations for the stagnation point.

2.10.2. Numeric Formulation

Equation (2.78) can be solved by modifying the boundary layer solver used for the flat-plate case. Equation (2.26) is replaced by the following expression:

$$\begin{aligned} f_{i-1,j} = {} & f_{i,j} + \frac{f'_{i,j-1}}{f'_{i,j}}\left(f_{i-1,j-1} - f_{i,j-1}\right) \\ & + \frac{2\Delta K}{(1-\beta)Kf'_{i,j}}\left(\begin{array}{l} \dfrac{f'_{i,j+1} - 2.0\,f'_{i,j} + f'_{i,j-1}}{\Delta\eta} \\ + \dfrac{f_{i,j}}{4.0}\left(f'_{i,j+1} - f'_{i,j-1}\right) \\ + \dfrac{\beta\Delta\eta}{2}\left(1 - (f'_{i,j})^2\right) \end{array}\right) \end{aligned} \tag{2.82}$$

No other changes are needed to the solution procedure.

2.10.3. Fluid Flow Results

Figure 2.27 shows the non-dimensional wall slip velocity as a function of K for a flat plate, selected wedge angles, and the stagnation region. These results show that non-equilibrium effects actually appear to increase in importance as the angle of attack increases, suggesting that the importance of slip increases in complex geometries.

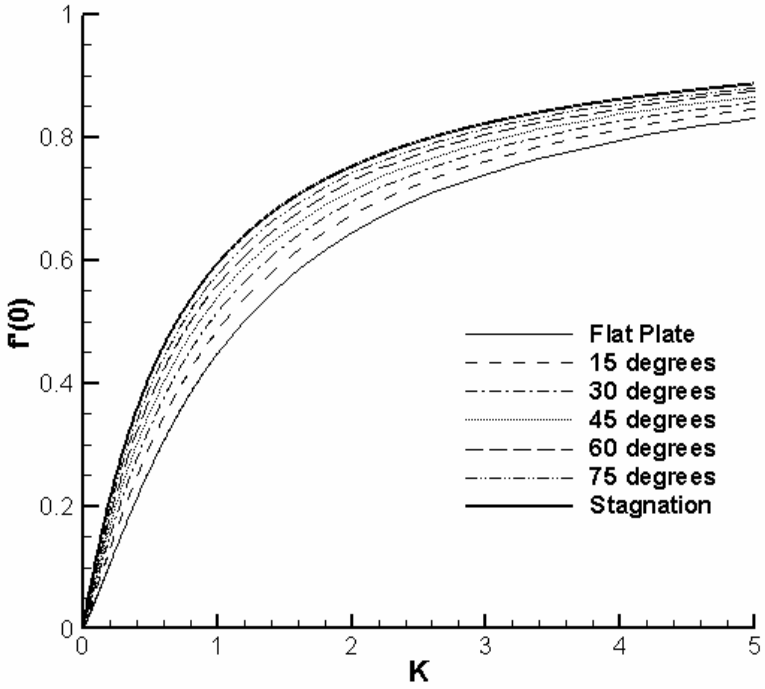

Figure 2.27. Non-Dimensional Wall Velocity as a Function of K

Figure 2.28 shows the non-dimensional skin friction as a function of K. These results show that the apparent decrease in skin friction due to rarefaction increases with increasing wedge angle. They also show that the local maximum seen in the flat plate cases disappears with increasing angle.

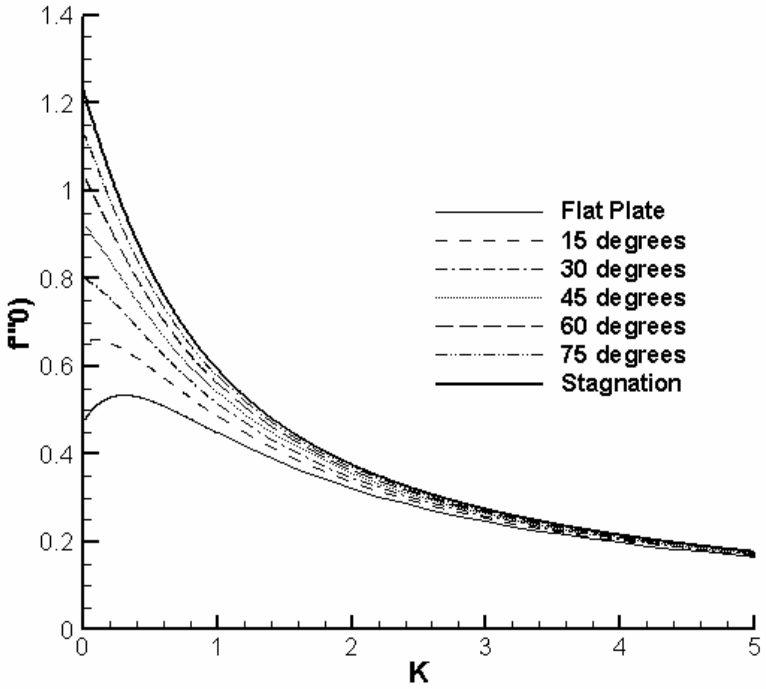

Figure 2.28. Non-Dimensional Wall Friction as a Function of K

Figures 2.29 through 2.31 show the non-dimensional boundary layer thickness, velocity thickness, and momentum thickness for the wedge flow. The results generally agree with the wall velocity and skin friction results, in that they show that the effects of the slip boundary condition increase with increasing wedge angle.

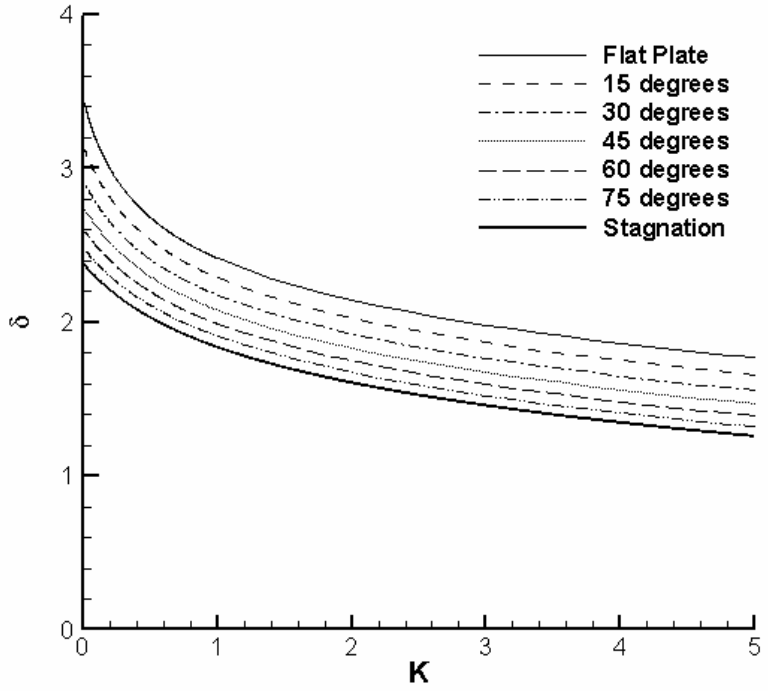

Figure 2.29. Boundary Layer Thickness as a Function of K

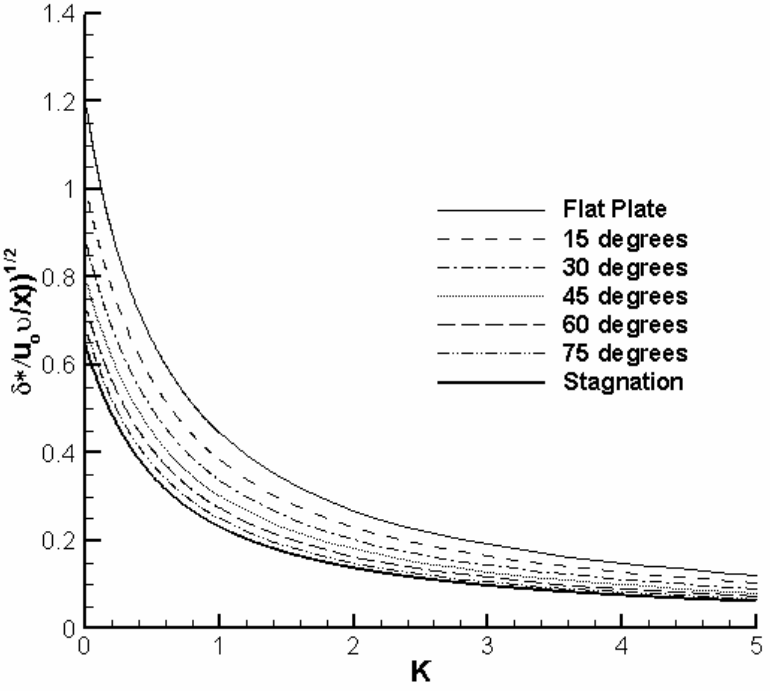

Figure 2.30. Velocity Thickness as a Function of K

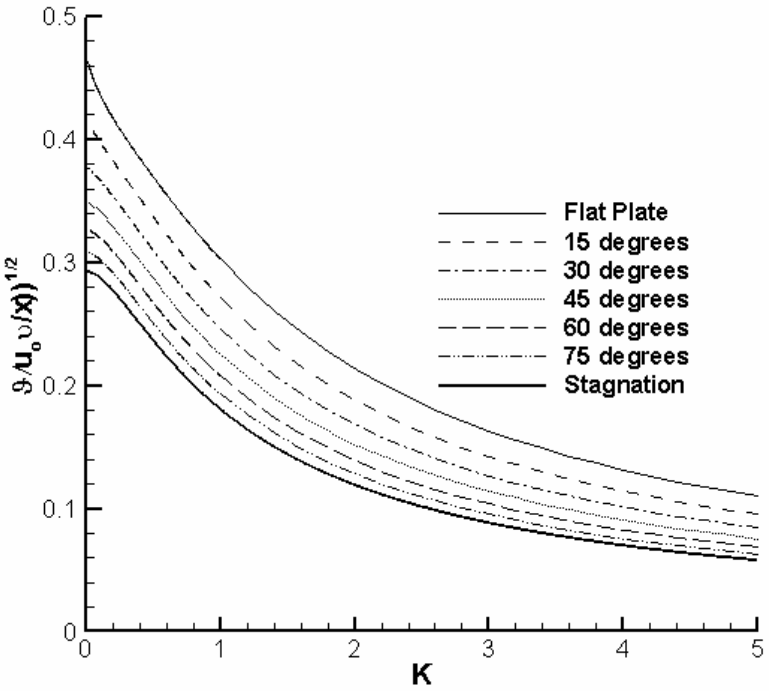

Figure 2.31. Momentum Thickness as a Function of K

2.11. Conclusions

Based on these results, the boundary layer equations can be solved for slip-flow conditions. The boundary layer loses the self-similarity of the no-slip Blasius solution. The loss of self-similarity leads to an increase in skin friction under some conditions. The heat transfer increases due to slip effects. However, the corresponding thermal jump from non-equilibrium effects in gases limits this increase. The boundary layer grows at a slightly slower rate than for the no-slip solution. The results for skin friction and heat transfer contradict previous results obtained using perturbation theory (Lin, 1951, Kogan, 1969). This discrepancy is explained by the fact that the classical perturbation analysis did not incorporate the two-dimensional nature of the flow. Similar results are obtained for wedge flows and stagnation flows, with the relative importance of slip effects increasing with the angle of the wedge. These results can be applied to analyze a variety

of systems, including potential micro-device designs, and flight in low-density atmospheres.

These results allow us to select the test conditions under which continuum breakdown may occur for micro-scale airfoils. Using the scaling of K_1 for a flat plate, we would expect slight continuum breakdown at a velocity of 30 m/s, a pressure of 1.0 atm, and a chord of 100 microns. Increasing the velocity, decreasing the pressure, and decreasing the chord will all increase the non-equilibrium effects present in the flow. These results can then be used to select test conditions for operating a facility of micro-scale aerodynamics.

CHAPTER 3

EXPERIMENTAL FACILITY DESIGN

3.1 Introduction

To allow testing of lift and drag at the micro-scale, a unique wind-tunnel facility is designed and fabricated. This chapter lays out the design requirements. It then documents the computational fluid dynamics study used to select the optimal contraction configuration. Finally, test data is used to show that the tunnel meets the design requirements.

3.2 Facility Requirements

In order to carry out the desired measurements, the facility must meet the following requirements:

1. To allow independent control of Knudsen number and Reynolds number, the facility must allow the pressure to be varied from 0.15 to 1.0 atmospheres, with a velocity range of 30 to 100 m/s. These values of pressure and velocity were selected to allow measurement of the rarefied flow effects calculated in chapter 2, while avoiding compressible flow effects.
2. Turbulence intensity should be kept as close to zero as possible for these experiments, to allow easier comparison of results, and to avoid velocity fluctuations within the system that may be of the same order of magnitude as the slip velocities at the surface of the airfoil. As a design goal, the turbulence intensity should be kept to less than 0.5% at all velocities and pressures.

3. The velocity profile in the test section should be kept as uniform as possible, with a minimal boundary layer thickness along the wall.
4. As will be shown in Chapter 4, the maximum allowable span for the microfabricated flat-plate airfoils is approximately 1 cm. This is based on a structural analysis of the micro-scale airfoils. To allow the airfoil to use sidewall mounting of the sensors, the width of the test section will be set at 1 cm.

3.3. Facility Configuration

A schematic of the facility is shown in figure 3.1:

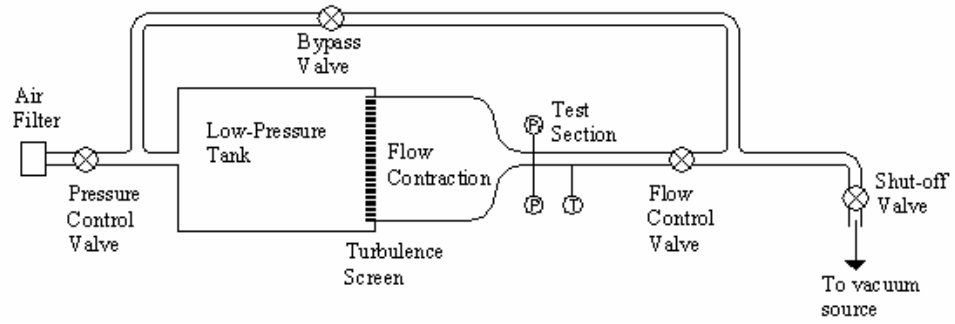

Figure 3.1. Schematic of Test Facility

The tunnel is a draw-through wind-tunnel. Air is drawn from the ambient environment and passed through a filter to protect against particles from the environment. The air goes through a pressure control valve, and is drawn into a low-pressure tank. Experience with the tunnel showed that a bypass valve was needed to obtain low-pressure, low velocity flow conditions. Air is then drawn through a turbulence screen, and into a flow contraction. The test section is mounted immediately downstream of the contraction. A second valve was mounted downstream of the test section to control the velocity. The air was then drawn off to a central vacuum system.

The two-valve system, with the first valve controlling pressure, and the second valve controlling velocity, was the only reliable way of independently controlling pressure and velocity. Once the bypass was installed, the velocity could be changed without re-adjusting the upstream pressure valve.

The small size of the test section allows for conventional methods of turbulence control to be carried to their limits. Both theoretical (Batchelor, 1953) and experimental (Uberoi, 1956) studies have shown that streamwise turbulence is reduced by contractions in the flow. Typical wind-tunnel facilities use a 25:1 or 16:1 ratio contraction for turbulence suppression. Because of the small size of the micro-scale facility, a 100:1 ratio inlet can be used.

3.4. Turbulence Suppression Strategies

Theoretical results show that the reduction in the streamwise turbulent velocity fluctuation u' is given by:

$$\frac{\overline{u_2'^2}}{\overline{u_1'^2}} = \frac{3}{4c^2}\left[\ln(4c^3 - 1)\right] \tag{3.1}$$

where u_1' is the pre-contraction turbulent streamwise fluctuation, u_2' is the post-contraction turbulent fluctuation, and c is the area ratio (Batchelor, 1953) . For a 100:1 reduction, we expect the rms fluctuations to decrease by a factor of 0.022.

This model indicates that the normal turbulent velocity fluctuations v' and w' will increase, based on the following equation:

$$\frac{\overline{v_2'^2}}{\overline{v_1'^2}} = \frac{\overline{w_2'^2}}{\overline{w_1'^2}} = \frac{3c}{4} \tag{3.2}$$

where v_1' and w_1' are the pre-contraction turbulent normal fluctuations, and v_2' and w_2' are the post-contraction turbulent normal fluctuations. (Batchelor, 1953) For a 100-1 reduction, we would expect the rms fluctuations to increase by a factor of 8.7.

Although the high contraction ratio leads to increased normal velocity fluctuations, these can be controlled by use of a honeycomb structure, which will filter out large-scale turbulent motions, while generating small-scale turbulence. The small-scale turbulent fluctuations will dissipate downstream of the honeycomb, based on the following expression:

$$\left[\frac{q'}{U_\infty}\right]^2 = \frac{0.03}{x/D} \tag{3.3}$$

where q' is the turbulent fluctuation, U_∞ is the free-stream velocity, x is the down-stream distance, and D is the honeycomb diameter (Lumley, 1967)

The high contraction ratio leads to extremely low velocities at the inlet of the system. This means that an extremely fine honeycomb can be used without causing high pressure drops. For this facility, a honeycomb of 2.5 cm long, 0.2 cm diameter tubes is selected.

Modeling the turbulence in the facility requires an estimate of the streamwise turbulent velocity fluctuations prior to the honeycomb. In the settling chamber, the velocity will be 1 m/s or less. If we assume a turbulence intensity of 10 % in the settling chamber, then the magnitude of the fluctuations is 0.1 m/s. Because 10 % is a high level of turbulence, typical of reacting flows (Lefebvre, 1998), this is a conservative estimate. Assuming initial turbulence fluctuations of 0.1 m/s, modeling the change in u'_{rms} using equation (3.1), and modeling the changes in v'_{rms} and w'_{rms} using equations (3.2) and (3.3), we can estimate the magnitude of the turbulent fluctuations after the contraction.

For a 10 cm pre-contraction length, using a 0.2 cm diameter honeycomb, these models indicate that all turbulent fluctuations will be below 0.2 % regardless of initial velocity.

Use of the 100-1 contraction will, however, result in anisotropic turbulence, since streamwise fluctuations are damped much more effectively than normal fluctuations. Depending upon the intended application for testing, this may have a major effect on the results. For the application described here, minimizing streamwise fluctuations was held to be of much greater importance than minimizing normal fluctuations. This is because one of the objectives of the tunnel is to allow measurement as the airfoils approach the slip flow regime, where a small wall velocity may appear.

3.5. Inlet Design: CFD Results

The major challenge in design of this facility involves the shape of the contraction section. While there has been much work on the design of both axisymmetric and square wind-tunnel contractions (Mikhail, 1978), the high contraction ratio, and small size, of this contraction are unique. A commercial CFD solver (FLUENT, 1995) is used to study several 100:1 square inlet configurations, with a final width of 1 cm.

All potential configurations are studied with final velocities of 30 and 100 m/s, at a pressure of 1 atmosphere. Following the same approach as previous researchers (Mikhail, 1978), the contraction is constructed from two curves, meeting at an inflection point. All inlets use h equal to 0.01 m and h_0 equal to 0.1 m, and the length was varied from 0.45 m to 0.2 m. To simplify the analysis, the curves chosen are circles, and the inflection point is taken as the midpoint of the converging section, as shown in figure 3.2:

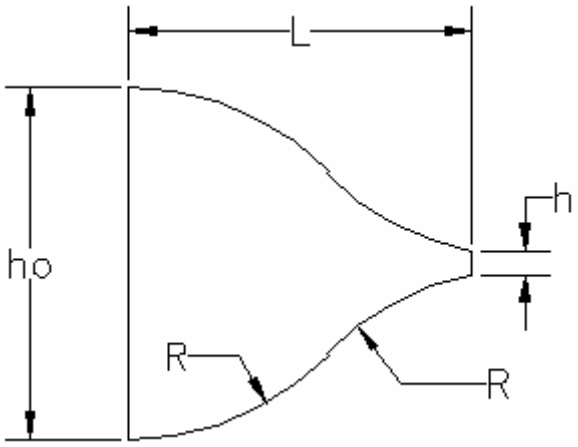

Figure 3.2. Inlet Geometry

Based on the low turbulence levels given by the analysis in section 3.4, a laminar flow solver is used to compute the flow. Initial calculations were made using a 20 by 20 by 60 mesh that included only the contraction section. Detailed calculations were made using a 20 by 20 by 100 mesh that included the upstream volume. A sample three-dimensional mesh is shown as figure 3.3. Symmetries exist in the x-y and x-z planes, allowing the tunnel to be simulated using one quarter of the total cross section. All cases use a uniform velocity inlet, and a uniform pressure outlet boundary condition. All cases were repeated using a 40 by 40 by 200 mesh, to ensure grid independence, and accurate resolution of the boundary layer.

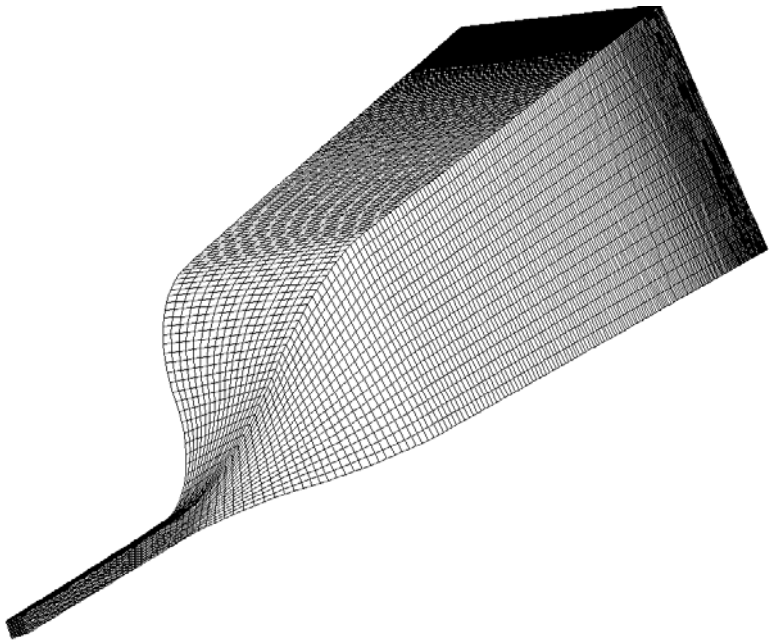

Figure 3.3. Sample Mesh

The velocity profiles 1 cm into the test section are compared based on boundary layer thickness and free-stream velocity uniformity. The position is non-dimensionalized based on the test section width:

$$y^* = \frac{y}{h} \tag{3.4}$$

where y* is the non-dimensional position. All velocities are non-dimensionalized using the following expression:

$$u^* = \frac{u}{\overline{u}} \tag{3.5}$$

where u* is the non-dimensional velocity, and $\overline{u}$ is the average velocity across the entire test section. The results for a pressure of 1.0 atm and a velocity of 100 m/s are shown in figure 3.4:

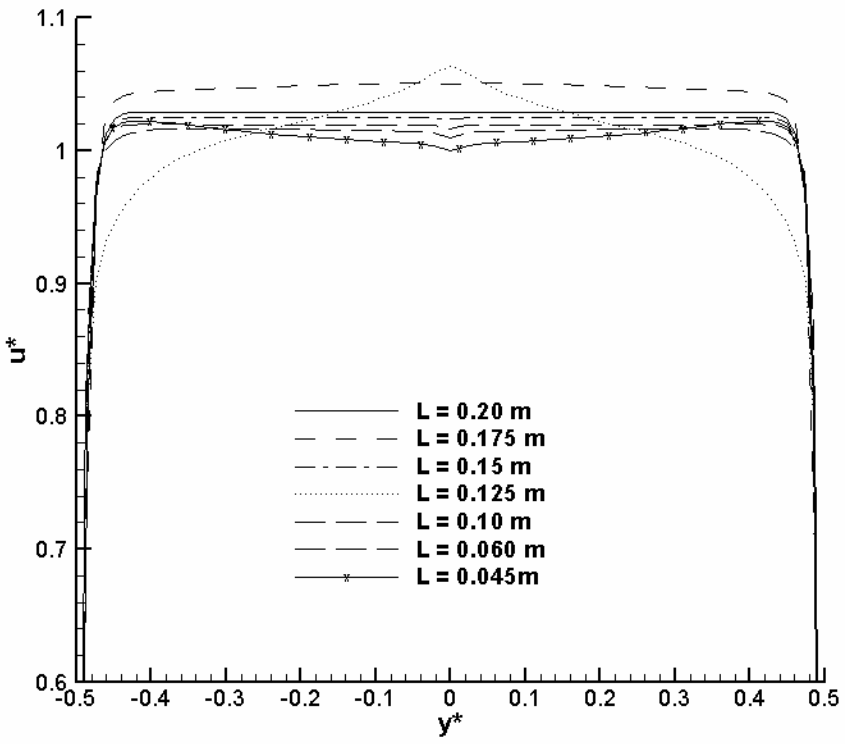

Figure 3.4. Velocity Profiles for Sample Contractions

These results show the velocity profile varies in structure based on the contraction length selected. For large contraction lengths, the core velocity overshoots the mean velocity in the test section by as much as 5 percent. As the contraction length decreases, the core velocity decreases. However, in some cases, a peak of high-velocity fluid remains at the center. This can be seen most clearly for a length of 0.125 m. As the contraction section continues to decrease, the overshoot in the core velocity decreases, and the average core velocity approaches that of the entire cross-section.

Because the results are normalized by the average velocity in the cross-section, the flow should be considered most uniform when normalized velocity is closest to unity across the entire center-line. A normalized velocity close to unity, instead of a uniform velocity above unity, means that the flow in the entire cross-section is relatively uniform.

While the airfoil will be mounted in the center slice, keeping the air velocity uniform in the entire test section reduces normal velocity components in the tunnel.

Based on these results, showing the smallest overshoot occurring for the shortest cross-section, a contraction length of 0.045 m was selected. This geometry is then re-tested for four cases: velocities of 30 and 100 m/s, and pressures of 0.1 and 1.0 atmosphere.

The results show that the shortest inlet possible is the most effective design for this application. Boundary layer growth for these conditions is a much larger concern than flow separation. Figure 3.5 shows the contours of x-velocity in a 0.045 m contraction, indicating that the fluid acceleration occurs in the second half of the contraction.

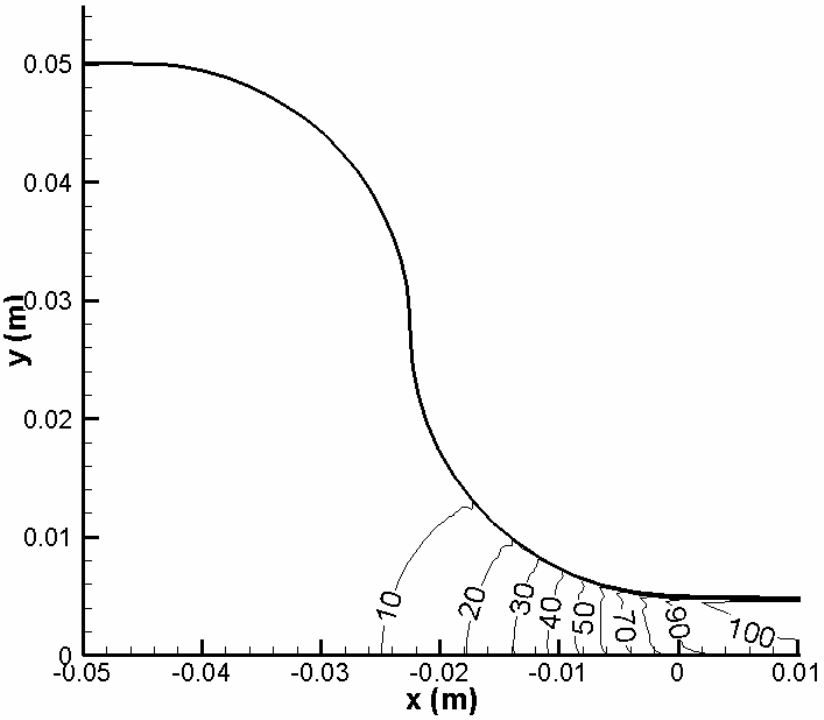

Figure 3.5. Contours of X-Velocity (m/s), Contraction Length of 0.045 m, U = 100 m/s, P = 1.0 atm

Figure 3.6 shows the streamlines for the 0.045 m contraction. These streamlines indicate that, in spite of the large change in area in a relatively short distance, there is no flow separation. The streamlines also indicate that, although a boundary layer does develop, there does remain a large core of relatively uniform flow in the system.

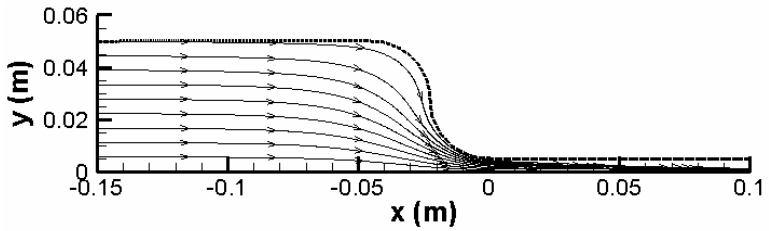

Figure 3.6. Streamlines for 0.045 m Contraction, U = 100 m/s, P = 1.0 atm

Figures 3.7 and 3.8 show the velocity profiles at the end of the contraction, and 1 cm downstream in the test section, for a contraction length of 0.045 m.

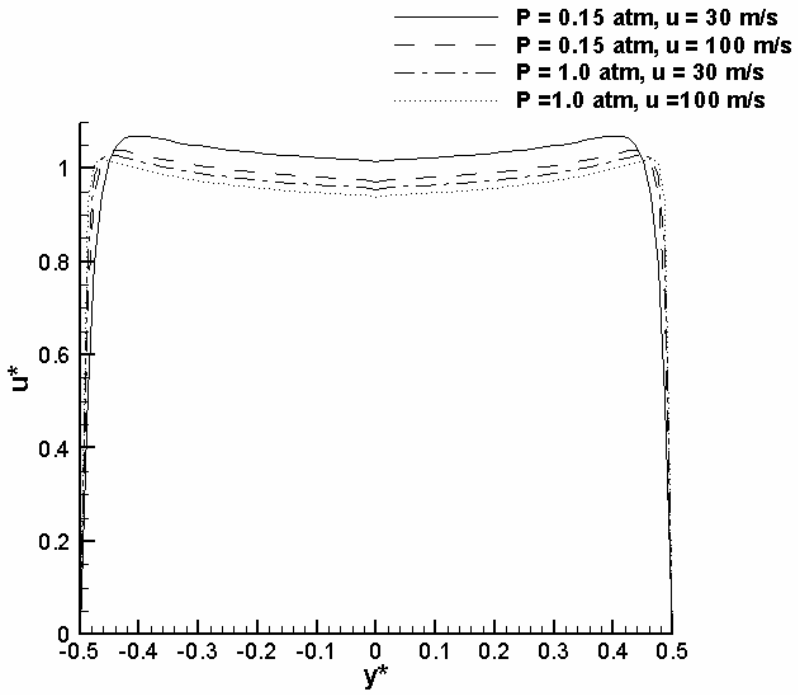

Figure 3.7. Normalized Velocity Profiles at End of 0.045 m Contraction

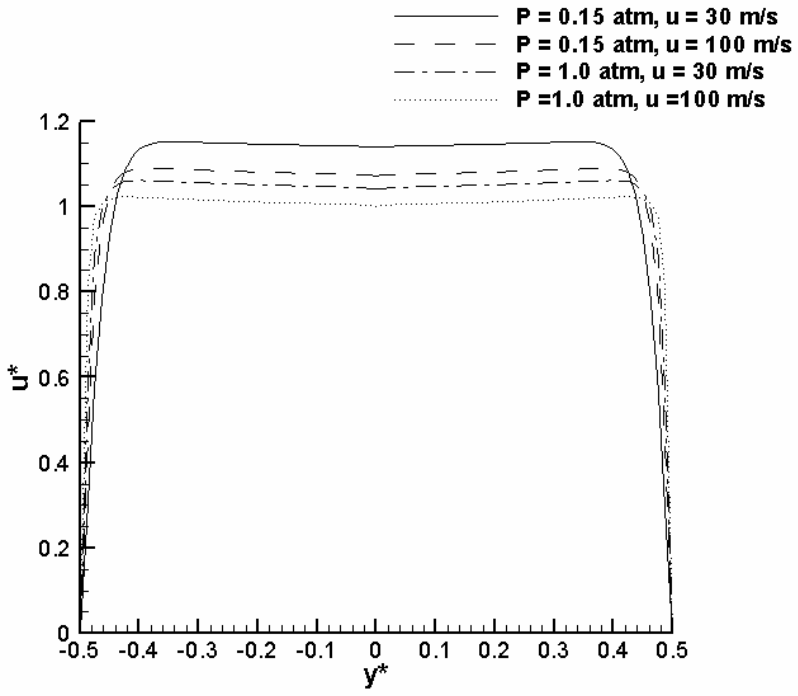

Figure 3.8. Normalized Velocity Profiles 1 cm into Test Section

These results show that the shortest possible inlet should be used for the inlet of a micro-scale wind-tunnel facility. While there is a velocity overshoot of 7 percent from the mean velocity at the end of the contraction, this smoothes out within the first 1 cm of the test section.

An additional concern was the possible appearance of corner vortices in the contraction section. The normal velocity vectors at the end of the contraction section are shown in figure 3.9. These results show a net flow from the wall area to the center of the test section, and that there is no development of corner vortices in the tunnel contraction section.

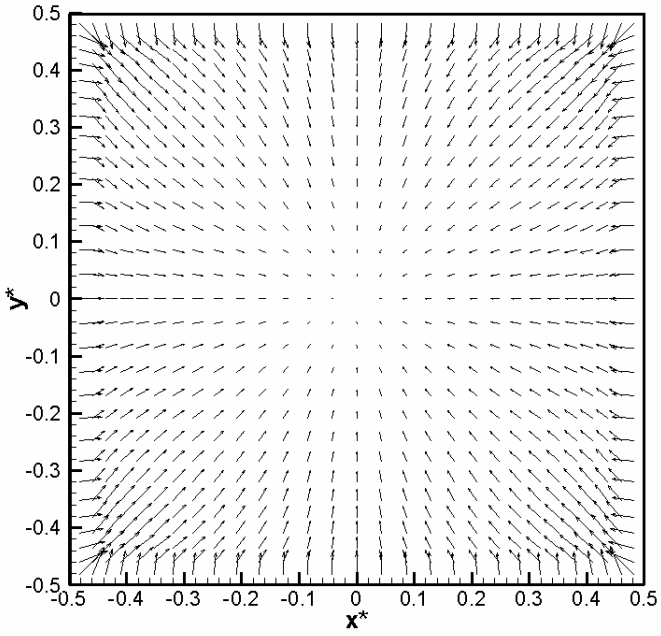

Figure 3.9. Normal Velocity Vectors at End of Contraction Section

The inlet is built using a length of 0.045 m. Additional CFD analysis on the selected design is performed to cover the entire range of pressures and velocities. The cases studied cover a range of pressures from 0.15 to 1.0 atmosphere, with a range of velocity from 10 to 100 m/s. The cases can be characterized using a channel Reynolds number, as given by equation (3.6).

$$\mathrm{Re}_h = \frac{\rho \bar{u} h}{\mu} \tag{3.6}$$

where h is the test section width, ρ is the air density, and μ is the viscosity.

Because the tunnel is designed to allow independent control of velocity and pressure, the channel Reynolds number will vary considerably. The minimum Reynolds number, at a pressure of 0.15 atmosphere, a temperature of 298 K, and a velocity of 10 m/s, is 1,010. The peak Reynolds number, at a pressure of 1.0 atmosphere and a velocity of 100 m/s, is 67,000.

For fully developed channel flows, transition to turbulence typically begins at a Reynolds number of around 2,300, and a flow is considered to be fully turbulent at a Reynolds number of 10,000. These criteria apply for both round and square channels (Schlichting, 1999). The majority of cases studied here are turbulent by these criteria. However, all CFD studies are performed using laminar flow models. The turbulence suppression system detailed earlier in this chapter is assumed to be effective enough that turbulence intensities are extremely low.

Figures 3.10 through 3.12 show the CFD velocity profiles 1 cm into the test section for pressures of 0.15 atm, 0.5 atm, and 1.0 atm, over a range from 10 to 100 m/s. All of these results show a core of uniform flow, and a boundary layer thinner than 0.0005 meters for velocities greater than 30 m/s. As expected, the boundary layer thins with increasing velocity, and increasing density.

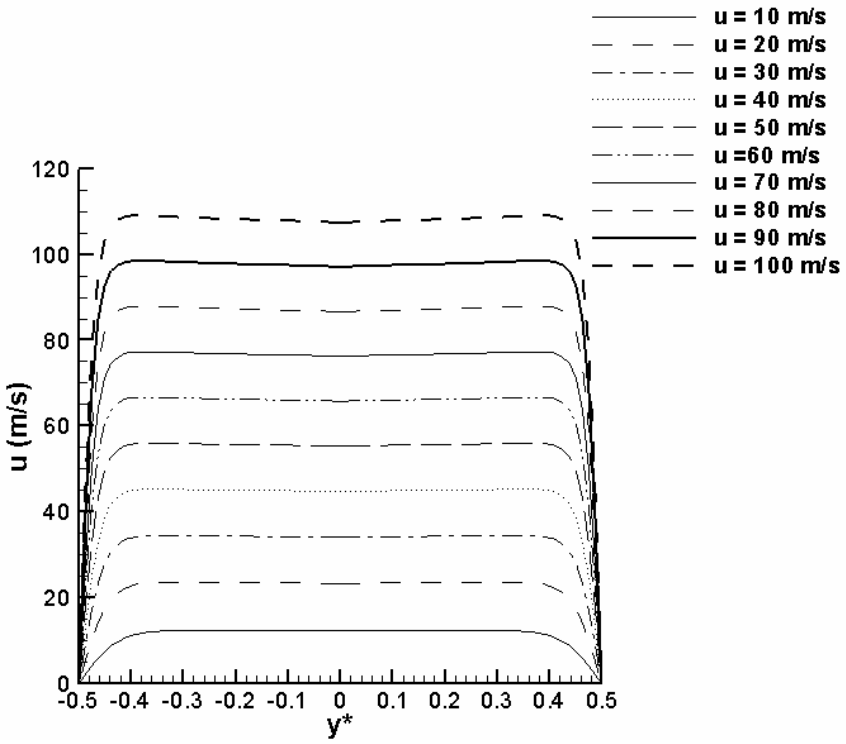

Figure 3.10. Velocity Profiles for Tank Pressure of 0.15 atm

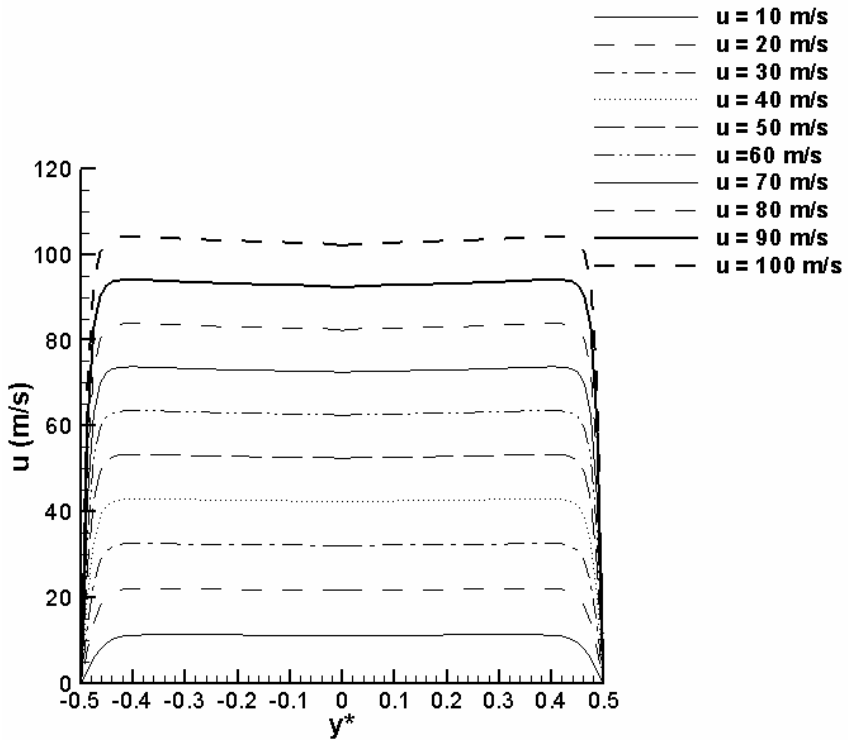

Figure 3.11. Velocity Profiles for Tank Pressure of 0.5atm

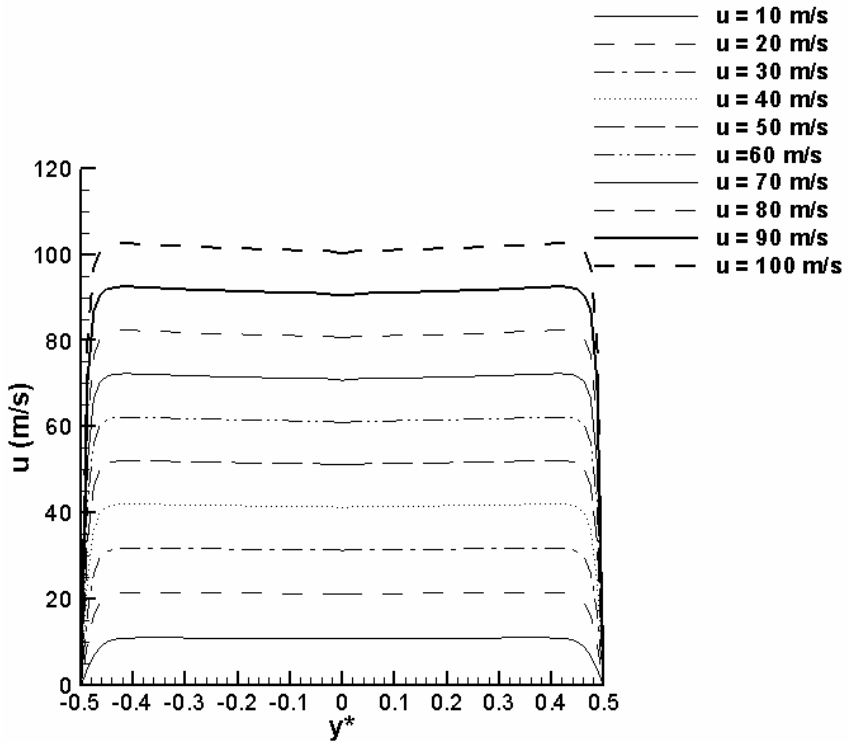

Figure 3.12. Velocity Profiles for Tank Pressure of 1.0 atm

When non-dimensionalized using average velocity and channel Reynolds number, the velocities profiles 1 cm into the test section collapsed onto each other, as shown in figure 3.13.

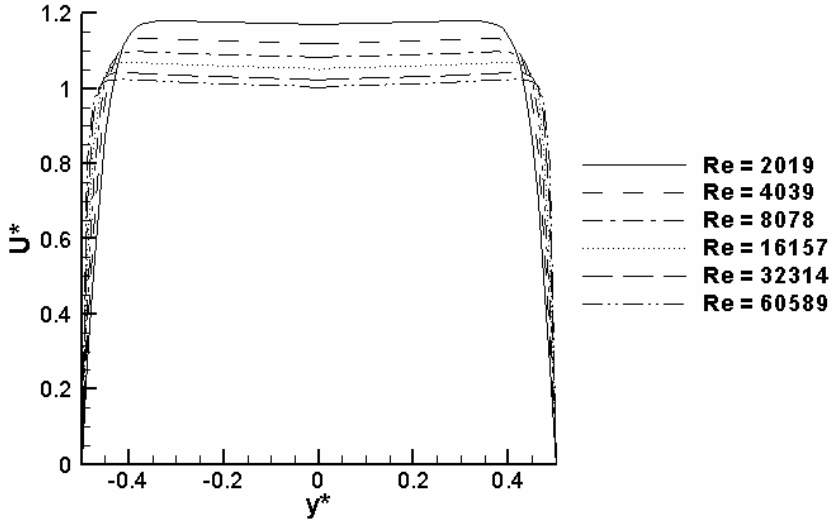

Figure 3.13. Non-Dimensional Velocity Profiles

The velocity profiles are analyzed to determine the momentum deficit, velocity deficit, and boundary layer thickness. All of these results are plotted versus the channel Reynolds Number, and provide some indication of how close the channel is to achieving the design goal of uniform flow. They also provide some indication of possible transition to turbulence within the boundary layer.

The boundary layer thickness prior to the contraction can be found by using the Blasius boundary layer theory for a flat plate:

$$\delta_1 = \frac{5.0}{\sqrt{\rho u_1 / \mu l}} \tag{3.7}$$

where δ_1 is the pre-contraction boundary layer thickness, l is the length of the settling chamber, and u_1 is the pre-contraction velocity

Assuming a constant density, u_1 can be found using continuity, leading to the expression:

$$\delta_1 = \sqrt{\frac{hc}{l}} \frac{5.0l}{\sqrt{\mathrm{Re}_h}} \tag{3.8}$$

The pre-contraction and post-contraction boundary layer thickness are shown as figure 3.14. The contraction reduces the boundary layer thickness by two orders of magnitude.

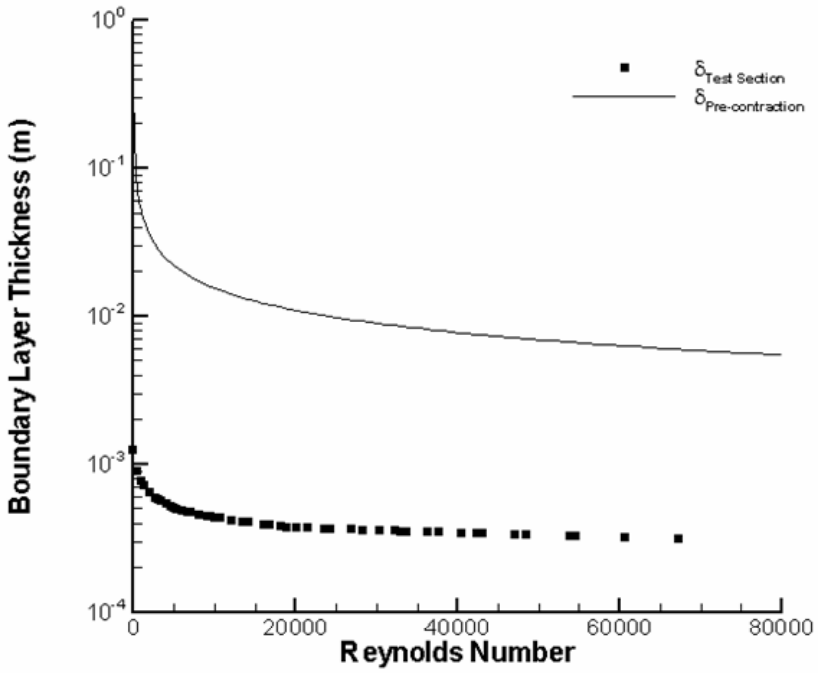

Figure 3.14. Boundary Layer Thickness versus Reynolds Number

Equation (3.9) is used to calculate the non-dimensional momentum thickness (White, 1991).

$$\theta = \int_o^{h/2} \frac{u}{u_{\max}} \left(1 - \frac{u}{u_{\max}}\right) dy \tag{3.9}$$

where θ is the momentum deficit, h is the height of the test section, and u is the downstream velocity at a given point (y).

The velocity thickness is calculated using equation (3.10) (Schlichting, 1999):

$$\delta^* = \int_o^{h/2} \left(1 - \frac{u}{u_{\max}}\right) dy \tag{3.10}$$

The momentum and velocity thickness are non-dimensionalized using the channel height, and are shown in figure 3.15:

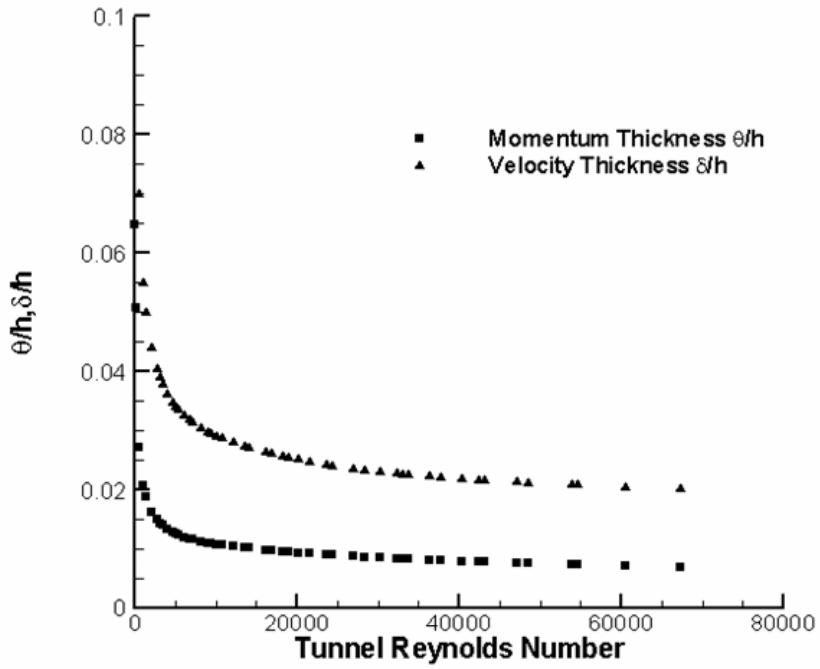

Figure 3.15. Momentum and Velocity Deficits versus Reynolds Number

The results show that the length scales of the momentum and velocity deficits are both small relative to the tunnel width, and vary predictably with Reynolds Number.

The results of this analysis can also be used to predict possible transition to turbulence within the boundary layer of the tunnel. A Reynolds number based on velocity thickness is calculated, as shown in equation (3.11):

$$\mathrm{Re}_{\delta} = \frac{\rho \bar{u} \delta^{*}}{\mu} \tag{3.11}$$

where δ^* is the velocity thickness found using equation (3.8). Re_δ as a function of tunnel Reynolds number is plotted as figure 3.16.

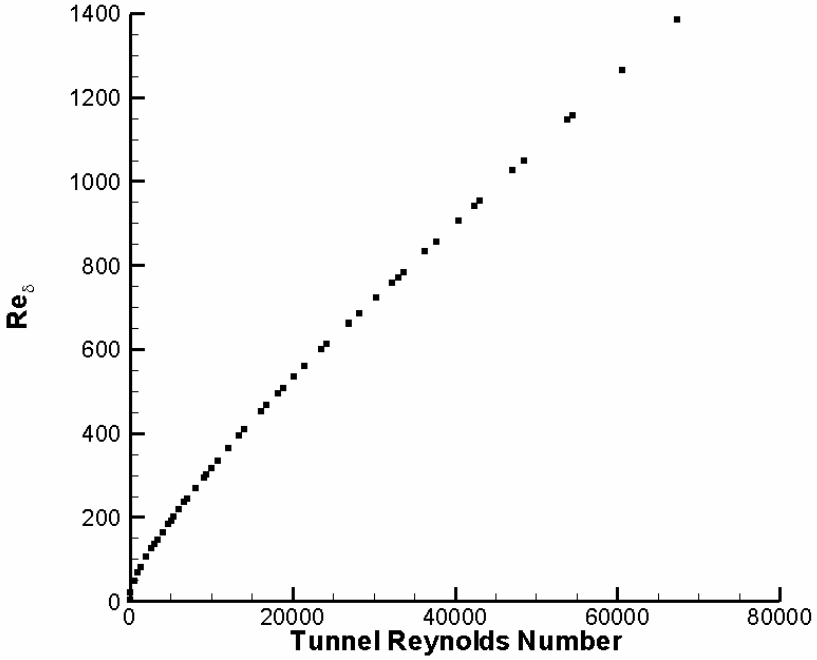

Figure 3.16. Re_δ versus Tunnel Reynolds Number

Previous researchers have found that laminar boundary layers become unstable when Re_δ approaches 520 (White, 1991). Based on these criteria, at a tunnel Reynolds number of above 20,000, the boundary layer may transition to turbulence.

These computational results show that the non-dimensional velocity profile, as well as flow characteristics such as the momentum thickness, velocity deficit, and boundary layer thickness, collapse onto the same curve based on Reynolds number. They also show that the tunnel flow is much more uniform than what would normally be expected for a channel flow.

These results show that as the airfoil Knudsen number is changed by varying tunnel conditions, the velocity profile will be identical for any given tunnel Reynolds number. This will allow results for any given Reynolds number test structure to be compared for various Knudsen numbers.

3.6.Initial Testing

3.6.1. Initial Test Configuration

The facility was initially tested without using a bypass, in the configuration shown schematically in figure 3.17:

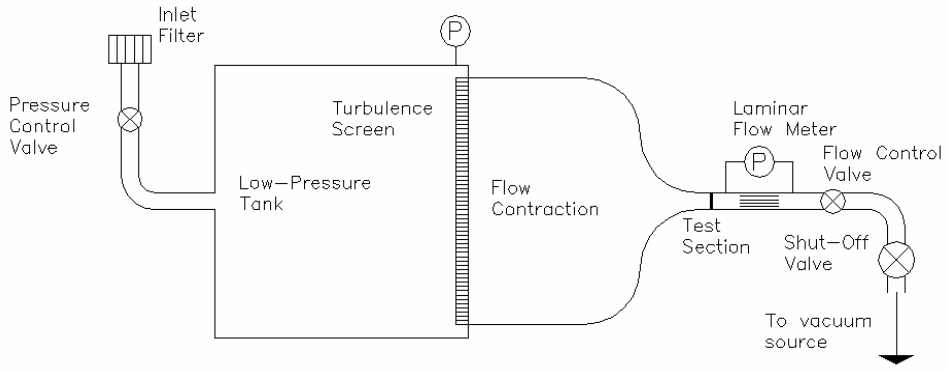

Figure 3.17. Test Section Initial Configuration

A photograph of the facility in its initial test condition is shown in Figure 3.18:

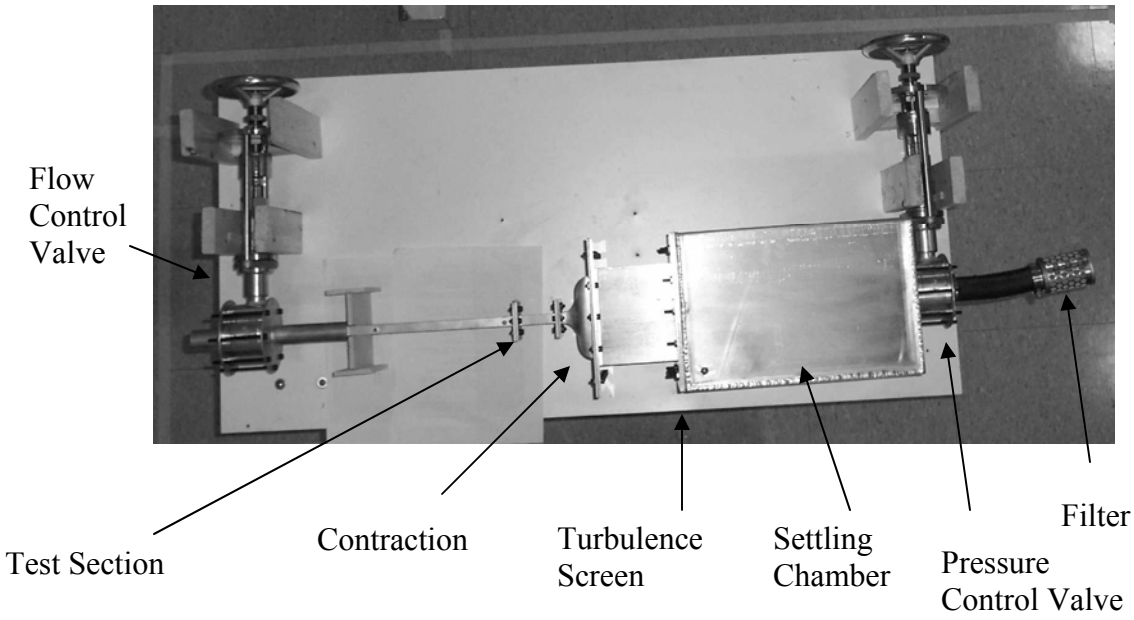

Figure 3.18. Initial Tunnel Configuration

The flow direction of the tunnel in this photograph is from right to left. The air is drawn in through a small-engine air filter, and passes through a gated flow-control valve. The air is then drawn through a 30 cm long settling chamber, with a 20 cm by 20 cm cross-section. Even at peak flow, the velocities in the settling chamber will remain below 1 m/s. At the end of the settling chamber, the air is drawn through a honeycomb of 0.2 cm diameter straws, as shown in Figure 3.19. The air then travels down a 10 cm straight section, and into the 100-1 contraction, which is shown in Figure 3.20. Immediately after the contraction is the test section. After the test section, air then flows through a second valve, used to control the flow velocity.

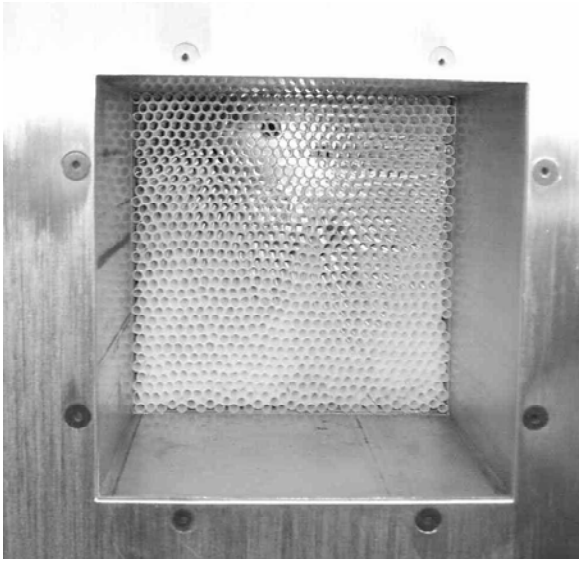

Figure 3.19. Turbulence Screen

Figure 3.20. Contraction Section

3.6.2. Initial Experimental Results

The velocity in the test section is measured 1 cm into the test section at a pressure of 1.0 atmosphere, using a TSI Model 1279 probe. This probe is a cylindrical, single wire, cross-flow probe. The support structure has a diameter of 0.035 inches, which was the

smallest structure available. The probe was inserted through the side of the tunnel, with a positional uncertainty of 0.5 mm. Low-pressure readings could not be taken due to leakage problems. Figure 3.21 shows the measured velocity profiles.

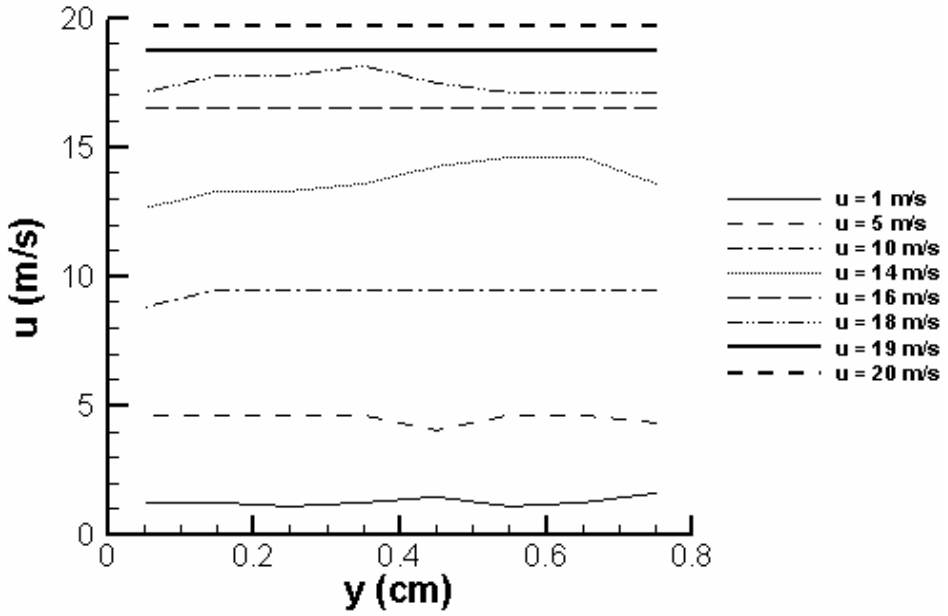

Figure 3.21. Measured Velocity Profiles 1 cm into Test Section

Direct comparison of these results with the computational fluid dynamics results is not feasible, due to the lack of detailed information in the boundary layer. These results show that a uniform velocity profile is maintained across the test section, suggesting that the tunnel fulfils the design criteria.

The streamwise velocity fluctuations u'_{rms} are also measured by taking the root-mean squared fluctuations in the hot-wire voltage, and are shown in Figure 3.22 below:

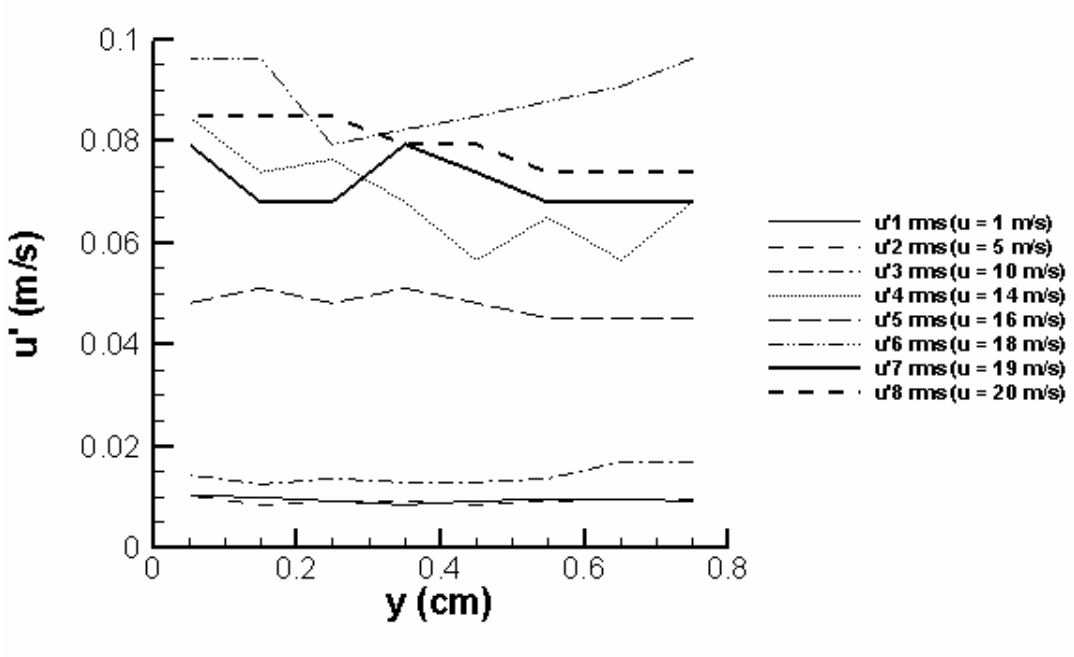

Figure 3.22. Measured Turbulent Fluctuations 1 cm into Test Section

Figure 3.23 shows the percentage turbulence intensity, normalized using the local average velocity. All results for local turbulence intensities are below 1%.

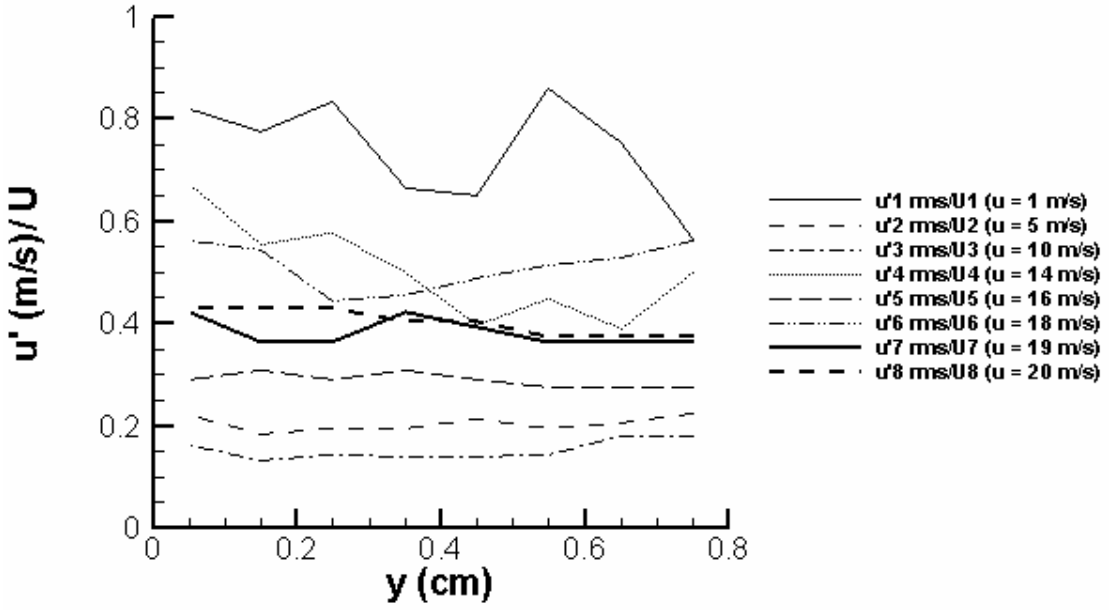

Figure 3.23. Normalized Turbulent Fluctuations 1 cm into Test Section

The hot-wire used in these experiments was calibrated at a pressure of 1.0 atm in a low-speed wind tunnel, and then used for low-pressure testing. Because of this, the absolute velocity measurements may not be valid. However, the results do show that the tunnel has uniform flow, and turbulence intensity on the order of one percent.

3.7. Final Tunnel Testing

After the initial results showed uniform flow, the tunnel was modified by the addition of a bypass valve, improved sealing, and additional instrumentation. Final tests were performed to characterize the system.

3.7.1. Final Tunnel Configuration

The completed facility is shown as figure 3.24:

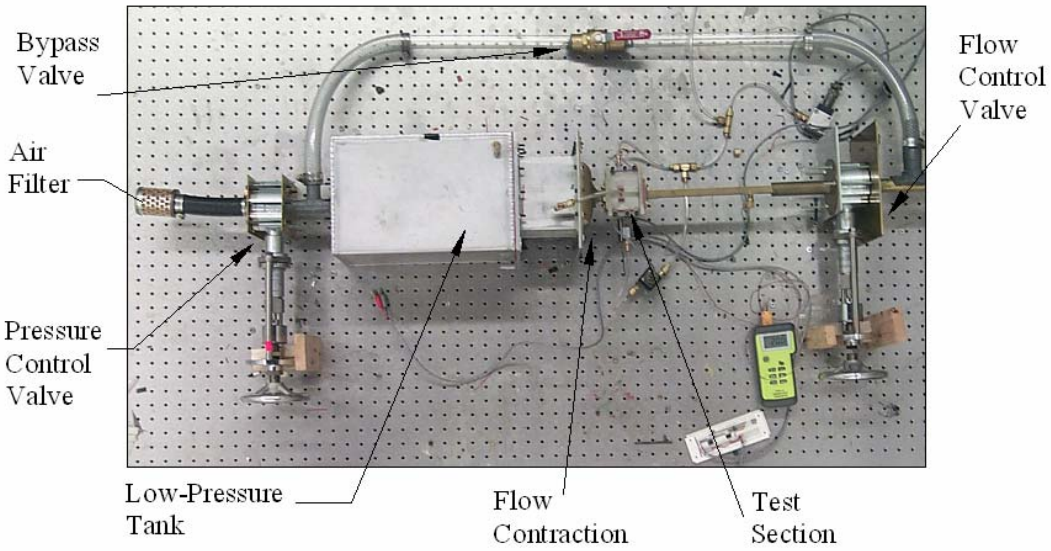

Figure 3.24. Operational Facility

The flow direction of the tunnel in this photograph is from left to right. The main difference between this layout and the one used for preliminary testing is the addition of a bypass system. A second 2.5 cm diameter flow line is installed in parallel to the test

section to serve as a bypass. This allows low pressure to be maintained in the settling chamber even when there is very little airflow through the vacuum system.

3.7.2. Test Section Instrumentation

The instrumented test section is shown in figure 3.25:

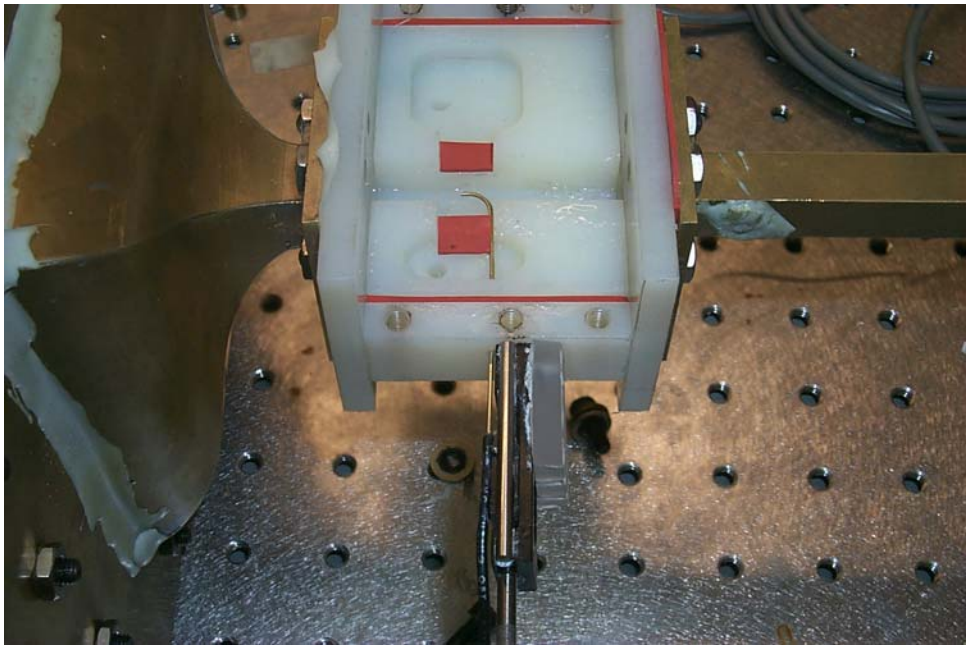

Figure 3.25. Test Section Instrumentation

An impact probe to measure dynamic pressure, a static pressure port, and a thermocouple are installed in the test section. The 0.0008 m diameter impact probe is moved across the test section by using the attached vertical stage. A schematic of this apparatus is shown as figure 3.26:

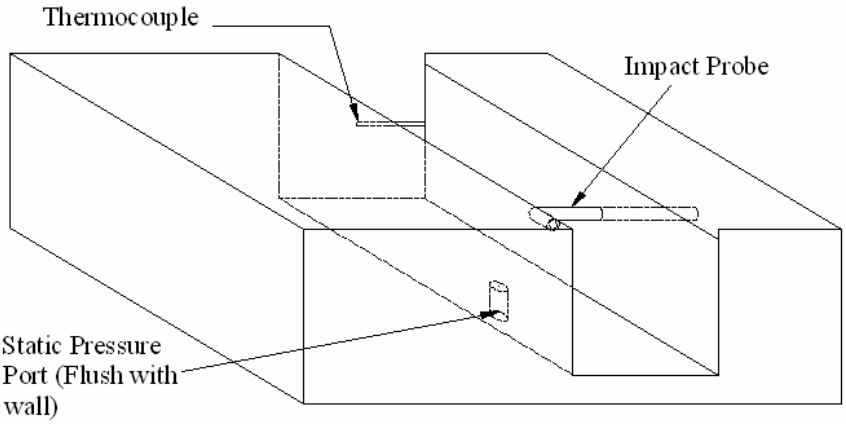

Figure 3.26. Test Section Instrumentation

A schematic of the test-section instrumentation, including manometers used for calibration, is shown as Figure 3.27:

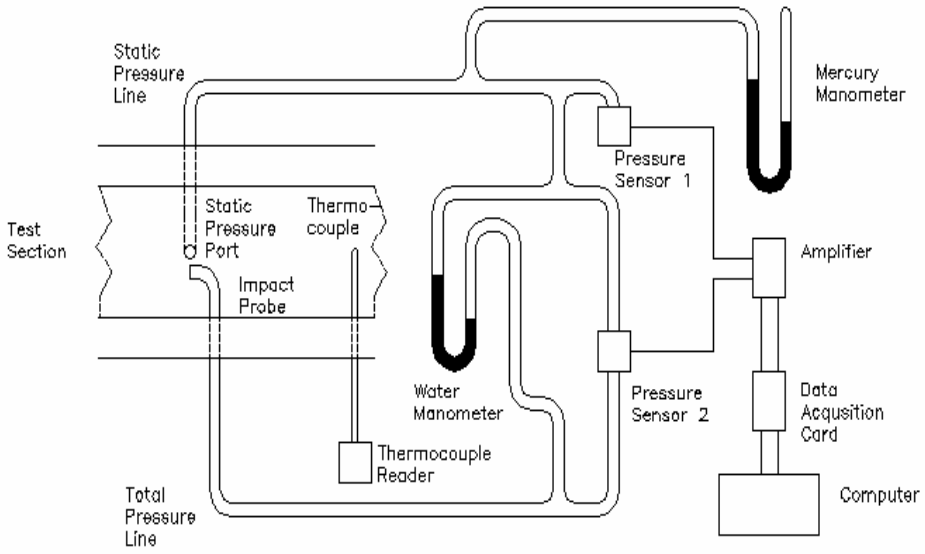

Figure 3.27. Test Section Instrumentation Schematic

The impact probe allows direct measurement of velocity based on the Bernoulli principle and the ideal gas law (Holman, 2000), as given in equation (3.12):

$$u = \sqrt{\frac{2(\Delta P)}{\rho}} = \sqrt{\frac{2RT(\Delta P)}{P}} \tag{3.12}$$

where P is the static pressure, T is the static temperature, R is the ideal gas constant, and ΔP is the dynamic pressure of the system, which is the difference between the pressure at the probe and the static pressure.

3.7.3. Test Section Velocity Measurements

The velocity profiles in the test section are measured for pressures ranging from 0.3 to 1.0 atmosphere, and are shown as figures 3.28 through 3.31. Due to geometric constraints on the impact probe, the velocity is measured from one wall to past the mid-point of the test section, instead of across the entire test section. The error bars for velocity were generated using the experimental uncertainty in the measurements of pressure and temperature, and applying them to equation (3.12) using the normal experimental uncertainty equations. (Holmann, 1984)

$$\varepsilon(u) = u\sqrt{\left(\frac{1}{2}\frac{\varepsilon(T)}{T}\right)^2 + \left(\frac{1}{2}\frac{\varepsilon(\Delta P)}{P}\right)^2 + \left(\frac{1}{2}\frac{\varepsilon(P)}{P}\right)^2} \tag{3.13}$$

ε(u) is the experimental uncertainty in the velocity, ε(T) is the experimental uncertainty in the temperature, ε(ΔP) is the experimental uncertainty in the dynamic pressure, and ε(P) is the experimental uncertainty in the static pressure.

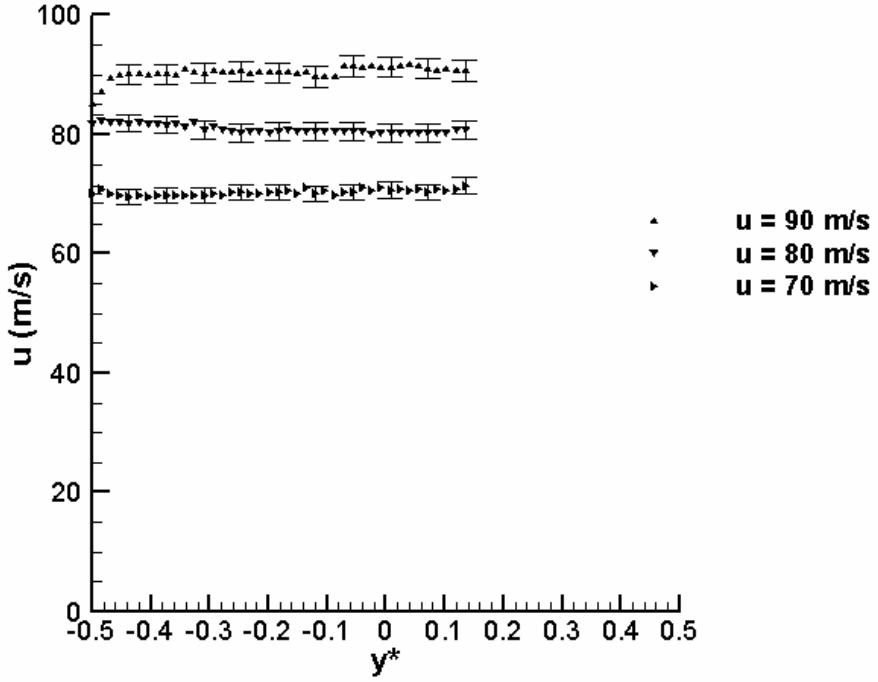

Figure 3.28. Velocity Profiles for P = 0.3 atm

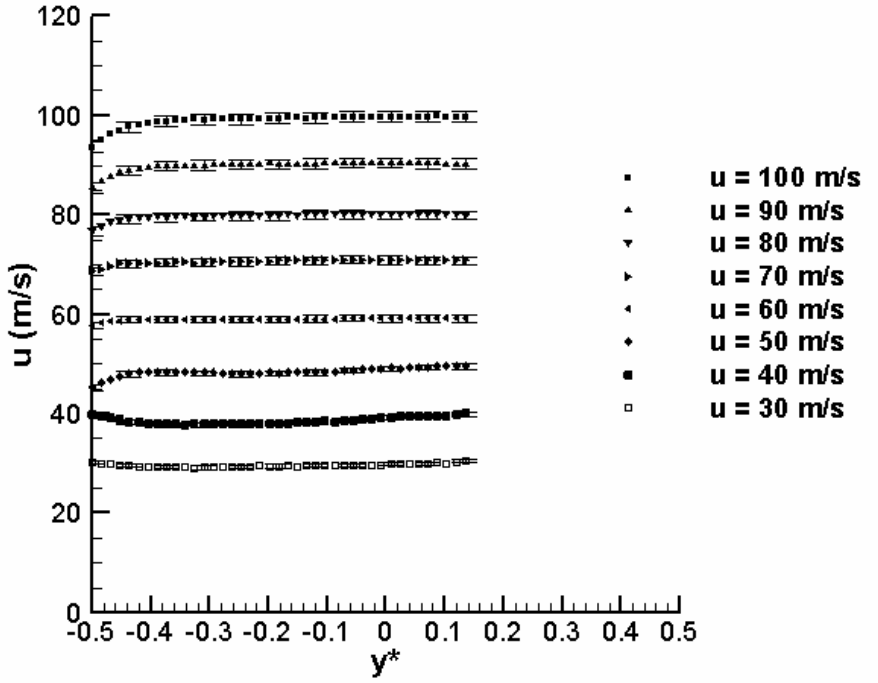

Figure 3.29. Velocity Profiles for P = 0.5 atm

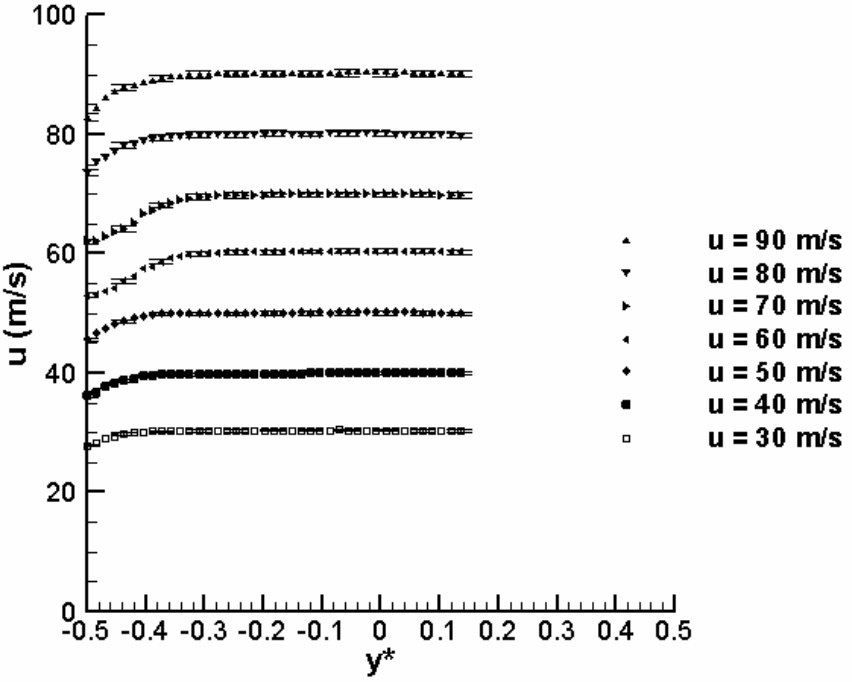

Figure 3.30. Velocity Profiles for P = 0.9 atm

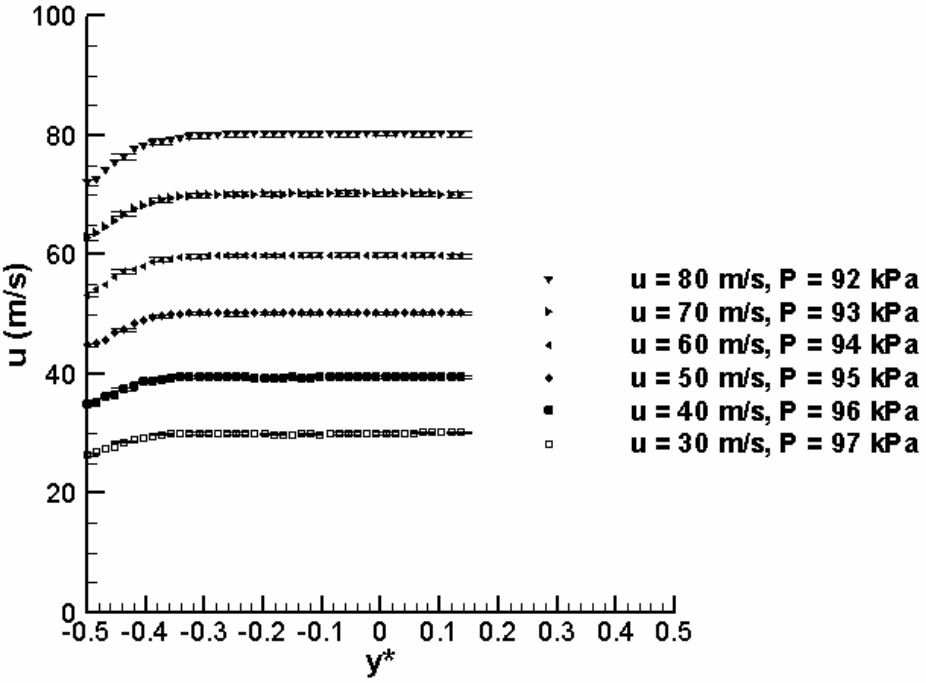

Figure 3.31. Velocity Profiles for P = 1.0 atm

These results show a core of uniform flow, as predicted by the CFD modeling. They also show possible transition to turbulence in the boundary layer at high Reynolds numbers, as predicted by the modeling of the boundary layer. Therefore, independent measurements were taken of turbulence in the core of the flow, to ensure that the channel flow remains laminar.

The flows measured do not cover the entire design range of the tunnel. While the tunnel could be run at pressures of 0.15 atm, reliable flow measurements could not be obtained in that range. This is a limitation of the total pressure probes used in the testing. The tunnel design could only be validated for the range of pressures between 0.3 and 1.0 atmosphere.

3.7.4. Test Section Turbulence Measurements

The turbulence at the centerline of the test section is characterized using a TSI hot-film probe, as shown in figure 3.32. The re-designed test section allows simultaneous use of a hot-film probe and an impact probe, avoiding the calibration problems present in preliminary tests. The hot-film probe is mounted in the same y-z plane as the impact probe, avoiding flow interference.

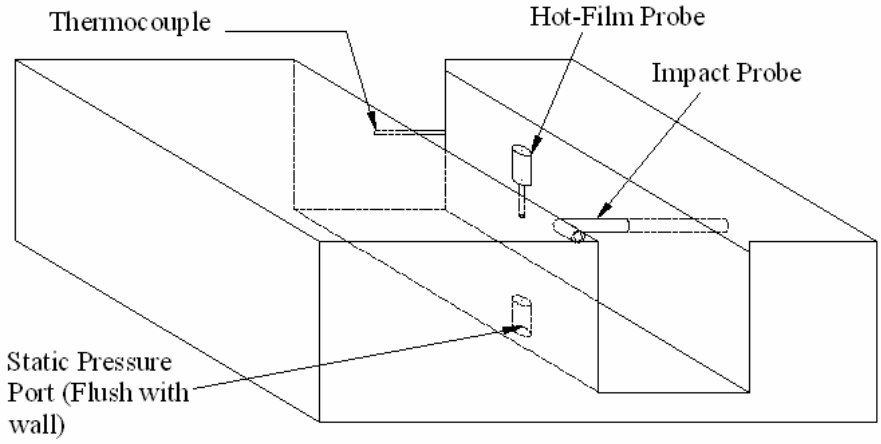

Figure 3.32. Test Section Instrumentation with Hot Film Probe

The probe is then calibrated by comparison with the impact probe. This method of calibration is selected since external calibration would not be reliable at lower pressures. Testing shows that the commercial hot-wire system is not reliable for low pressures, so measurements of turbulence intensity are taken at 0.6 atmospheres and 100 m/s, and 0.9 atmospheres and 90 m/s. Because the probe is an intrusive measurement, and may generate additional turbulence, the turbulence numbers given by the hot-wire should be taken as an upper bound on the turbulence in the tunnel. Typical hot-wire traces are shown in figure 3.33:

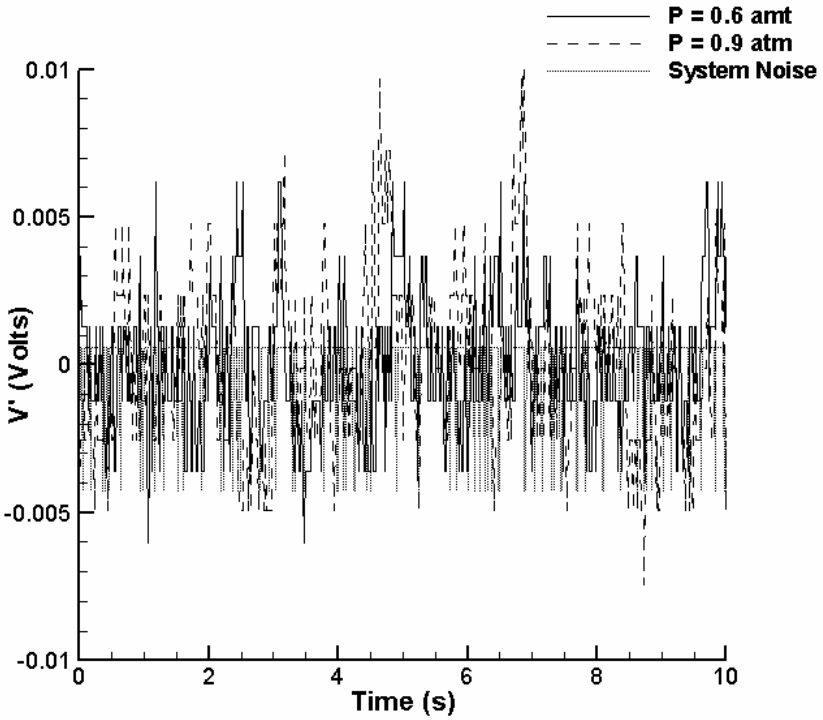

Figure 3.33. Centerline Hot-Wire Voltage Fluctuations

These results show that the flow is steady over the duration of planned tests. The voltage fluctuations due to turbulence in the hot-wire system are low enough to be on the same order of magnitude as the electrical noise in the system. Because sources of error

accumulate as vector sums, the electrical noise can be removed from the rms calculations using the following equation: (Holmann and Moody, 1994)

$$V(turb)'_{rms} = \sqrt{\overline{V'^2} - V(noise)'^2_{rms}} \tag{3.14}$$

where $V(turb)'_{rms}$ is the voltage fluctuation due to turbulence, V' is the voltage fluctuation in the signal, and $V(noise)'_{rms}$ is the measured signal noise. After removal of signal noise, the measured turbulence intensity is 0.2 % for 0.6 atmospheres and 100 m/s, and 0.4 % for 0.9 atmospheres and 90 m/s. Due to the intrusive nature of the probe in a confined channel, these should be taken as upper limits on the turbulence values.

3.8. Conclusions

Computational fluid dynamics analysis showed that high contraction-ratios are possible for wind-tunnel usage without incurring flow separation, or corner vortices. These results were confirmed by experimental measurements that show that uniform flow profiles were achieved with minimal turbulence. Boundary layer growth is minimal, and a core of uniform flow was maintained. Additional study may be undertaken to determine the limits of 100-1 contractions as a flow control tool.

Experimental study showed that the design goals of the test facility were partially met. The full range of desired pressures and velocities could not be achieved. However, the results suggest that any future low-pressure wind-tunnel built on a draw-through design should be designed with a high bypass ratio to the test section. This will improve the flexibility of the design for testing at low speed, low-pressure conditions.

CHAPTER 4

DESIGN OF AN INTEGRATED MICRODEVICE WITH AN AIRFOIL AND FORCE SENSOR

4.1. Introduction

To allow measurement of aerodynamic forces on micromachined beams in the slip flow regime, an integrated microdevice, including a flat-plate airfoil and a piezoresistive force sensor, is designed and fabricated. The structural limitations on a beam with a micro-scale cross-section, and meso-scale length, are analyzed and used to set a maximum airfoil width. A fabrication process for beams with these dimensions is created, and validated, allowing selection of a maximum allowable beam width. The integrated piezoresistive force sensor is designed and analyzed, based on the expected aerodynamic forces and the maximum allowable beam width.

4.2. Sensor Configuration

Previous researchers have measured forces on a beam system using piezoresistive methods, usually to measure a one-dimensional force or acceleration. (Madou, 1997) To allow simultaneous measurement of lift and drag, the concept has been extended to two dimensions by using an asymmetric mounting. The design, which integrates the force sensor with the flat plate airfoil, is shown in figure 4.1 below:

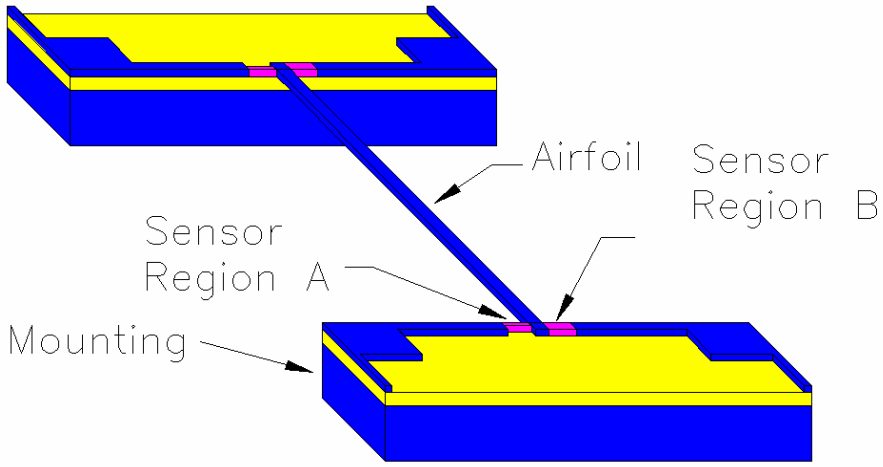

Figure 4.1. Integrated Flat Plate Airfoil and Sensor Design

The device can be fabricated from a silicon-on-insulator wafer. The structure consists of the airfoil, and four sensor regions, which transmit forces to the substrate.

4.3. Fabrication and Release of Long Beam Structures

4.3.1. Structural Constraints

The maximum allowable design width of the beam used in testing is set by the expected force during testing. However, three sets of structural limitations affect the allowable length of a micro-fabricated beam structure: buckling during release, structural loading in liquid flow around the beam during release, and possible low natural frequencies for the resulting beam structure. Another concern is the possibility of stiction during the release, which may also cause breakage of microbeams.

4.3.1.1. Aerodynamic Drag

Structural considerations limit the maximum chord of any micro-scale airfoil, and the width of the facility. The maximum allowable span of the airfoil is found by modeling the system as a beam under uniform loading (Ugural, 1995). In this case, the maximum stress seen in the airfoil will be at the end of the airfoil:

$$\sigma_{max} = \frac{3 S f}{2 c^3 t} \tag{4.1}$$

where σ_{max} is the maximum stress, S is the span of the beam, c is the chord, t is the thickness, and f is the force per unit span.

For crystalline silicon, the yield strength is approximately 8.4 GPa. (Peterson, 1982) Crystalline silicon typically does not deform at its yield strength- it will shatter. Using a safety factor of 1.5, the maximum allowable force for 40 and 100 micron chord airfoils as a function of thickness and span is shown in figures 4.2 and 4.3:

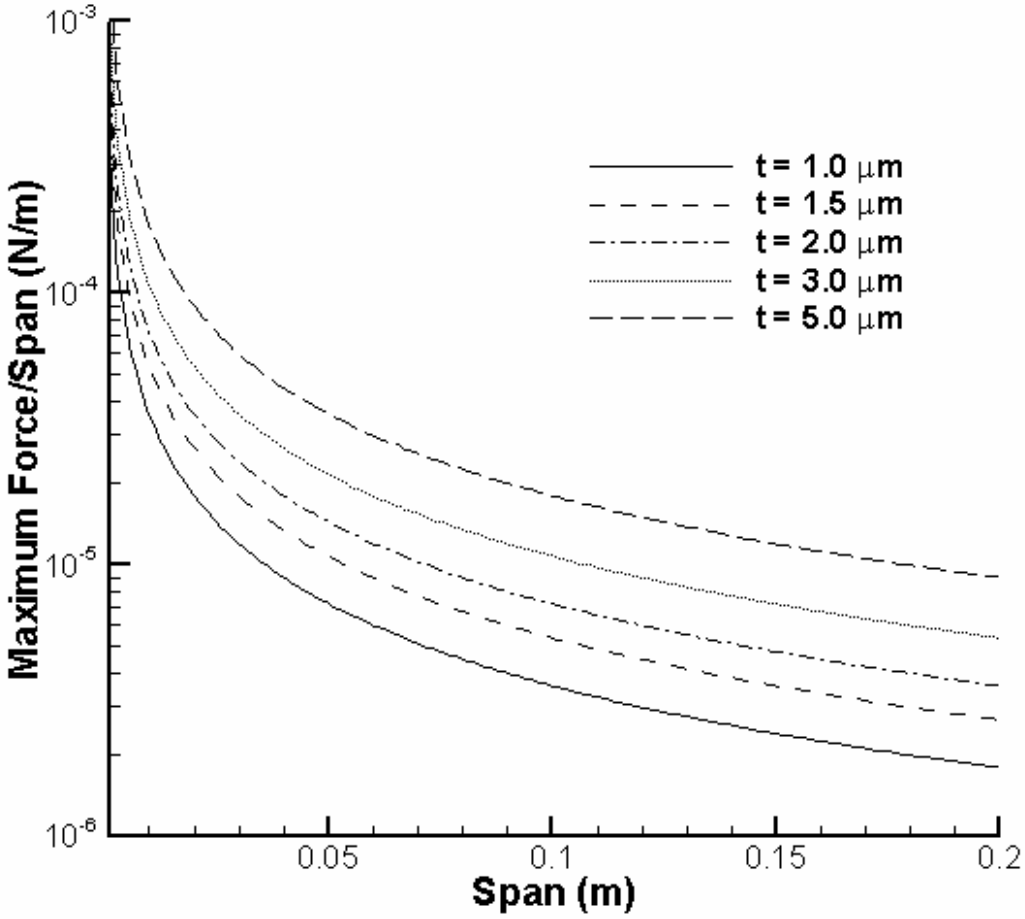

Figure 4.2. Allowable Force/Span vs. Span for 40 micron Airfoil

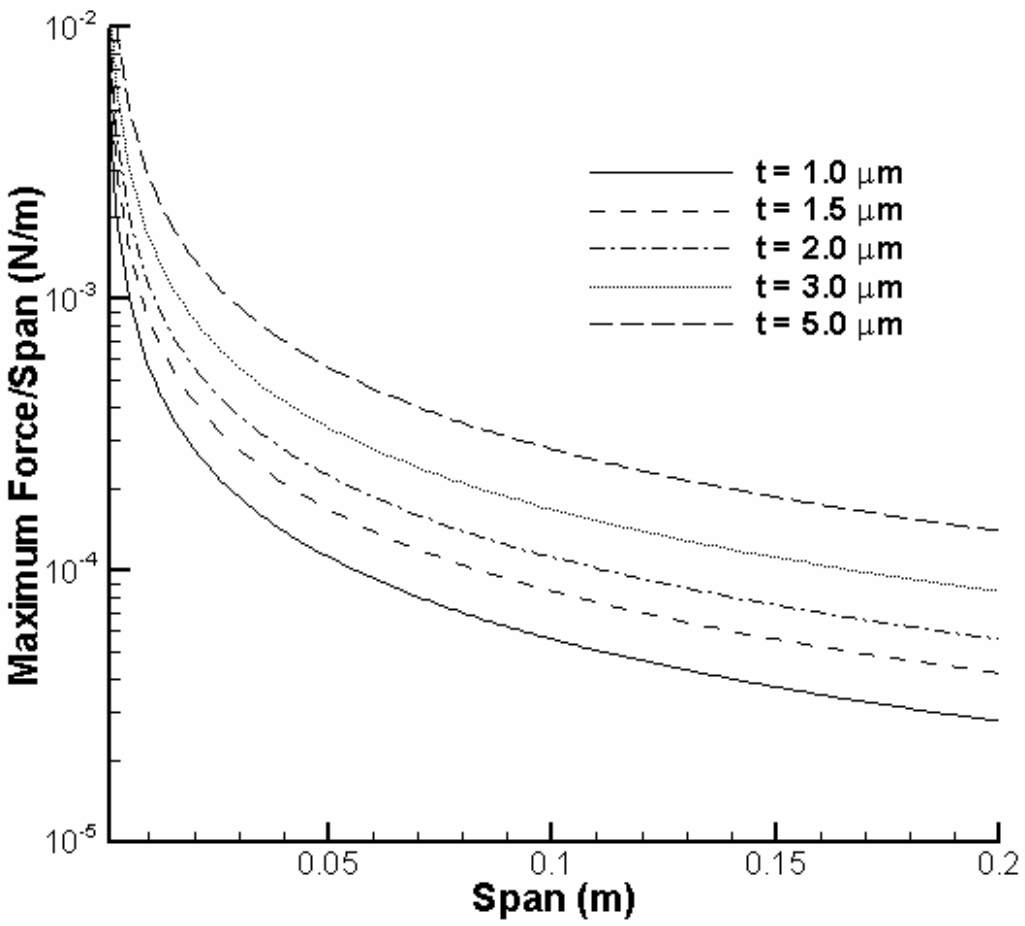

Figure 4.3. Allowable Force/Span vs. Span for 100 micron Airfoil

These results can be compared to the aerodynamic forces for 40 and 100 micron airfoils shown as figures 2.15 and 2.16. Comparing the maximum allowable forces in figures 4.2 and 4.3 to the expected aerodynamic forces allows selection of a maximum allowable span for airfoil testing. Based on these concerns, a span of 1 cm was selected for airfoil testing.

Based on the selected span of 1 cm, a more complete analysis of the stresses in the airfoil was performed for a 5 micron thick airfoil structure. The shear on a uniformly loaded beam anchored at both ends is given as:

$$V = \frac{S\ f}{2}\left(1 - 2\frac{z}{S}\right) \tag{4.2}$$

where z is the position along the beam. The shear as a function of position is calculated for 40 and 100 micron beams, assuming the maximum aerodynamic loading shown in figures 2.15 and 2.16, and a span of 1 cm. The results are shown as figure 4.4:

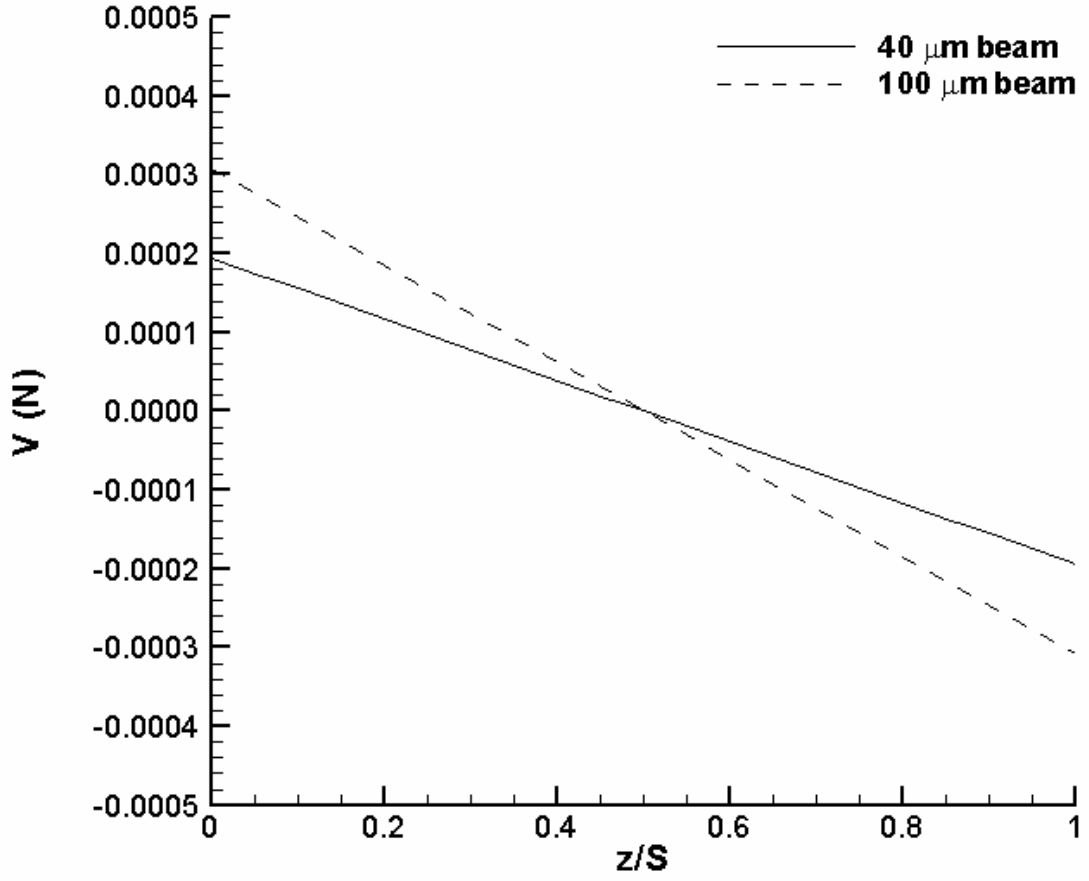

Figure 4.4. Airfoil Shear versus Location

The bending moment can be found by integration equation 4.2:

$$M = \frac{S\ f}{2}\left(z - \frac{z^2}{S}\right) \tag{4.3}$$

The bending moment for 40 and 100 micron beams is shown as figure 4.5:

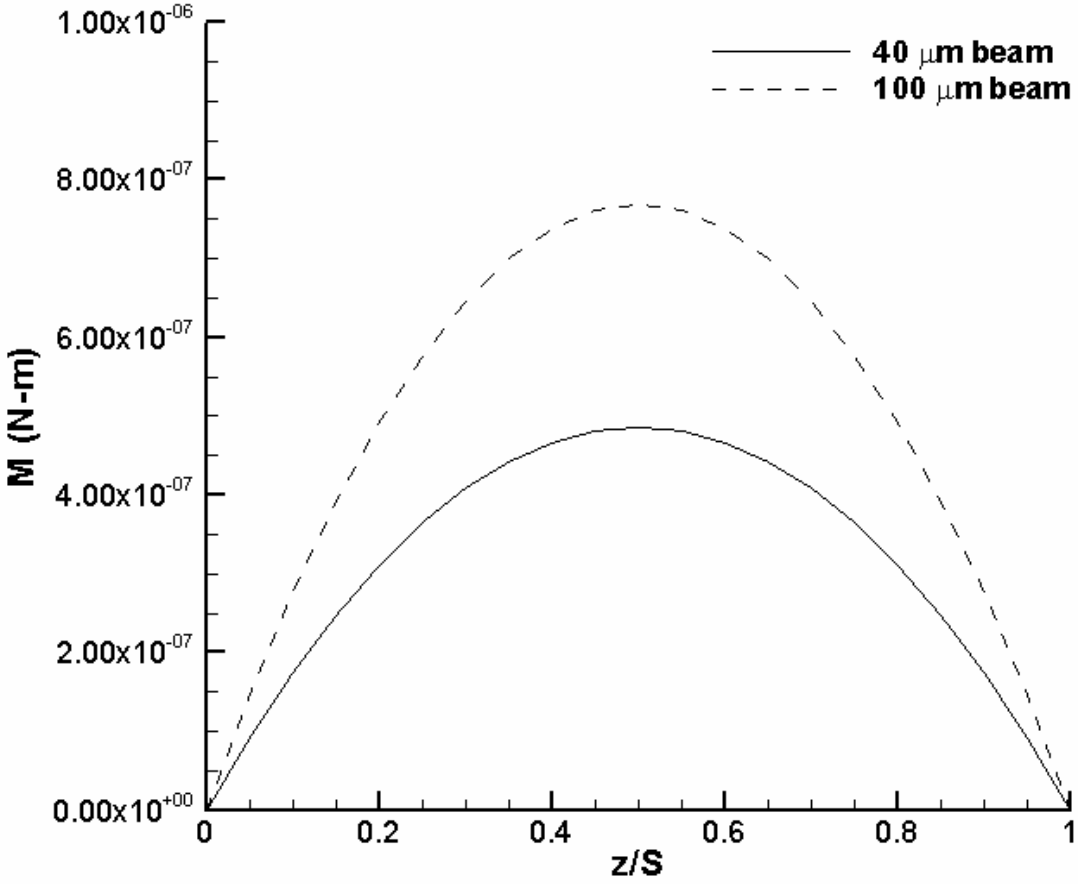

Figure 4.5. Airfoil Bending Moment versus location

These results can be used to calculate the maximum shear and compressive stresses in the beams. The maximum shear stress in the beam cross-section will occur at the beam center-line, and is given by the expression

$$\tau_{\max} = \frac{3\mathrm{V}}{2\mathrm{A}} = \frac{3V}{2tc} \tag{4.4}$$

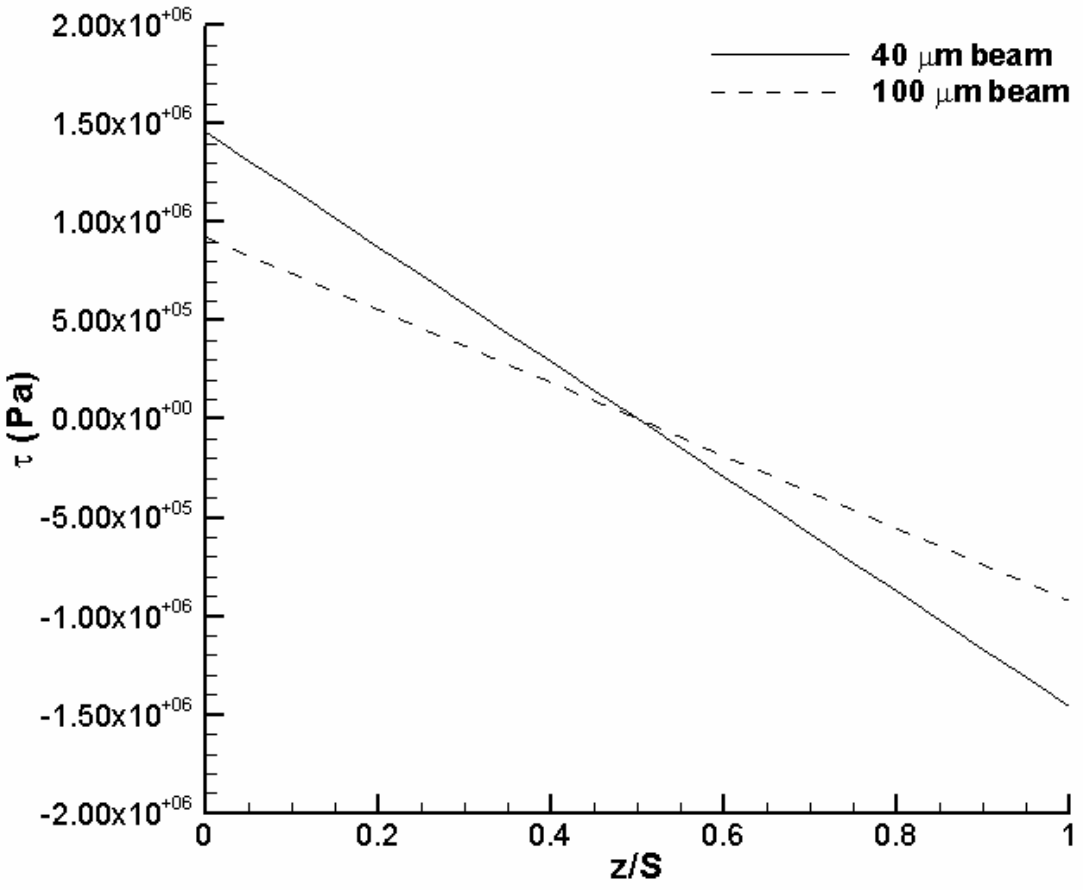

Figure 4.6. Maximum Shear Stress versus Location

The maximum compressive stress will occur at the edge of the beam cross-section, and is given by:

$$\sigma_{\max} = \frac{\mathrm{M}}{\mathrm{I}}(\mathrm{c}/2) = \frac{6M}{tc^2} \tag{4.5}$$

This result is shown in figure 4.7:

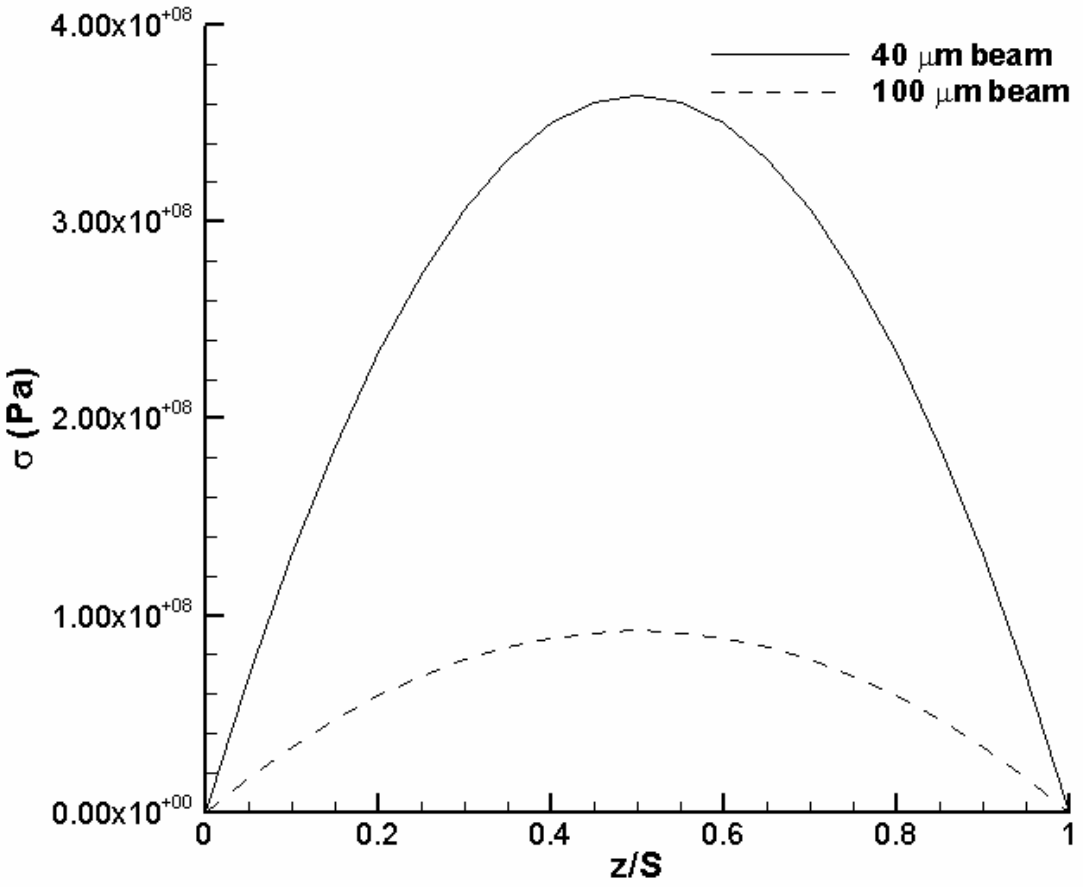

Figure 4.7. Maximum Compressive Stress versus Location

In all of these cases, the maximum stresses calculated are well below the yield strength of silicon.

4.3.1.2.Viscous Drag During Beam Release

A similar analysis can be carried out to obtain the maximum allowable force on the beams during release. As the beam is pulled away from support structure during release, the flow around the beam will create force on the beam. The flow geometry is shown in figure 4.8:

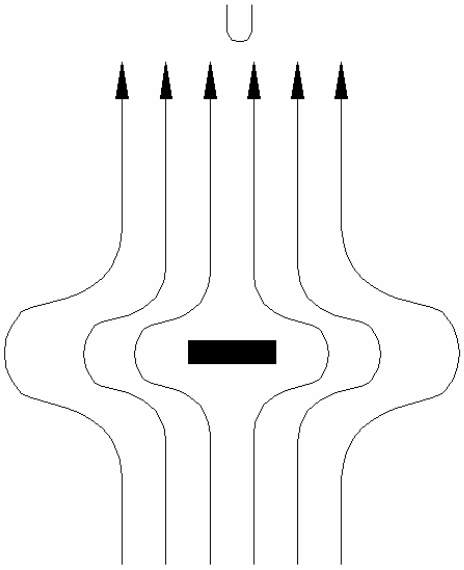

Figure 4.8. Flow Around the Beam During Release

Low-Reynolds Number fluid flow theory (White, 1991) suggests that the force on the beam per unit span will be a function of the beam width, the fluid velocity, and the fluid viscosity:

$$\frac{F_D}{S} \propto U\mu c \tag{4.6}$$

To calculate the expected fluid forces, a commercial computational fluid dynamics package was used (Fluent, 1995). The expected forces were calculated for a beam with a chord of 100 μm and a thickness of 5 μm for velocities ranging from 0.1 to 2.0 mm/s. Density and viscosity values for acetone and pentane were used (CRC, 2001). Acetone is the usual release fluid to remove photoresist, but recent researchers have had success with fragile structures using pentane. (Raccurt, 2004) The results are shown in figure 4.9:

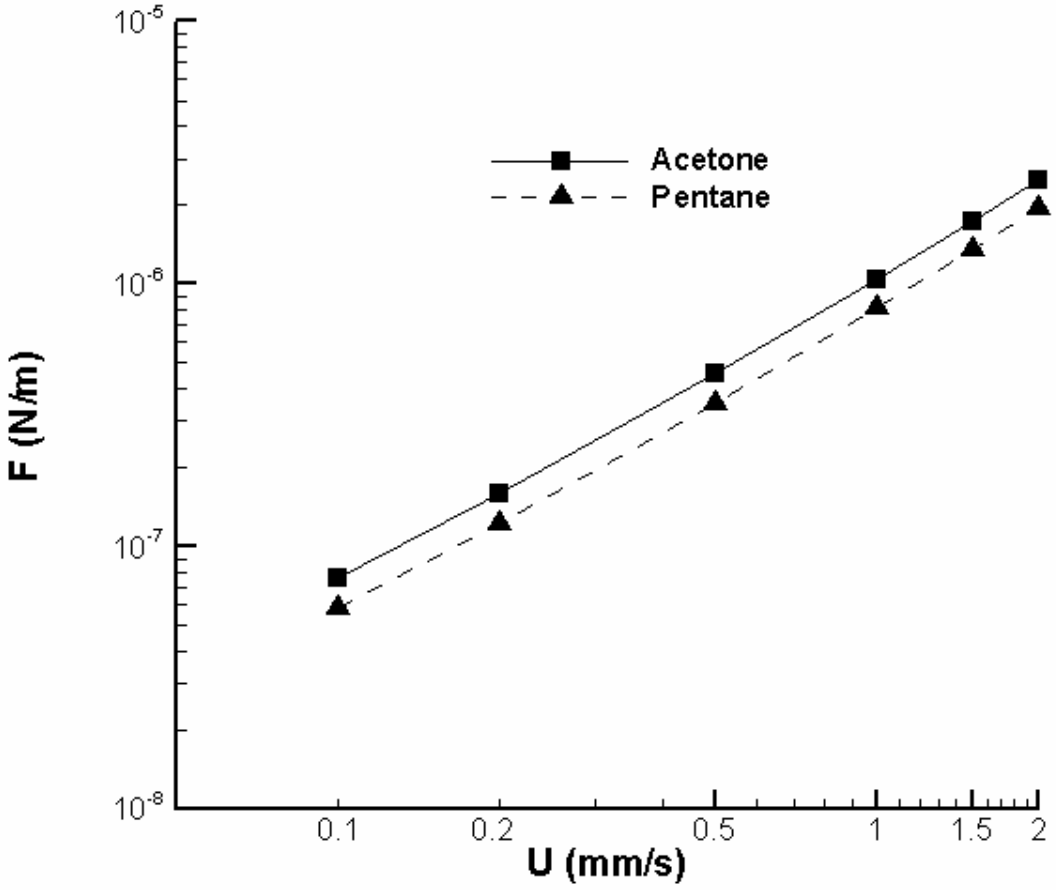

Figure 4.9. Expected Viscous Forces During Release

The allowable structural loads on the beam can be found by modeling the system as a beam under uniform loading (Ugural, 1995). In this case, the maximum stress seen in the airfoil will be at the end of the plate:

$$\sigma_{max} = \frac{3 S f}{2 t^3 c} \tag{4.7}$$

where σ_{max} is the maximum stress, S is the span of the beam, c is the chord, t is the thickness, and f is the force per unit span.

Using a factor of safety of 1.5, and the mechanical properties of crystalline silicon (Peterson, 1982), the maximum allowable force during release on a beam with a chord of

100 μm is shown in figure 4.10:

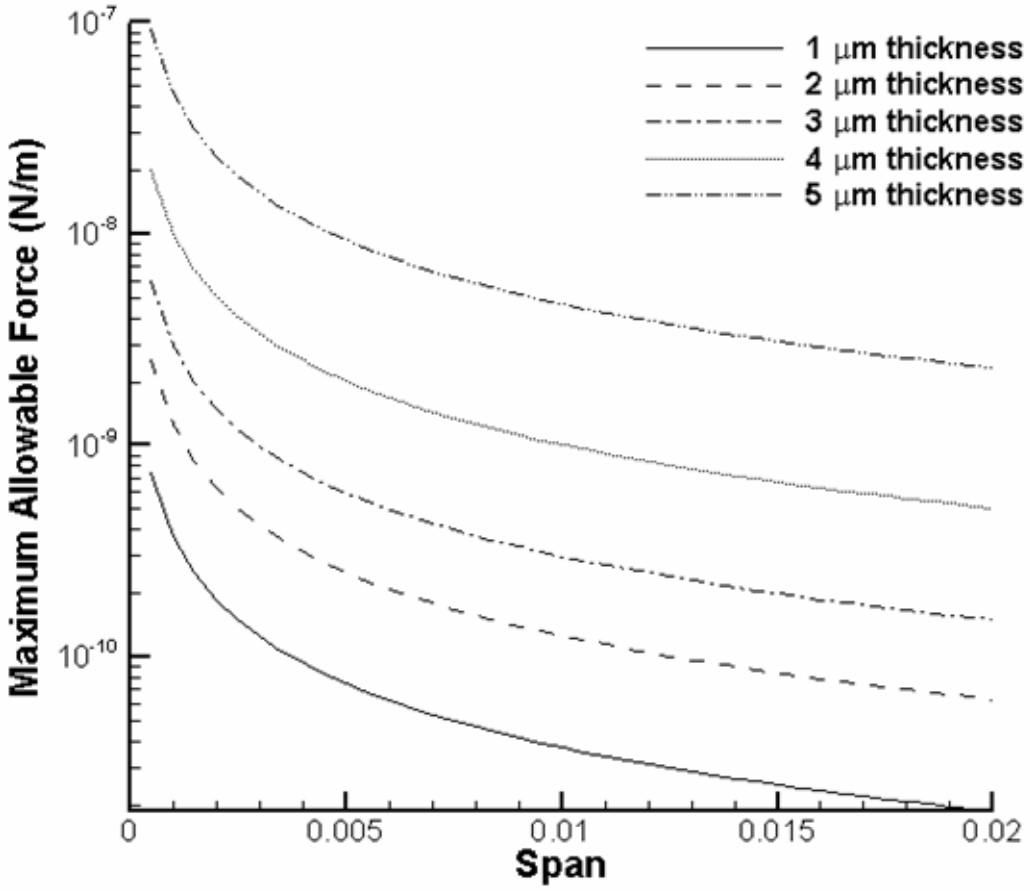

Figure 4.10. Maximum Allowable Force During Release

Comparison of figure 4.9 with figure 4.10 shows that, by using a low-viscosity fluid such as pentane, and a wet release process that minimizes fluid motion, it is possible to successfully release silicon beam structures with a chord of 100 μm, a thickness of 5 μm, and a span of 1 cm.

4.3.1.3. Vibration

The first natural frequency of the first vibrational mode of a structure clamped at both ends is given by equation (4.8) (Timoshenko, 1974):

$$\omega = \frac{4.73^2}{S^2} t \sqrt{\frac{E}{12\rho_{beam}}} \tag{4.8}$$

where ω is the natural frequency, E is the elastic modulus, and ρ_{beam} is the density of the beam. Using the properties of crystalline silicone, figure 4.11 shows the natural frequency of a micro-machined silicon beam as a function of thickness and span:

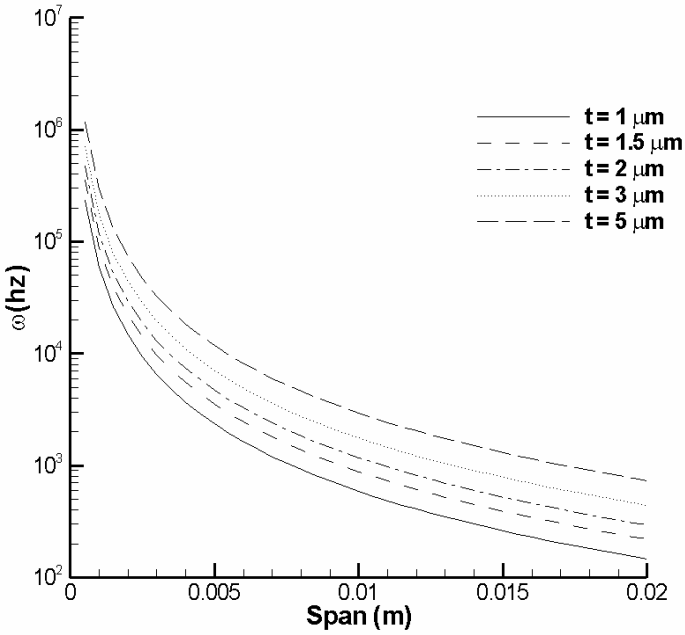

Figure 4.11. Natural Frequency for a Silicon Beam as a function of span and thickness

These results suggest that as the beam thickness approaches 1 micron, even low frequency vibrations within the laboratory environment may excite the beam.

4.3.1.4. Beam Buckling

Buckling during release is encountered in a variety of MEMS applications (Fang, 1999, White, 2003). Buckling in microstructures typically results from thermal stresses in the materials, usually as a result of deposition at high temperatures. The critical stress required to buckle a microbeam is given by the expression:

$$\sigma_{crit} = \frac{4\pi^2 EI}{S^2 A} = \frac{\pi^2 Et^2}{3S^2} \tag{4.9}$$

where I is the moment of inertia of the beam cross-section, and A is the beam cross-sectional area (Fang, 1999). The critical stress for a silicon microbeam as a function of thickness and length is given as figure 4.12:

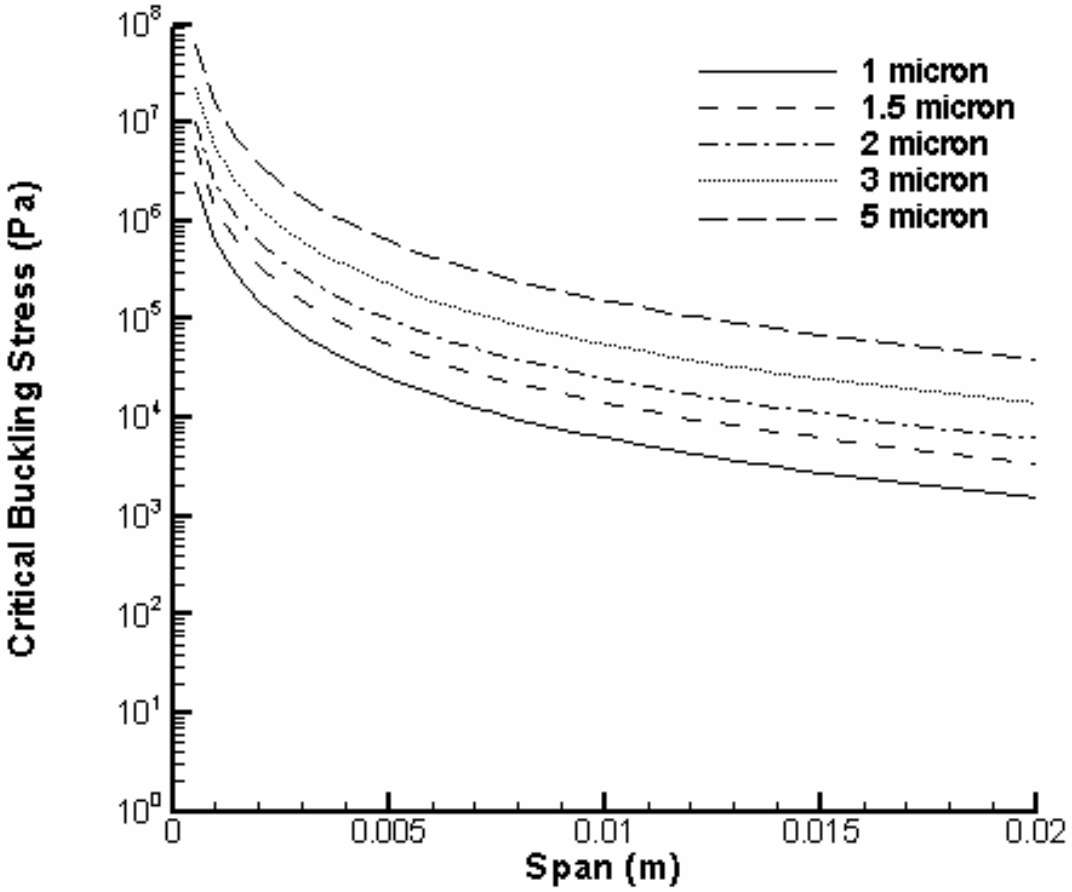

Figure 4.12. Critical Buckling Stress for a Silicon Beam as a function of span and thickness

Build-up of thermal stress can be avoided by careful selection of wafer materials. Silicon-on-Insulator wafers using mechanically attached layers will have lower thermal stresses than wafers using oxide deposited at high temperatures, and should be used for this process.

All of these results suggest that for a micro-machined structure with a length on the order of mm or cm, the practical limit for thickness is on the order of 1 micron.

4.3.2. Fabrication of Meso- Scale Beam Structures with Micro-Scale Cross Section

The fabrication process for a polysilicon micro-beam is shown in figure 4.13.

Step 1. The process begins from a bare silicon wafer

Step 2. A 1.0 micron thick layer of silicon oxide is deposited using a Low-Pressure Chemical Vapor Deposition (LPCVD) process.

Step 3. A 2.0 micron thick layer of polysilicon is deposited using a LPCVD process.

Step 4. A 4 to 8 micron thick masking layer of silicon oxide is deposited on the backside of the wafer using a LPCVD process.

Step 5. The top of the wafer is coated with SC1827 photoresist, and the beam structure is defined using photolithography. The beam structure is then defined in the polysilicon using a Reactive Ion Etch (RIE) process. The oxide layer forms an etch stop for this process. The photoresist is then removed.

Step 6. SC1827 photoresist is deposited on the backside of the wafer, and the mounting shape is defined using photolithography. The oxide is etched using a 1:1 solution of buffered hydrofluoric (HF) acid. The photoresist is removed.

Step 7. The first handling wafer, with pre-etched micro-channels, is attached to the device layer using hard-baked AZ9260 photoresist.

Step 8. The first handle wafer is coated with AZ9260 photoresist. The shape of individual protective dies is defined using photolithography. The handle wafer is then divided into individual protective dies using a Deep Reactive Ion Etch (DRIE) to perform a through-wafer etch. The photoresist used to bond the

wafers is used as an etch stop for this process.

Step 9. The second handling wafer, which has pre-etched support structures, is attached using hard-baked AZ9260 photoresist.

Step 10. After the assembly is completed, the backside is etched through using a Deep Reactive Ion Etch, using the oxide layer as an etch stop. The backside oxide is used as a masking layer, and the buried oxide layer used as an etch stop.

Step 11. The wafers are then soaked in a 1:1 solution of buffered hydrofluoric (HF) acid, removing the oxide from underneath the beam structures.

Step 12. The device dies, with individual protective plates from the first handle wafer, are removed mechanically from the second handle wafer, avoiding the need for mechanical dicing. This protects the beam structures for excessive vibration.

Step 13. The device is mounted to support structure.

The device is soaked in acetone to remove the support plate. The acetone is then replaced in the beaker first with a solution of isopropanol, and then pentane, and the fluid removed. Soaking the devices in acetone will break down the photoresist used to attach the protective plates, allowing the beam structure to be released. Performing the final release with pentane reduces the surface tension forces during release, allowing for the release of fragile structures (Raccurt, et al, 2004.) Using the backside oxide mask, instead of photoresist, means that there is no residual oxide left on the backside of the wafer, meaning that the mounting will not be affected by acetone.

Step 1. Bare Silicon Wafer

Step 2. Buried Oxide Deposition

Step 3. Polysilicon Deposition

Step 4. Backside Oxide Deposition

Step 5. Define Beam Geometry

Step 6. Define backside oxide mask

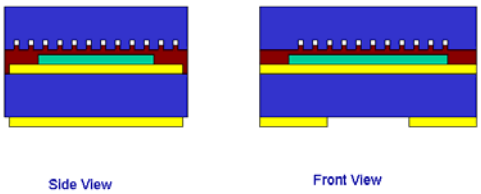

Step 7. Add first handling wafer

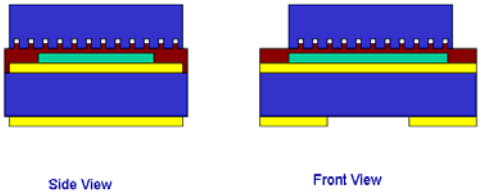

Step 8. Define first handling wafer geometry

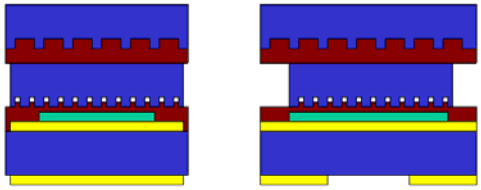

Step 9. Add second handling wafer

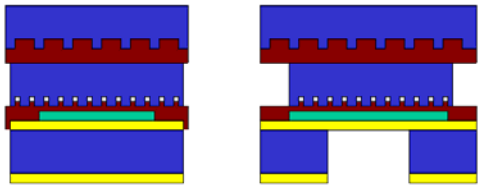

Step 10. Etch bulk silicon of device wafer

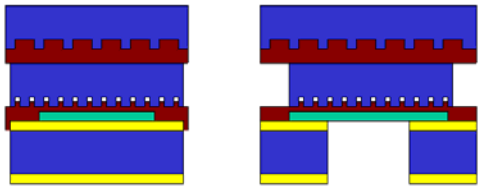

Step 11. Remove oxide from under airfoil

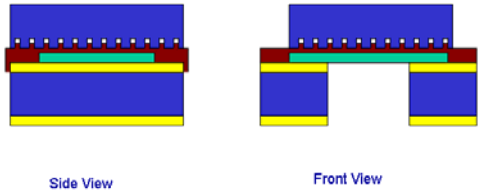

Step 12. Remove second handle wafer

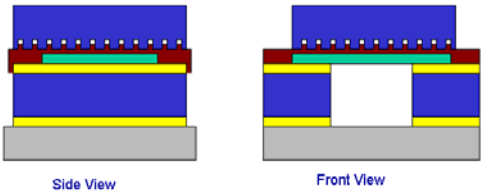

Step 13. Attach device to tunnel mounting

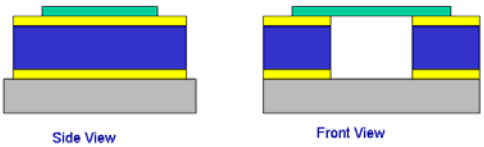

Step 14. Remove protective plate

Figure 4.13. Polysilicon Beam Fabrication Process

A released comb of structures, varying in length from 0.1 to 1.0 cm, is shown in figure 4.15. (The 0.9 cm beam structure is broken.) This result demonstrates that beam structures with meso-scale length, and micro-scale cross-section, can be fabricated using existing processes and materials.

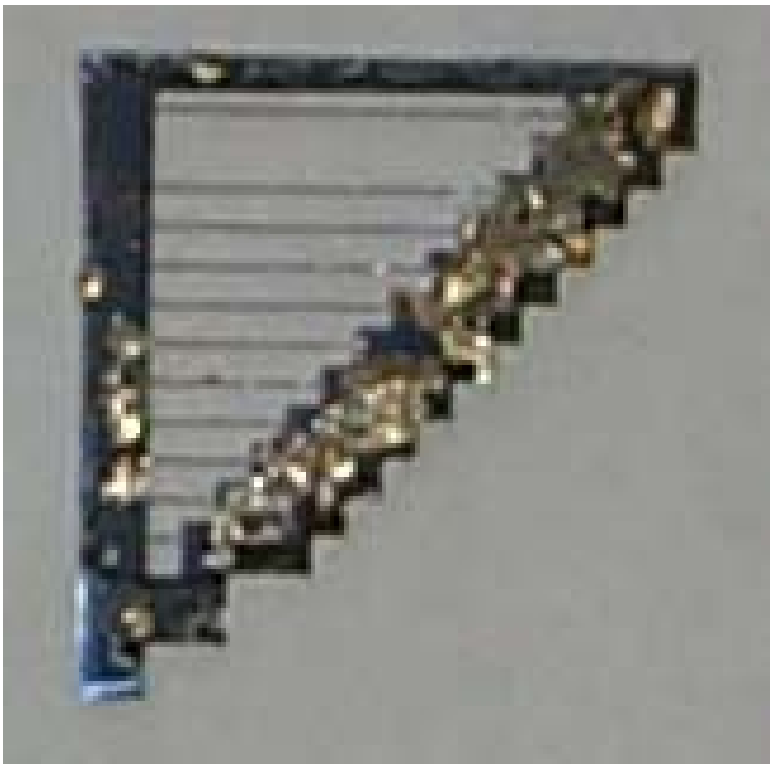

Figure 4.14. Released 1.5 μm thick Polysilicon Beam Structure

4.4. Sensor Design

4.4.1. Sensor Range

Based on the force per span estimates obtained in chapter 2, and on the maximum span of 1 cm found in section 4.1 of this chapter, we can estimate the expected forces on the airfoil using equation 4.10:

$$Force = 2.0\,\mathrm{L}\,\mathrm{C_D}\,\frac{c\rho U^2}{2} \tag{4.10}$$

where L is the airfoil span, C_D is the drag coefficient, c is the chord, ρ is the air density, and U is the velocity. As a conservative estimate, the no-slip drag coefficient given by (2.42) is used instead of a slip value. The estimated forces for a 40 micron and 100 micron airfoil with a span on 1 cm are shown as figures 4.16 and 4.17.

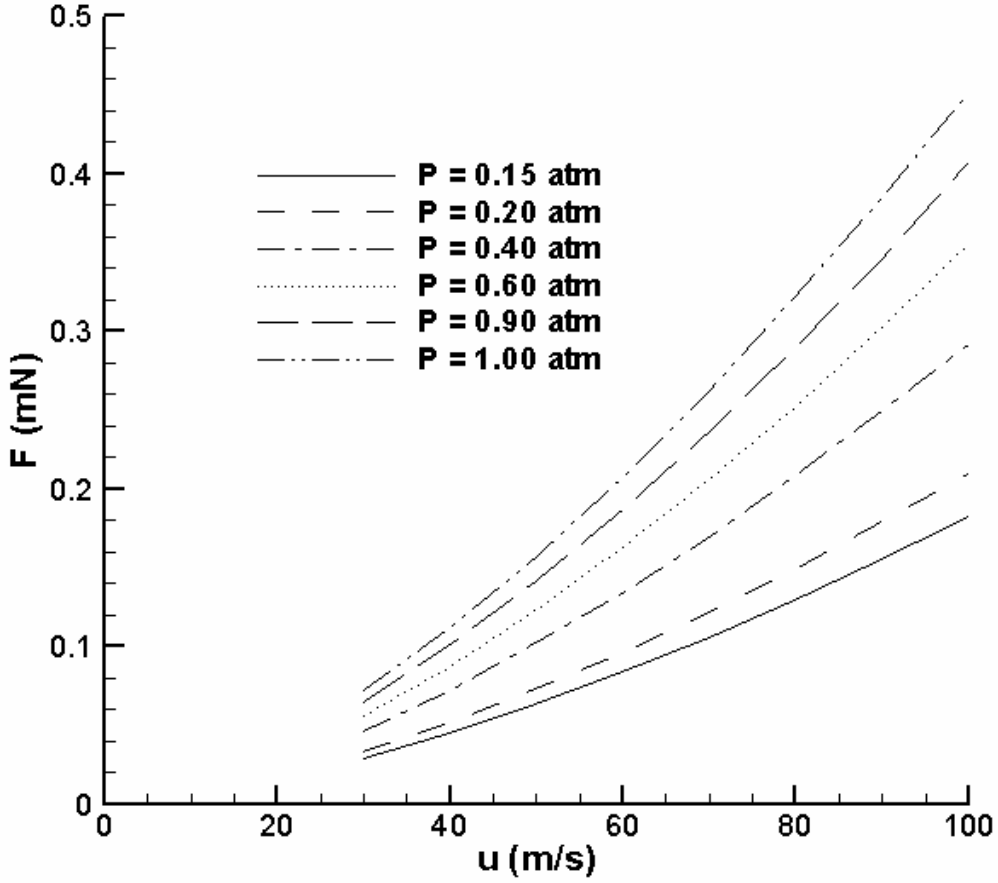

Figure 4.15. Estimated Forces on an Airfoil with a Chord of 40 μm, Span of 1 cm

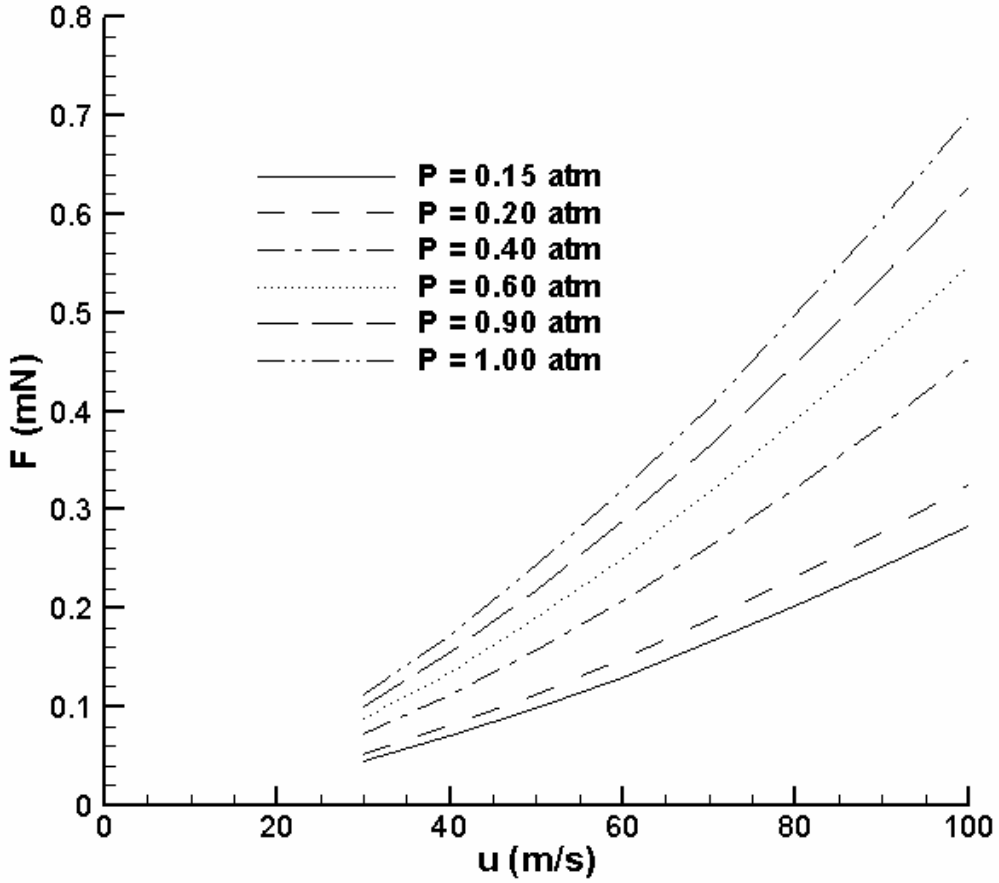

Figure 4.16. Estimated Forces on an Airfoil with a Chord of 100 μm, Span of 1 cm

4.4.2. Theory

The device uses piezoresistive effects to measure the stresses in the sensor regions. These measurements allow the forces on the airfoil to be determined. For a crystalline material, the change in resistivities is given by equation (4.11) (Sze, 1994)

$$\begin{bmatrix} \Delta\rho_x/\rho \\ \Delta\rho_y/\rho_y \\ \Delta\rho_z/\rho_z \\ \Delta\rho_{xy}/\rho_{xy} \\ \Delta\rho_{xz}/\rho_{xz} \\ \Delta\rho_{yz}/\rho_{yz} \end{bmatrix} = \begin{bmatrix} \pi_{11} & \pi_{12} & \pi_{13} & 0 & 0 & 0 \\ \pi_{12} & \pi_{11} & \pi_{12} & 0 & 0 & 0 \\ \pi_{13} & \pi_{12} & \pi_{11} & 0 & 0 & 0 \\ 0 & 0 & 0 & \pi_{44} & 0 & 0 \\ 0 & 0 & 0 & 0 & \pi_{44} & 0 \\ 0 & 0 & 0 & 0 & 0 & \pi_{44} \end{bmatrix} \begin{bmatrix} \sigma_x \\ \sigma_y \\ \sigma_z \\ \tau_{xy} \\ \tau_{xz} \\ \tau_{yz} \end{bmatrix} \tag{4.11}$$

where ρ_x, ρ_y, and ρ_z, are the resistivities in the x, y, and z directions. ρ_{xy}, ρ_{xz}, and ρ_{yz} are the cross-resistivities. $\Delta\rho_x$, $\Delta\rho_y$, and $\Delta\rho_z$ are the changes in resistivity in the x, y, and z directions, $\Delta\rho_{xy}$, $\Delta\rho_{xz}$, and $\Delta\rho_{yz}$ are the changes in the cross-resistivities. π_{11}, π_{12}, $\pi_{13}$and π_{44} are the coefficients of the piezoresistive matrix. σ_x, σ_y, and σ_z are the stresses in the x, y, and z directions. τ_{xy}, τ_{xz}, and τ_{yz} are the shear stresses in the material.

For silicon, the cross-resistivity terms are much smaller than the resistivity terms, and can be ignored. Equation (4.11) simplifies to:

$$\begin{bmatrix} \Delta\rho_x/\rho_x \\ \Delta\rho_y/\rho_y \\ \Delta\rho_z/\rho_z \end{bmatrix} = \begin{bmatrix} \pi_{11} & \pi_{12} & \pi_{13} \\ \pi_{12} & \pi_{11} & \pi_{12} \\ \pi_{13} & \pi_{12} & \pi_{11} \end{bmatrix} \begin{bmatrix} \sigma_x \\ \sigma_y \\ \sigma_z \end{bmatrix} \tag{4.12}$$

If the structure is not subject to elastic deformation, than the response of the structure is linear. The stresses in sensor regions A and B, shown in figure 4.1, are then given by:

$$\begin{bmatrix} \sigma_x \\ \sigma_y \\ \sigma_z \end{bmatrix}_A = \begin{bmatrix} A_{11} & A_{12} & A_{13} \\ A_{21} & A_{22} & A_{23} \\ A_{31} & A_{32} & A_{33} \end{bmatrix} \begin{bmatrix} F_x \\ F_y \\ F_z \end{bmatrix}, \begin{bmatrix} \sigma_x \\ \sigma_y \\ \sigma_z \end{bmatrix}_B = \begin{bmatrix} B_{11} & B_{12} & B_{13} \\ B_{21} & B_{22} & B_{23} \\ B_{31} & B_{32} & B_{33} \end{bmatrix} \begin{bmatrix} F_x \\ F_y \\ F_z \end{bmatrix} \tag{4.13}$$

Equation (4.12) can be combined with equation (4.13) to show how the resistance change is proportional to the forces applied. If the results are simplified by neglecting forces in the z-direction, as well as σ_z, the following results are obtained for the resistance change at A:

$$\begin{bmatrix} \Delta\rho_x/\rho_x \\ \Delta\rho_y/\rho_y \\ \Delta\rho_z/\rho_z \end{bmatrix}_A = \begin{bmatrix} \pi_{11}A_{11} + \pi_{12}A_{21} & \pi_{11}A_{12} + \pi_{12}A_{22} \\ \pi_{12}A_{11} + \pi_{11}A_{21} & \pi_{12}A_{12} + \pi_{11}A_{22} \\ \pi_{13}A_{11} + \pi_{12}A_{21} & \pi_{13}A_{12} + \pi_{12}A_{22} \end{bmatrix} \begin{bmatrix} F_x \\ F_y \end{bmatrix} \tag{4.14}$$

with a similar result for the resistance change at B:

$$\begin{bmatrix} \Delta\rho_x/\rho_x \\ \Delta\rho_y/\rho_y \\ \Delta\rho_z/\rho_z \end{bmatrix}_B = \begin{bmatrix} \pi_{11}B_{11}+\pi_{12}B_{21} & \pi_{11}B_{12}+\pi_{12}B_{22} \\ \pi_{12}B_{11}+\pi_{11}B_{21} & \pi_{12}B_{12}+\pi_{11}B_{22} \\ \pi_{13}B_{11}+\pi_{12}B_{21} & \pi_{13}B_{12}+\pi_{12}B_{22} \end{bmatrix} \begin{bmatrix} F_x \\ F_y \end{bmatrix} \tag{4.15}$$

If we attempt to measure resistance change in the x-direction at both A and B, we obtain the following result:

$$\begin{bmatrix} (\Delta\rho_x/\rho_x)_A \\ (\Delta\rho_x/\rho_x)_B \end{bmatrix} = \begin{bmatrix} \pi_{11}A_{11}+\pi_{12}A_{21} & \pi_{11}A_{12}+\pi_{12}A_{22} \\ \pi_{11}B_{11}+\pi_{12}B_{21} & \pi_{11}B_{12}+\pi_{12}B_{22} \end{bmatrix} \begin{bmatrix} F_x \\ F_y \end{bmatrix} \tag{4.16}$$

By simply inverting the coefficient matrix, we can see that the forces can be recovered, so long as the coefficient matrix is not singular:

$$\begin{bmatrix} F_x \\ F_y \end{bmatrix} = \begin{bmatrix} \pi_{11}A_{11}+\pi_{12}A_{21} & \pi_{11}A_{12}+\pi_{12}A_{22} \\ \pi_{11}B_{11}+\pi_{12}B_{21} & \pi_{11}B_{12}+\pi_{12}B_{22} \end{bmatrix}^{-1} \begin{bmatrix} (\Delta\rho_x/\rho_x)_A \\ (\Delta\rho_x/\rho_x)_B \end{bmatrix} \tag{4.17}$$

Designing the structure so that A_{ij} is not equal to B_{ij} will prevent the coefficient matrix from being singular. This can be accomplished simply by ensuring the structure is sufficiently asymmetric that the response in A is not equal to the response in B. The coefficient matrix in (4.17) can be simplified further to obtain:

$$\begin{bmatrix} F_x \\ F_y \end{bmatrix} = \begin{bmatrix} S_{11} & S_{12} \\ S_{21} & S_{22} \end{bmatrix}^{-1} \bullet \begin{bmatrix} (\Delta\rho_x/\rho_x)_A \\ (\Delta\rho_x/\rho_x)_B \end{bmatrix} \tag{4.18}$$

where S_{11} is the change in resistivity in region A in response to a unit x-force, S_{12} is the change in resistivity in region A in response to a unit y-force, S_{21} is the change in resistivity in region B in response to a unit y-force, and S_{22} is the change in resistivity in region B in response to a unit y-force,.

4.4.3. Sensor Finite Element Method Analysis

Determining the structural response coefficients can be done using a commercial finite element package, such as ANSYS. The proposed sensor geometry is shown in figure 4.18:

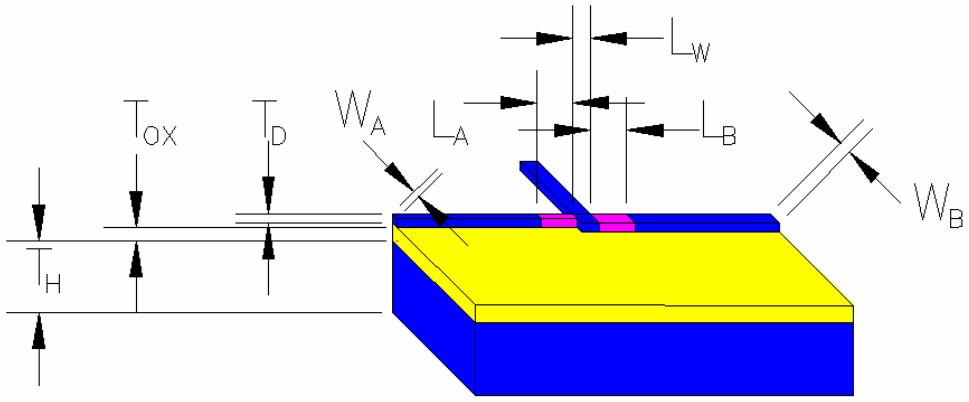

Figure 4.17. Proposed Sensor Geometry

L_W represents the space allowed for the airfoil, which also represents the maximum allowable airfoil chord. L_W is set to 100 microns. L_A and L_B are the lengths of the sensor regions, and are set to 50 microns. W_A and W_B are the widths of the sensor regions. W_A is set to 10 microns, and W_B is set to 20 microns. T_D, T_{OX}, and T_H represent the thickness of the device, oxide, and handle layers of the SOI wafer. For commercial wafers, the thickness of the handle layer is typically 500 microns, and the thickness of the device and oxide layers varies. This geometry was analyzed using device thicknesses of 1, 1.5, 2, 3, and 5 microns, and oxide thicknesses of 1, 1.5, 2, and 3 microns, using the finite element mesh shown in figure 4.19, and the ANSYS commercial finite element package. (ANSYS, 1999). A force of 1 N is applied in the location of the airfoil, in the x and y directions, and the results used to determine the sensor sensitivity.

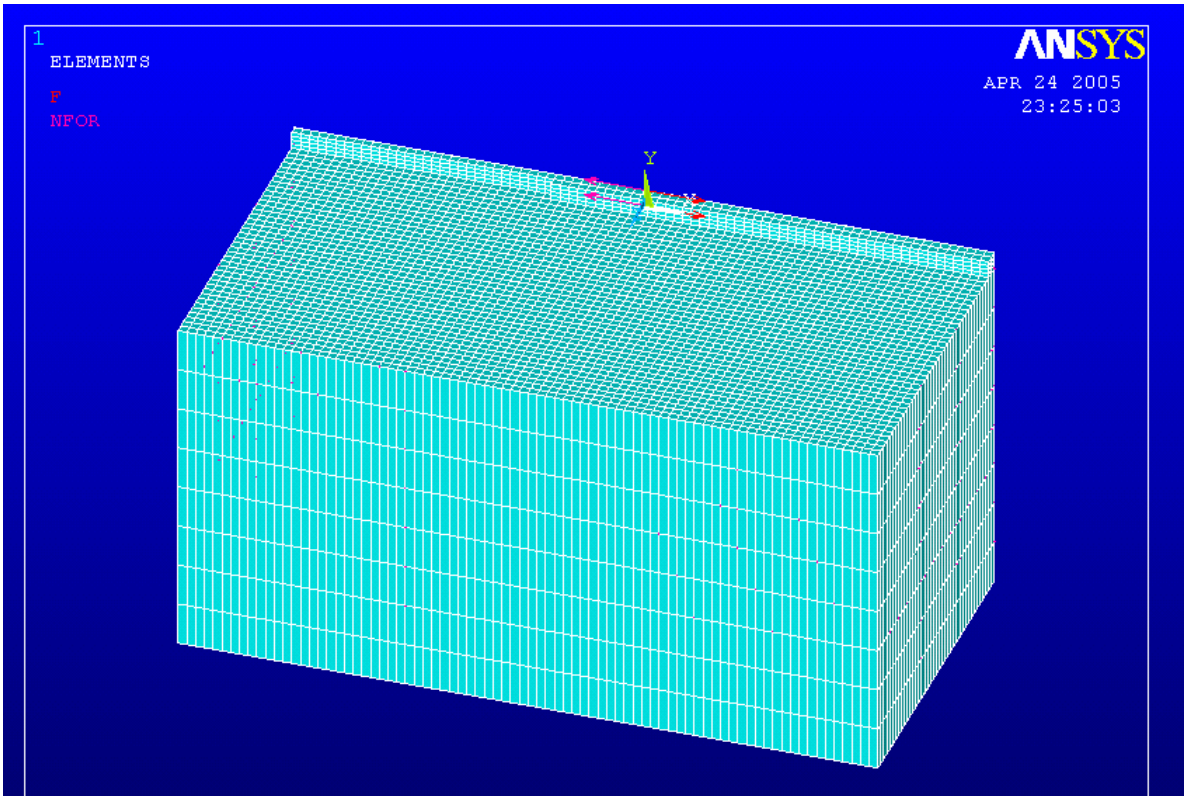

Figure 4.18. Finite Element Mesh

Finding the change in resistance in the sensor requires integrating the sensor resistivity over the entire sensor volume. The FEM results for the sensor region were is from the finite-element model, and integrated to find the resistance change in the sensor regions based in response to x and y forces using the following equations:

$$S_{11} = (\Delta\rho_x / \rho)_A\big|_{x-force} = \iiint_v [\pi_{11} \quad \pi_{11} \quad \pi_{13}][\sigma_x \quad \sigma_y \quad \sigma_z]^t_{x-force} dV \tag{4.19}$$

$$S_{12} = (\Delta\rho_x / \rho)_A\big|_{y-force} = \iiint_v [\pi_{11} \quad \pi_{11} \quad \pi_{13}][\sigma_x \quad \sigma_y \quad \sigma_z]^t_{y-force} dV \tag{4.20}$$

$$S_{21} = (\Delta\rho_x / \rho)_B\big|_{x-force} = \iiint_v [\pi_{11} \quad \pi_{11} \quad \pi_{13}][\sigma_x \quad \sigma_y \quad \sigma_z]^t_{x-force} dV \tag{4.21}$$

$$S_{22} = (\Delta\rho_x / \rho)_B\big|_{y-force} = \iiint_v [\pi_{11} \quad \pi_{11} \quad \pi_{13}][\sigma_x \quad \sigma_y \quad \sigma_z]^t_{y-force} dV \tag{4.22}$$

The results of integrating these equations, over the complete range of oxide and device layer thicknesses, are shown as figures 4.20 through 4.23. These results show that the asymmetry condition required for the sensor is met. They also show that the sensor sensitivity, while changing based on device and oxide layer thickness, remains within the same order of magnitude for a variety of wafer configurations.

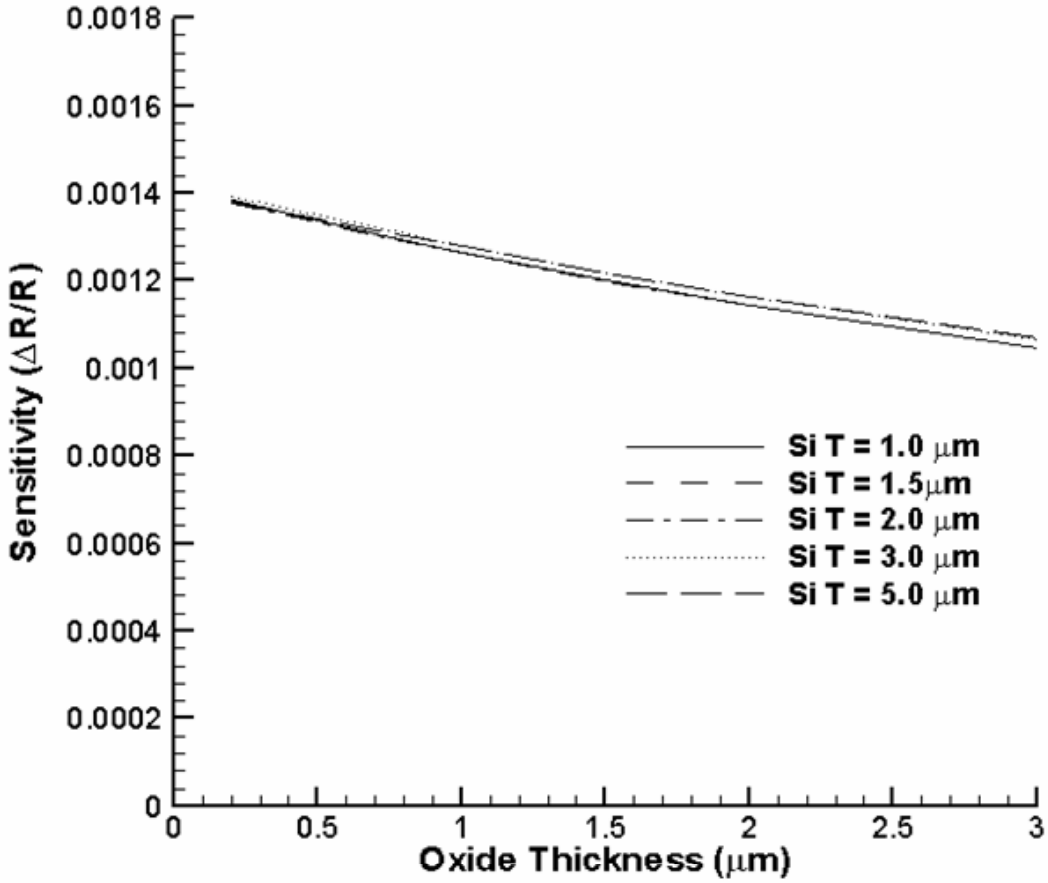

Figure 4.19. X-Sensitivity of Left-Hand Sensor Region

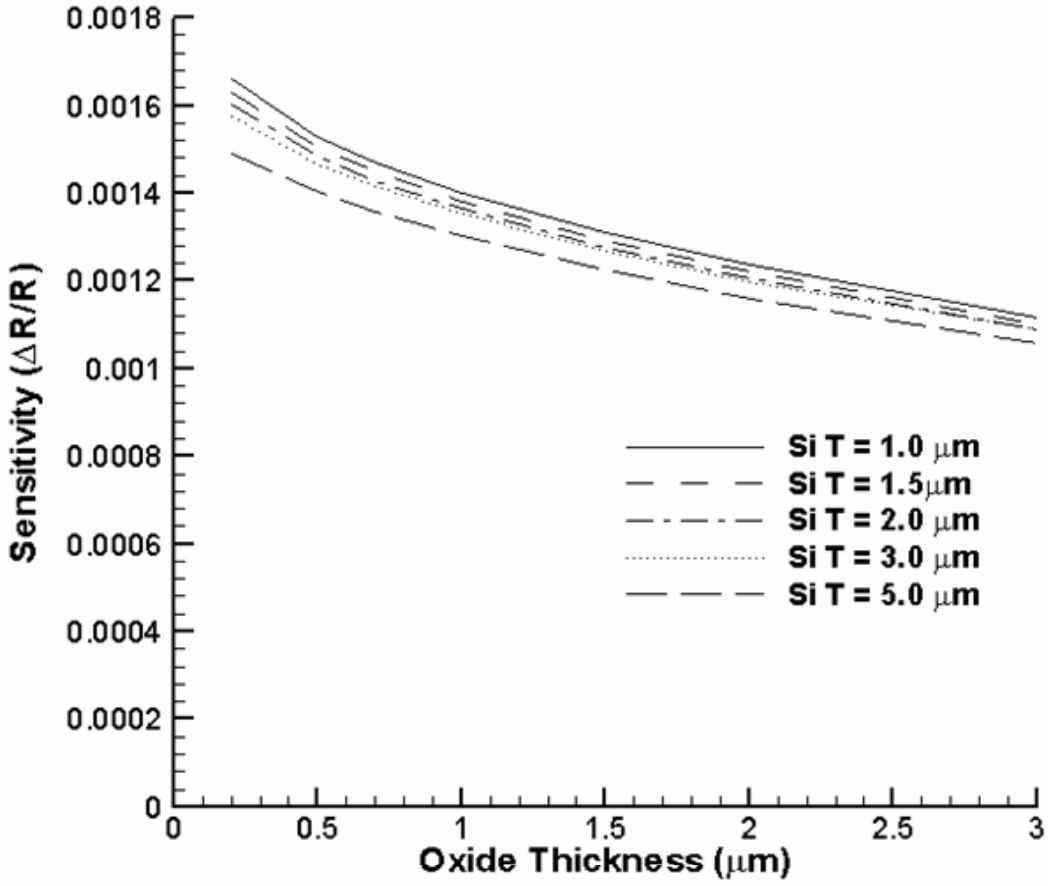

Figure 4.20. X-Sensitivity of Right-Hand Sensor Region

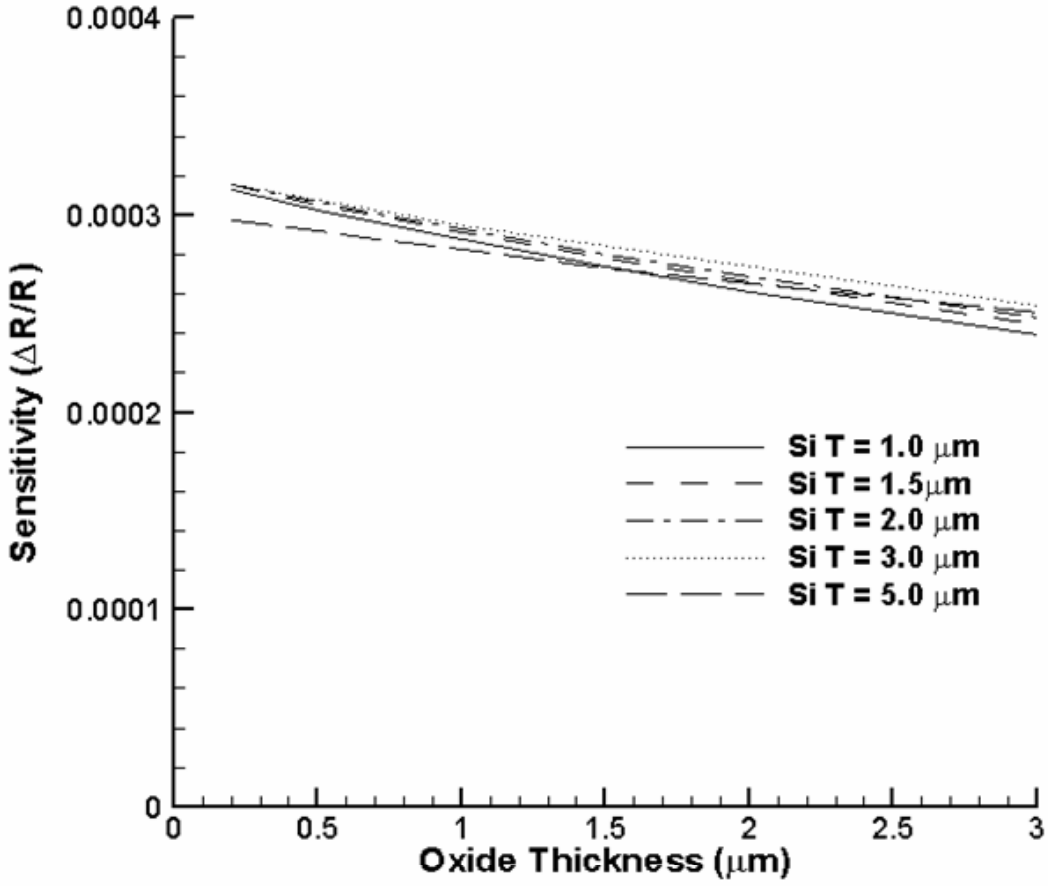

Figure 4.21. Y-Sensitivity of Left-Hand Sensor Region

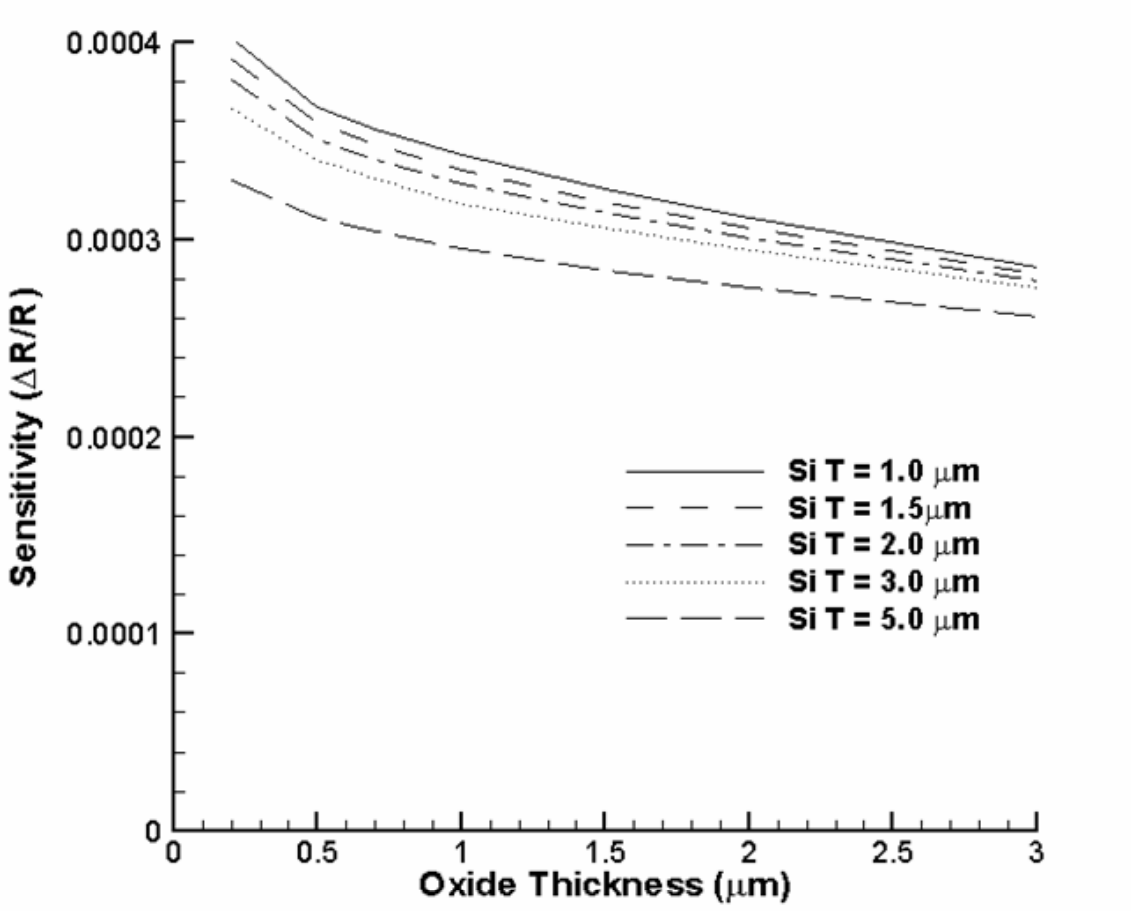

Figure 4.22. Y-Sensitivity of Right-Hand Sensor Region

4.5.Conclusions

This chapter demonstrates the structural considerations that limit fabrication of micro-machined airfoils. A manufacturing process is developed, and demonstrated, that allows fabrication of meso-scale beams with a micro-scale cross-section from crystalline silicon. Finite element analysis of a piezoresistive sensor, with the capability to simultaneously read forces in the x and y-directions, shows that the expected drag force can be successfully measured.

CHAPTER 5

FABRICATION, INSTALLATION, AND CALIBRATION OF THE COMBINED AIRFOIL AND FORCE SENSOR

5.1. Introduction

This chapter describes the fabrication of an integrated 100 micron chord airfoil with a piezoresistive force sensor. A complete manufacturing process for the combined airfoil with flow sensor is described, culminating in the installation of the airfoil in the tunnel described in Chapter 3. The integration of the force sensor into a data acquisition system is described. Because the airfoils did not survive testing, the potential failure modes of the airfoil are analyzed to determine the most likely cause of failure.

5.2. Device Fabrication

Several major modifications must be made to the process outlined in section 4.2.2 to allow fabrication of the integrated sensor device. The fabrication process is broken into several separate processes:

1. Preparation of first handle wafer
2. Preparation of second handle wafer.
3. Top-side processing of device wafer
4. Integration of handling wafers with device wafers.
5. Installation of device in tunnel

5.2.1. Preparation of first handle wafer

Because the devices are fabricated using an SOI wafer with crystalline silicon, the process must be modified to minimize inter-molecular attraction between the device wafer and the handle wafer. This is accomplished by depositing silicon oxide as a coating wafer on the handling wafer, using the process shown in figure 5.1:

Step 1. The process begins from a bare silicon wafer

Step 2. A 0.5 micron thick layer of SiO_2 is deposited on the handle wafer using LPCVD.

Step 3. SC1827 photoresist is deposited on the top of the wafer, and the microchannel pattern defined using photolithography. The microchannels are then etched using a 1:1 buffered HF wet etch to remove the oxide over the channels.

Step 4. A DRIE process is used to etch the microchannels to a depth of 50 microns. The photoresist is then removed from the wafer.

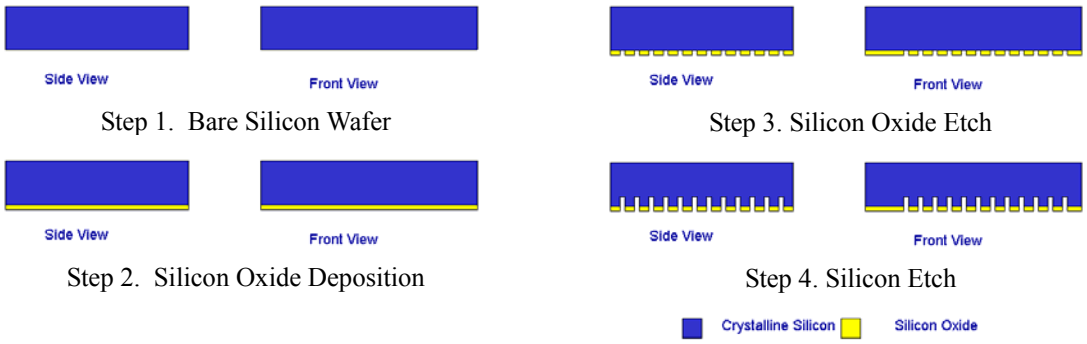

Figure 5.1. Process Flow for preparation of first handle wafer

5.2.2. Preparation of second handle wafer.

The preparation of the second handle wafer was also modified to reduce inter-molecular forces between layers of silicon. However, since there was no need to etch through this wafer, a coating of gold is used instead of silicon oxide. Use of gold instead of silicon oxide eases mechanical removal of photoresist.

Step 1. The process begins from a bare silicon wafer

Step 2. SC1827 photoresist is deposited on the top of the wafer, and the support structure defined using photolithography. The shape of the support structure is defined using a 100 micron deep DRIE to remove silicon. The photoresist was then removed.

Step 3. A 300-angstrom thick layer of chromium was sputtered onto the wafer to allow adhesion between gold and silicon, followed by a 3000-angstrom thick layer of gold.

The process flow is shown as figure 5.2.

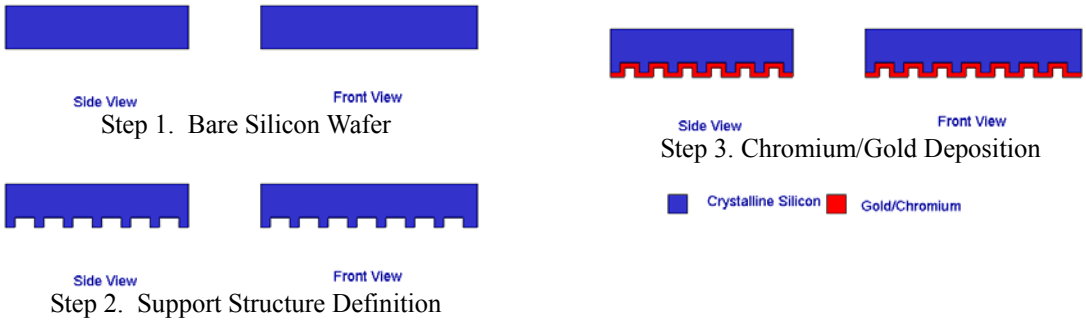

Figure 5.2. Process Flow for preparation of second handle wafer

5.2.3. Processing of device wafer

The most complex of the fabrication processes is the fabrication of the sensor, airfoil, and wiring on the SOI wafer. The complete process flow is shown as figure 5.3:

Step 1. This process begins with a bare SOI wafer. For the final production run, a 450 micron thick wafer with a device layer of 5 microns and a buried oxide layer thickness of 1 micron was used

Step 2. LPCVD is used to deposit a 1 micron thick oxide masking layer on the front side of the wafer.

Step 3. SC1827 photoresist is deposited on the topside of the wafer, and the oxide mask pattern is defined using photolithography. The oxide mask is then etched using a 1:1 etch of buffered HF, and the photoresist removed from the wafer.

Step 4. A boron deposition furnace is used to deposit boron into the sensing regions to a concentration of 10^{21} ions per cubic centimeter. An 8 hour, 1000° C anneal is used to ensure that boron is distributed evenly throughout the sensing regions.

Step 5. The oxide mask is removed using a 1:1 etch of buffered HF.

Step 6. An 8 micron thick backside masking layer of oxide is deposited using LPCVD.

Step 7. SC1827 photoresist is deposited on the topside of the wafer, and the airfoil pattern is defined using photolithography. The front of the wafer is then etched using a DRIE process to define the airfoil and sensor region geometry. The photoresist is then removed from the wafer.

Step 8. AZ9260 photoresist is deposited on the front-side of the wafer. Photolithography is used to create a reverse pattern of the wiring in the photoresist. The wafer is metalized by sputtering a 300-angstrom thick layer of chromium and a 3000-angstrom thick layer of gold. The excess gold and chromium are removed via a lift-off process.

Step 9. SC1827 photoresist is deposited on the backside of the wafer, and the mounting pattern is defined using photolithography. A 1:1 buffered HF etch is used on the backside to define the mounting shape.

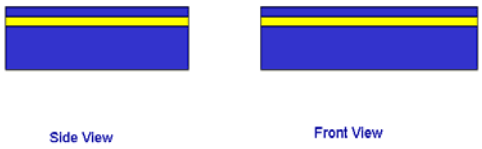

Step 1. Bare SOI Wafer

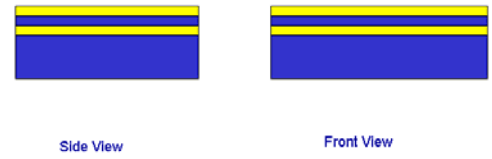

Step 2. Deposit topside masking layer of oxide

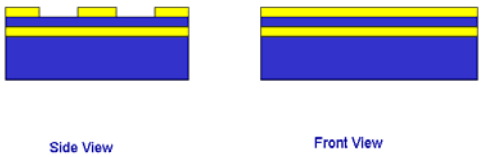

Step 3. Define masking layer of oxide

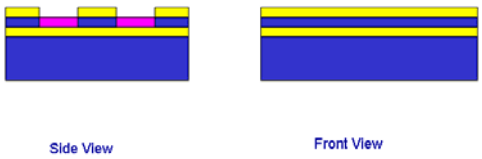

Step 4. Deposit boron into sensing regions

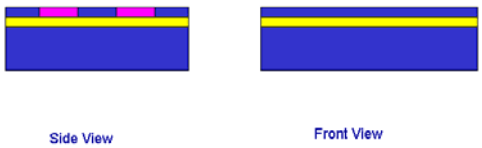

Step 5. Remove topside masking layer of oxide

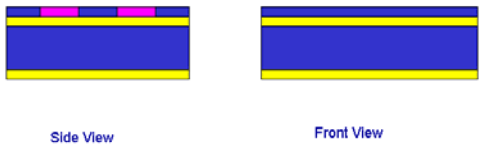

Step 6. Deposit backside masking layer of oxide

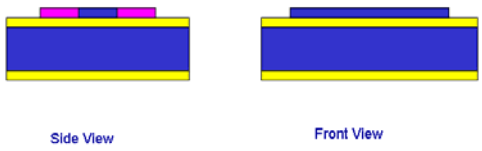

Step 7. Define airfoil geometry

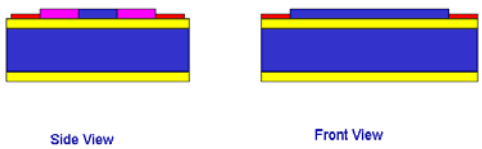

Step 8. Deposit wiring

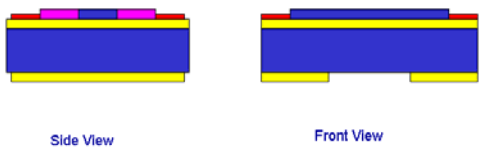

Step 9. Define backside masking layer of oxide

Figure 5.3. Process Flow for Preparation of Device Wafer

A photograph of the sensor region at the end of this process flow is shown as figure 5.4:

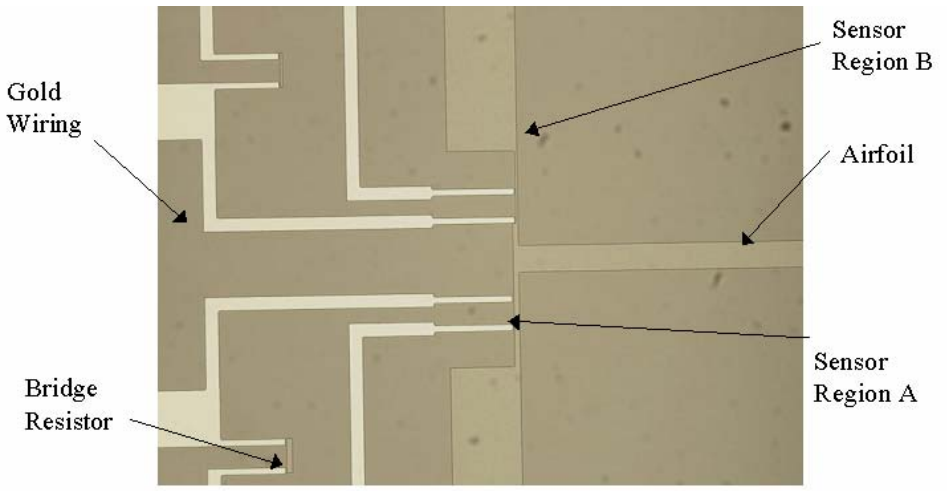

Figure 5.4. Photograph of Sensor

5.2.4. Integration of handle wafers with device wafer and Tunnel Release

After the sensor region and airfoil structure are completed, the device wafer is then bonded with a pair of handle wafers. The material underneath the airfoil is then removed, and the airfoil installed in the tunnel. The complete process, as shown in figure 5.5, is:

Step 1. The first handle wafer is attached using hard-baked AZ9260 photoresist.

Step 2. AZ9260 photoresist is deposited on the exposed side of the handling wafer. Photolithography is used to create the pattern of protective plates. A DRIE process is used to etch through the handle wafer to define the protective plates. The buried layer of photoresist forms an etch stop.

Step 3. The second handle wafer is attached using hard-baked AZ9260 photoresist.

Step 4. A DRIE process is used to etch through the device wafer to define the individual dies, using the backside oxide as a masking layer. The buried oxide layer forms an etch stop.

Step 5. The oxide under the airfoil is removed using a 1:1 etch of buffered HF.

Step 6. The individual devices with protective plates are removed from the second handling wafer mechanically.

Step 7. The device is attached using epoxy to the tunnel mounting.

Step 8. The protective plate is removed.

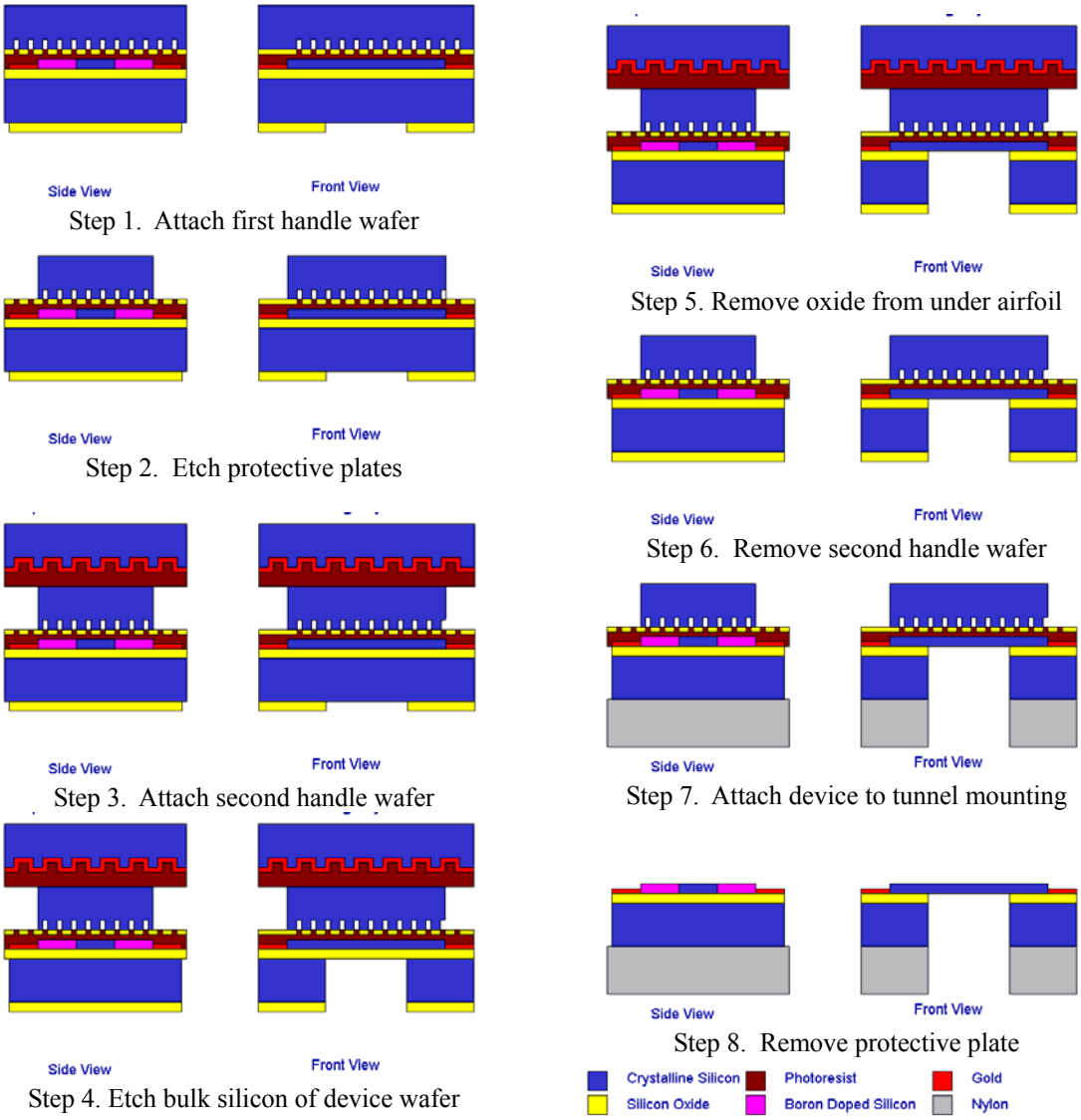

Figure 5.5. Process Flow for Integration and Tunnel Release

Figure 5.6 shows the device after step 6, prior to installation in the tunnel. The sensors with mountings are on the right and left of the photograph. The brownish surface is the photoresist on the device.

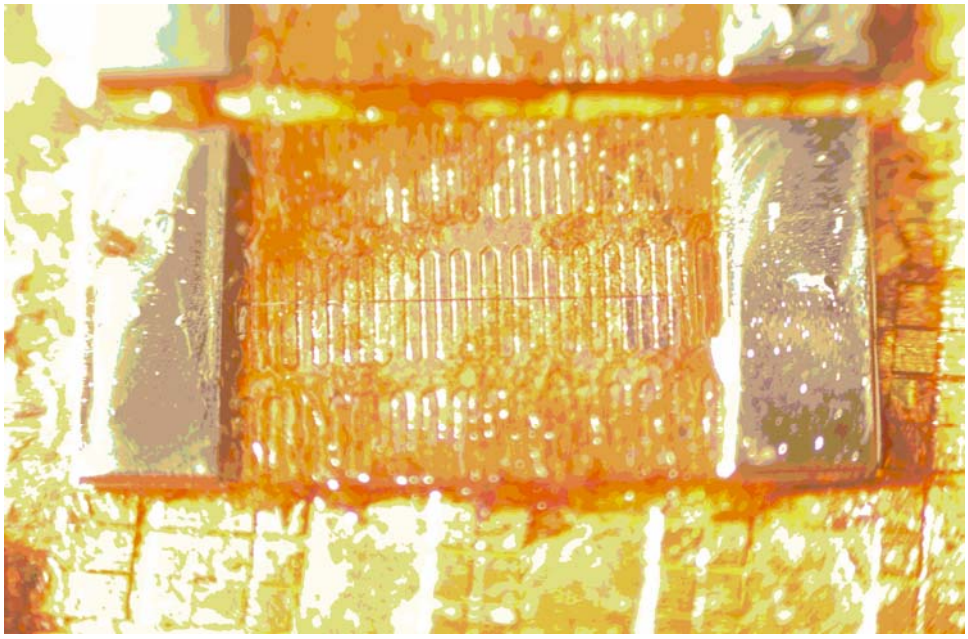

Figure 5.6. Device Prior to Mounting

To reduce the mechanical force on the airfoil during release, a mechanical lifter was installed in the tunnel. As shown in figure 5.7, a micrometer is attached to the protective plate to minimize lateral movement of the plate during the release process.

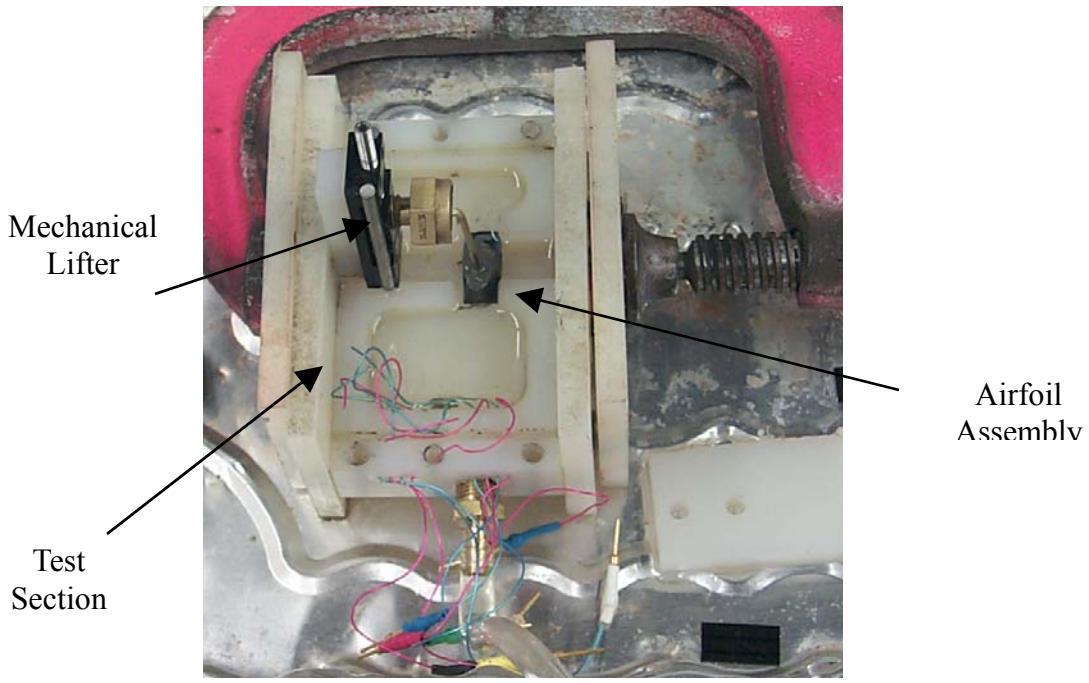

Figure 5.7. Mechanical Lifter Installation

Even with the mechanical lifter, the breakage rate on the devices is over 50 percent. A successfully released airfoil is shown as figure 5.8 below.

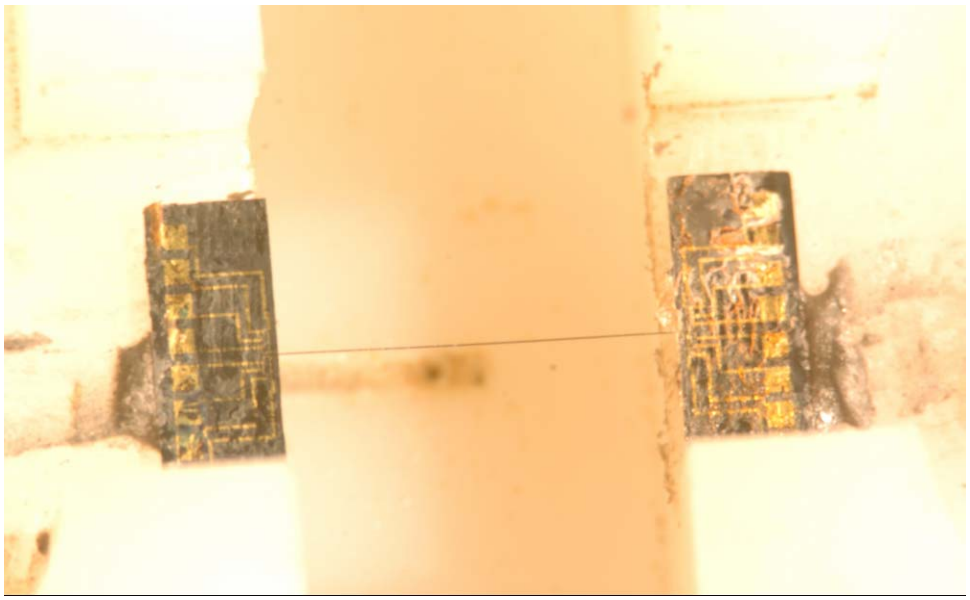

Figure 5.8. Released Airfoil

After release, devices were examined using the FEI Quanta 200 3D Focused Ion Beam Environmental Scanning Electron Microscope in low pressure at the University of Michigan Electron Microbeam Analysis Laboratory. Figure 5.9 shows the mounting point where the beam joins the sensor region. This photograph shows that the beam retains its shape as it joins the mounting point. It also shows that the through-wafer etch required to release the backside of the beam overlaps the freestanding beam by approximately 100 microns. Because of the sacrificial oxide layer, the beam is still free-standing in this area.

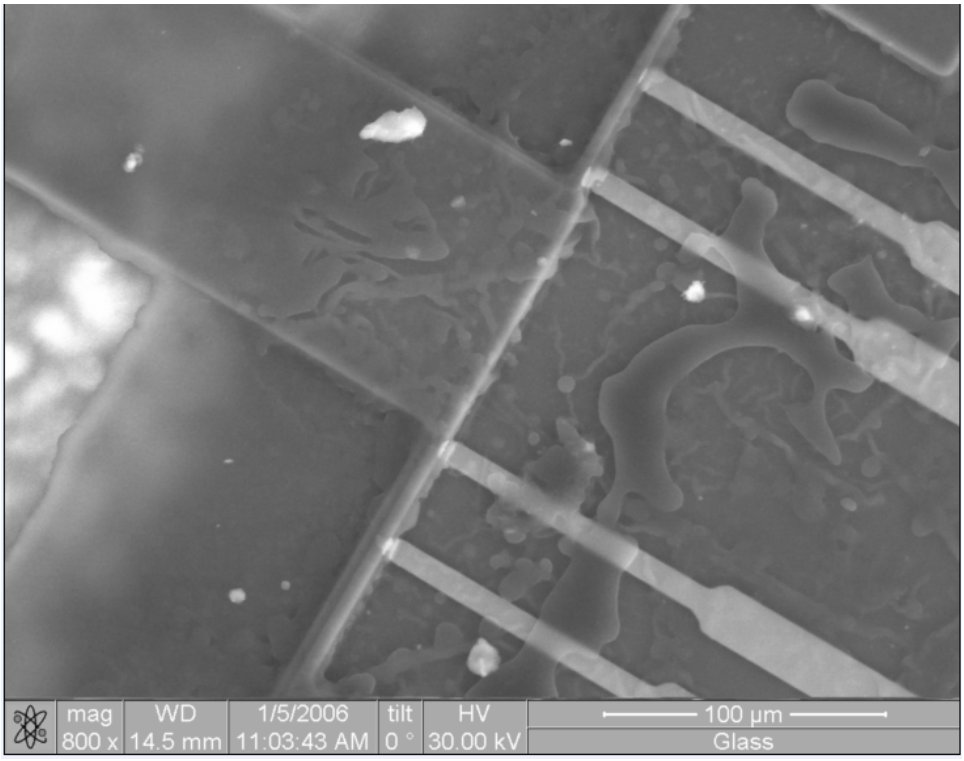

Figure 5.9. Electron Microscope Image of Sensor Region

Figure 5.10 shows the freestanding beam at a 35 degree angle. This photograph shows that the beam retains a rectangular cross-section during processing.

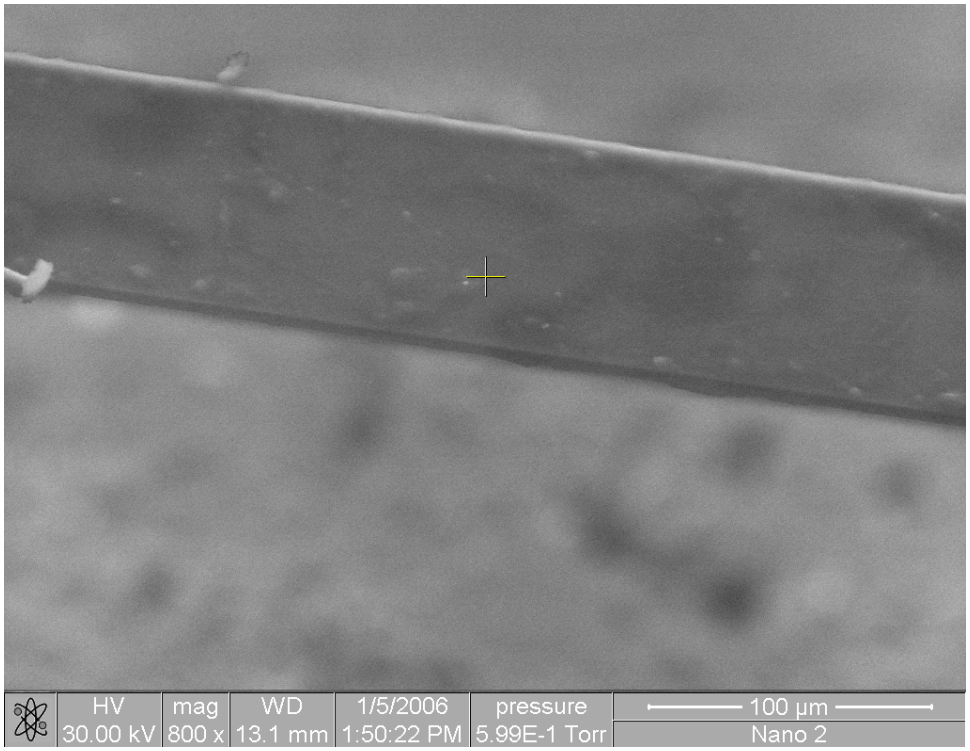

Figure 5.10. Electron Microscope Image of Airfoil Structure

5.3. Electrical Installation

Integration of the sensor design into a data acquisition system required several steps: design of a Wheatstone Bridge circuit, selection of a data acquisition system, design of the actual interconnects between the chip and the data acquisition system, and the selection of a power supply.

5.3.1. Wheatstone Bridge Design

The piezoresistive sensing regions must be integrated into a data acquisition system. The first step in doing this is to integrate the sensors into a Wheatstone Bridge circuit, as shown in figure 5.11. The output voltage of the Wheatstone bridge will be proportional to the change in resistance of the sensor:

$$(V_4 - V_2) = \frac{\Delta R_B}{4R_B}(V_1 - V_3) \tag{5.1}$$

$$(V_8 - V_6) = \frac{\Delta R_A}{4R_A}(V_5 - V_7) \tag{5.2}$$

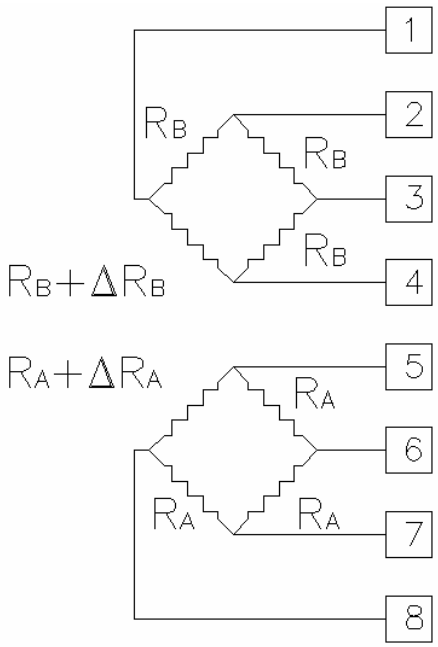

Figure 5.11. Wheatstone Bridge Sensor

The Wheatstone bridge circuits are fabricated on-chip, as shown in figure 5.12:

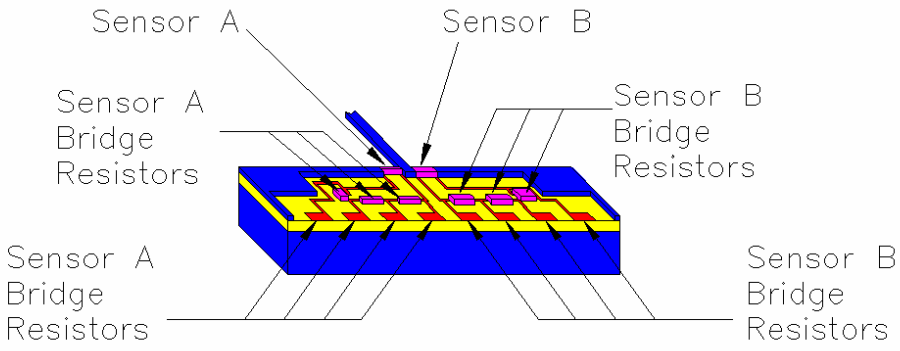

Figure 5.12. Wheatstone Bridge Layout

5.3.2. Data Acquisition

Using the electrical contact pads, the bridge circuits can then be integrated with an off-chip voltage source, amplifier, and data-acquisition system. The complete electrical schematic is shown as figure 5.13. The voltage inputs of the two Wheatstone bridges are connected to a DC power supply. The output voltages are connected to a pair of amplifiers, which are then connected to a data acquisition card.

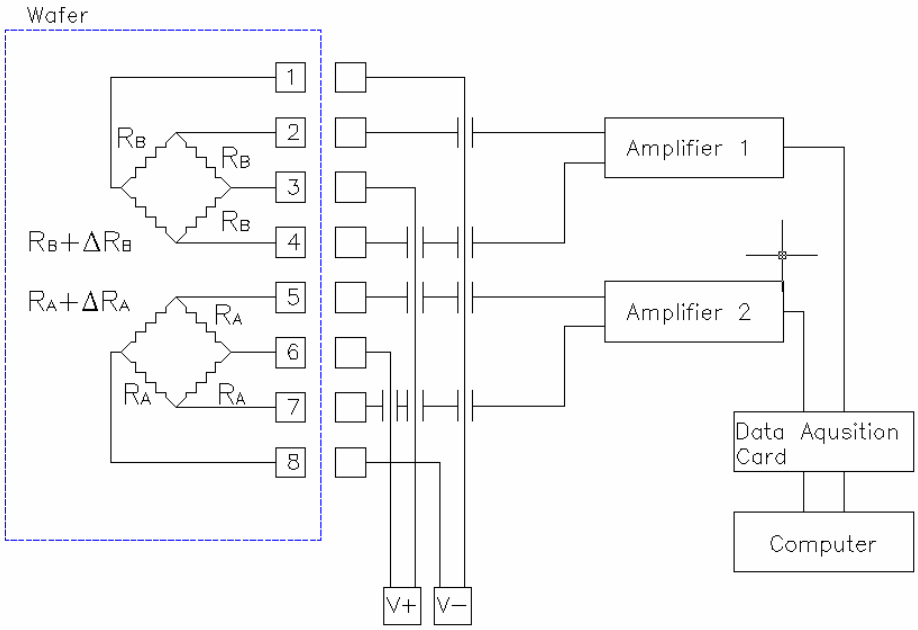

Figure 5.13. Electrical Installation

The amplifier circuit is shown in figure 5.14 below.

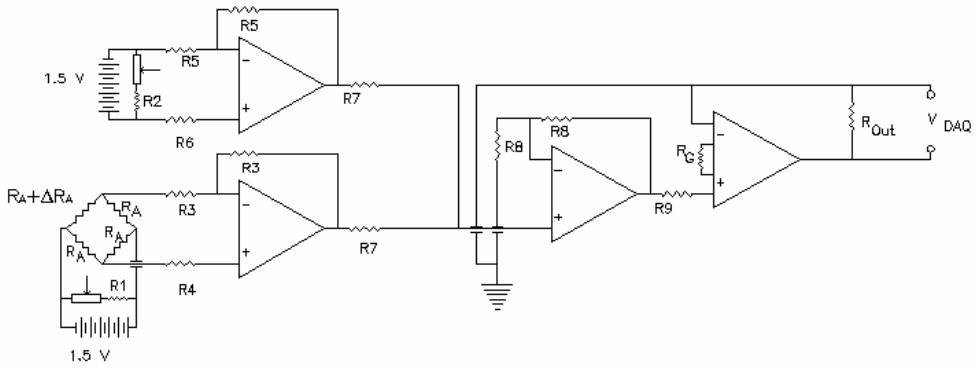

Figure 5.14. Amplifier Circuit

The amplifier is designed around the Analog Devices AMP02 instrumentation op-amp. (Analog Devices, 2006) Instead of filtering out system noise, the amplifier circuit shown is designed to have extremely low noise, by using 12 V batteries, instead of a standard DC voltage source. The bridge voltage is first fed into a voltage follower circuit. A second voltage follower circuit matches a variable voltage source. These two are added using a third op-amp, with the second voltage set to cancel the bridge offset. This sum is then amplified, and fed into the data acquisition system. Testing of the amplifier shows that the only noise present was thermal noise in the output resistor.

The gain of the amplifier is given by equation (5.3):

$$G = \frac{V_{CARD}}{V_{BRIDGE}} = \left(\frac{50\,k\Omega}{R_{Amp}}\right) + 1 \tag{5.3}$$

For this circuit, a resistance of 250 Ω was used, giving a gain of 201.

5.3.3. Device Interconnection

An exploded view of the attachment of the wiring to the device was done using the brackets shown in figure 5.15. A wiring support bracket was attached to the tunnel. The

wiring isolation bracket was then placed over the sensor. The wires were then attached to the contact pads using z-axis conductive tape. Figure 5.16 shows the parts after assembly.

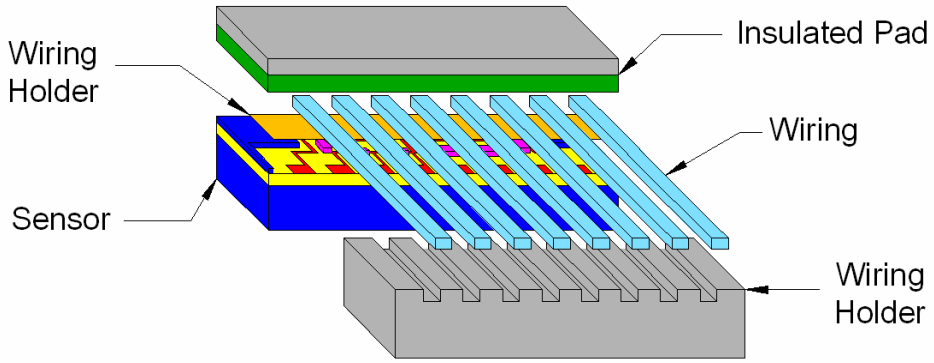

Figure 5.15. Wiring Installation (Exploded View)

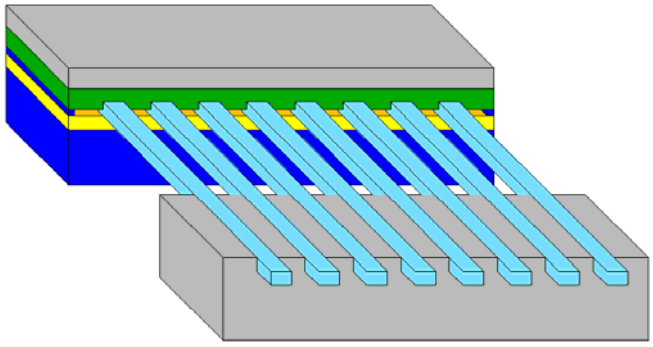

Figure 5.16. Wiring Installation

5.3.4. Power Supply Voltages

To minimize the noise in the system, DC batteries were used as voltage sources. While this might not be a suitable power supply for long-term operation, the power consumption in the system is low enough that testing may be done using this as a source. Before testing could begin, it was necessary to select the supply voltage. Based on equations 5.1 and 5.2, the signal strength will be directly proportional to the input voltage selected. However, thermal considerations limit the maximum power of the system.

Because piezoresistive coefficients are extremely sensitive to temperature, the voltage is set using a maximum allowable temperature rise of 1 K. The primary method for dissipating heat from the sensor regions will be conduction through the oxide layer into the bulk silicon. A simplified thermal model of the system is given as figure 5.17 below.

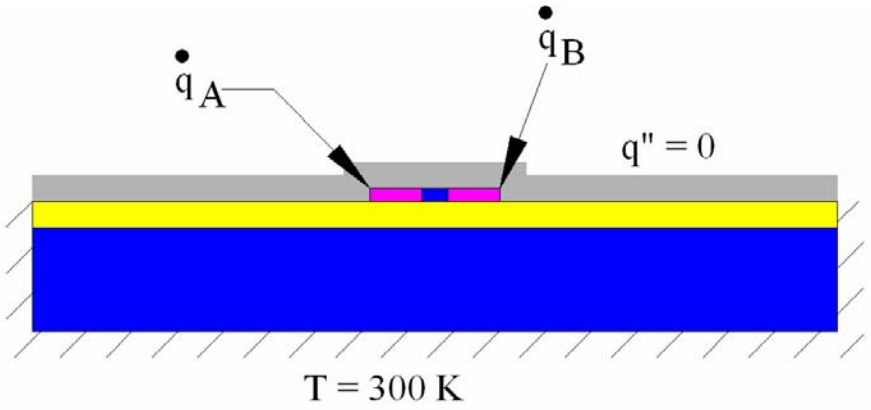

Figure 5.17. Boundary Conditions for Thermal Analysis

The heat generation rate $\dot{q}$ represents the energy dissipation per unit volume of the sensor areas. The thermal flux q" represents the heat loss per unit area on a surface. The boundary conditions are q" equal to zero at all exposed surfaces, and T equal to 300 K for the bulk silicon.

The finite element mesh used in chapter 4 for the structural analysis was re-used for thermal analysis. For a temperature rise of 1 K in each resistor, the maximum allowable heat dissipation in the resistors is 1.0 μW for sensor A, and 2.0 μW for sensor B.

Using the electrical conductivity of boron-doped silicon (Smith, 1954), we can make initial estimates of the electrical resistance of sensors A and B using equation 5.4:

$$R_A = \frac{L_A}{\rho t_A w_A} \tag{5.4}$$

where R is the resistance, L is the length of the sensing element, ρ is the electrical conductivity, t is the element thickness, and w is the element width. Using the dimensions from chapter 3, we can estimate that sensor A will have a resistance of R_A equal to 700 kΩ, and sensor B will have a resistance of R_B equal to 350 kΩ.

The maximum allowable voltage drop across each resistor can be determined by using the power dissipation equation:

$$P = \frac{V^2}{R} \tag{5.5}$$

where P is the power, V is the voltage across the resistor, and R is the resistance. Preliminary thermal analysis suggested that the maximum allowable voltage across each resistor was 0.85 V, or 1.7 V across the bridge. Values in excess of this may cause noise in the system.

5.4. Airfoil Failure Modes

Attempts were made to calibrate the airfoil x-direction force sensors by rotating the test section 90 degrees, and then by placing weights on the airfoil. The weights, shown in figure 5.18, are fabricated from paper and brass rods. They are designed to distribute a force across the entire airfoil.

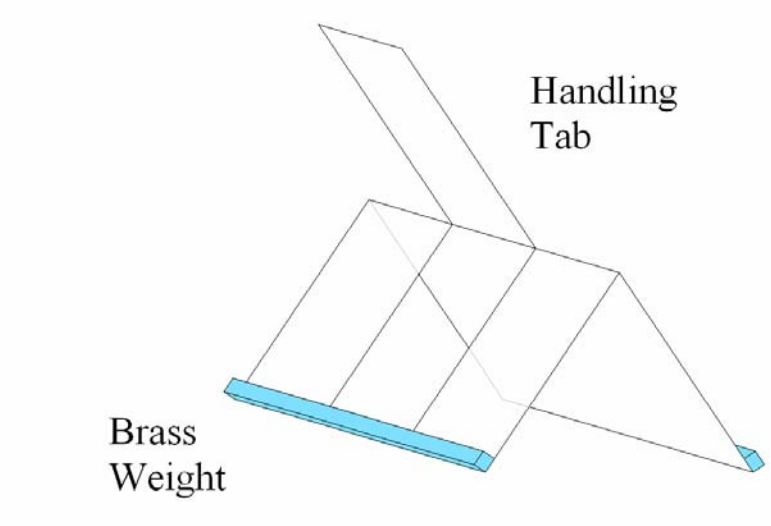

Figure 5.18. Airfoil x-direction Force Calibration Weight

While the airfoil could withstand the weight of the test structure, in practice, the electrostatic attraction of the weights, whether paper or metal, led to airfoil failure. Airfoils would break when the weight was removed during calibration.

Attempts to test the airfoil were also unsuccessful, because the airfoils broke during system transients. This result is surprising. Several possible explanations exist for this, each of which will be discussed in depth.

5.4.1 Manufacturing Tolerance Analysis

The first possible explanation is that the airfoil structural calculations over-estimate the strength of the beams because of manufacturing tolerances. Re-arranging equation (4.1), we find that the maximum force per unit span is directly proportional to the thickness t, as well as the yield strength σ_{yield}.

$$f_{max} = \frac{2\,tc^3}{3S}\sigma_{yield} \tag{5.6}$$

The thickness of the beams was directly measured during the fabrication process. The measured thickness varied between 4.5 and 4.8 microns, on a wafer with a nominal

device layer thickness of 5.0 microns. While a 10 percent error will affect the strength of the device, the large margins of safety added to the device design suggest that a 10 percent difference in thickness cannot be the cause of the failure. The airfoil did survive a .025 g weight being attached to it during calibration, as well as the forces of the release process, which were expected to be a larger concern than the aerodynamic forces.

5.4.2. Material Property Analysis

The second possible explanation is that the yield strength of the silicon was not as high as expected. The processing of the silicon may have led to the silicon being significantly weaker than expected. Without actually testing the silicon wafers used, it is difficult to rule this out. However, due to the margins of safety used in the design analysis, the silicon used in the testing would have to be at least 30 percent weaker than the published properties for this explanation to be likely.

An additional materials issue is the possibility of thermal expansion due to the mismatch in materials properties between the silicon of the airfoil and the nylon of the tunnel. The thermal expansion coefficient of silicon has been measured as $2.33 \times 10^{-6}/^{o}C$. (Peterson, 1982) The thermal expansion coefficient of the nylon used in the tunnel is given by the manufacturer as $6.3 \times 10^{-5}/^{o}C$. The difference between these values, $6.1 \times 10^{-5}/^{o}C$, suggests that if the tunnel is allowed to cool significantly after the release of an airfoil, the airfoil will sag. Because the lab temperature was not allowed to change by more that $2\ ^{o}C$, this was not observed during testing.

5.4.3. Potential Error in Drag Forces

A third possible explanation for the failure of the silicon airfoil in the tunnel is that the airfoil forces are significantly higher than those predicted by the flow models used. It

is possible that the airfoil actually sheds vortices during operation, even at the low Reynolds numbers used in this testing. The steady flow approximations used in this thesis, as well as the previous calculations performed using the information preservation method on similar geometries, would not detect this phenomena. Therefore, we recommend that the forces generated on micro-machined airfoils be investigated using CFD methods that allow for transient phenomena. Analysis of flow separation in MEMS (Baysal, 2002) shows that slip flows separate at lower Reynolds numbers than non-slip flows. Because separation will increase vortex shedding, codes should be run under both slip and no-slip conditions. If the transient forces lead to a peak force that is 2-3 times the force predicted by boundary layer theory, this may be the cause of airfoil breakage. Confirmation of this theory will require development of a transient CFD code that incorporates slip effects.

5.4.4. Failure due to Lift Forces

A fourth possible explanation for the airfoil failure is forces in the y-direction acting on the airfoil. As shown in figure 4.10, the airfoil is orders of magnitude mode fragile in the y-direction than in the x-direction. Solving equation (4.7) to find the maximum allowable force in the y-direction gives the result:

$$f_{max} = \frac{2\,t^3 c}{3S}\sigma_{yield} \tag{5.7}$$

The force is a function of the coefficient of lift C_L for the beam, the beam dimensions, and the dynamic pressure:

$$f = c * C_L * \frac{1}{2}\rho U^2 \tag{5.8}$$

Substituting (5.8) into (5.7) gives an expression for the maximum allowable coefficient of lift:

$$C_L\big|_{max} = \frac{\frac{2t^3\sigma_{yield}}{S}}{\frac{1}{2}\rho U^2} \tag{5.9}$$

Equation (5.9) suggests that the allowable coefficient of lift for a micro-machined airfoil structure is very small. Figure 5.19 shows the maximum allowable coefficient of lift for the span of 1 cm, and the thickness of 5 microns, as used in this experiment:

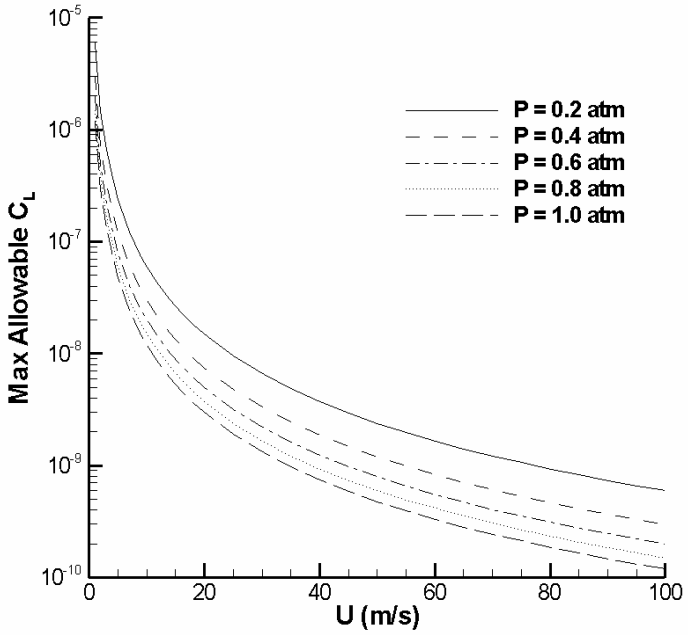

Figure 5.19. Allowable Lift Coefficient as a Function of Velocity

Figure 5.19 shows that the coefficient of lift must be neglible for the airfoil to survive testing. However, research into vortex shedding at low Reynolds numbers (Breuer, 2000) shows that, for a square cylinder the average lift force is zero, there is actually a time-dependent lift force. These computations suggest that the instantaneous

coefficient of lift may be of an order of magnitude of 1. Comparison of this result with figure 5.19 suggests that creating a micro-machined airfoil that will survive vortex shedding may be physically impossible.

5.4.5. Airfoil Resonance

The expected frequency of vortex shedding should also be considered in this analysis. Vortex shedding is characterized using the Strouhal number, or St, given in equation 5.10:

$$St = \frac{fc}{\mathrm{U}} \tag{5.10}$$

where f is the vortex shedding frequency, c is the airfoil chord, and U is the air velocity.

Experiments with flat plates at the macro-scale suggest that the Strouhal number for a flat plate is between 0.6 and 1.0. (Chen, 1996) For a flow velocity of 30 m/s, this indicates a vortex shedding frequency between 21 and 30 kHz. For a flow velocity of 100 m/s, this indicates a frequency between 70 and 100 kHz. In all cases, this analysis indicates extremely high frequency vortex shedding. Equation (5.10) suggests that, since vortex shedding frequency is inversely proportional to length, high vortex shedding frequencies may be a characteristic of micro-scale flows.

When these results are compared to figure 4.11, it becomes apparent that the natural frequency of the beam is below the excitation frequency of the flow. This suggests that the beam may be excited resonantly by vortex shedding. If this is true, the beam will vibrate, and possibly fail, regardless of the magnitude of the lift forces generated.

5.4.5. Airfoil Divergence

A final possible mode of failure is wing divergence. If the airfoil is at even a minimal angle of attack, a moment will develop on the airfoil from the pressure

distribution. If this moment is large enough, it will twist the airfoil, leading to a greater moment being generated on the airfoil, and possible failure.

To determine if this is a possibility for the airfoils being tested, we will assume that the pressure distribution on the bottom of the airfoil corresponds to the solution from Falkner-Skan Flow:

$$P(x) = \frac{\rho u_1^2 x^{2m}}{2} \tag{5.11}$$

where m is given by equation (2.68):

$$m = \frac{\beta}{2-\beta} \tag{2.68}$$

We will assume that the pressure on the top of the airfoil is ambient pressure. If this is correct, the moment on the airfoil will be given by the following integral:

$$M_z = \int_0^L (x - \frac{L}{2}) P(x) dx \tag{5.12}$$

Using the pressure distribution from (5.11), the integral can be evaluated to obtain

$$M_z = \frac{\rho u_1^2 L^{2m+2}}{4} \left[\frac{\mathrm{m}}{(\mathrm{m}+1)(2\mathrm{m}+1)} \right] \tag{5.13}$$

This result must be compared with the airfoil twist as a function of the applied movement.

The beam twist angle Φ(z) is given by equation (5.14) (Ugural, 1995)

$$\phi(z) = \frac{M_z \left(Lz - z^2 \right)}{2GJ} \tag{5.14}$$

where G is the Modulus of Elasticity in shear, and J is the polar moment of inertia:

$$J = \frac{tc\left(t^2 + c^2\right)}{12} \tag{5.15}$$

The maximum beam twist will be at the center of the airfoil. Equation (5.16) gives the distributed moment along the airfoil required to reach any given twist angle:

$$M = \frac{8\phi_{\max} GJ}{S^2} \tag{5.15}$$

For the airfoil cross-section, and the mechanical properties of silicon, the required moment to reach a twist angle is shown in figure 5.20. The expected moments generated by the fluid flow at these angles of attack are plotted for 2 cases: 100 m/s at 1.0 atmosphere, and 30 m/s at 0.1 atmosphere.

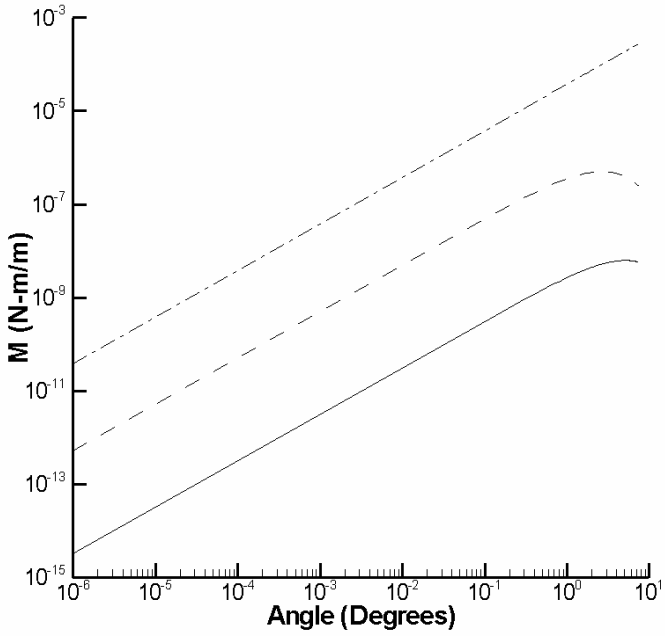

Figure 5.20. Airfoil Twisting Moment as a Function of Angle

Figure 5.20 shows that the moments generated by aerodynamic forces at any angle of attack are orders of magnitude below those required to keep the center of the airfoil twisted to that angle. Based on this, airfoil divergence can be ruled out as a failure mode.

5.4.6. Additional Testing Attempts

Attempts were also made to mount 125 micron titanium wire in place of the airfoil for use in testing. However, the epoxy required to mount these in place resulted in reduction the sensitivity of the force sensors to the point where it was indistinguishable from the system noise. A weight of 0.5 g, or approximately 5 mN, failed to produce a reliably detectable signal, and this approach to testing was not continued.

5.5. Conclusions

The technology developed for release of long micro-structures in Chapter 4 was used to create an integrated micro-device, with the theoretical ability to sense forces in both the x and y directions. The airfoil device was successfully released within the tunnel facility described in Chapter 3.

However, the fragility of the device made it impossible to use for actual testing. Several possible explanations exist. The most likely explanations are that the airfoil is being subjected to unexpected aerodynamic forces in the y-direction, or that the airfoil is excited into resonance by vortex shedding. Without a greater understanding of transient flow in the slip flow regime, it is difficult to evaluate these possibilities in more detail.

CHAPTER 6

CONCLUSIONS AND FUTURE WORK

6.1. Conclusions

This thesis made three major contributions to the scientific literature relevant to micro-flight. First, the governing equations for a boundary layer with slip flow were derived and solved. Second, a low-pressure, low turbulence facility for testing of micro-machined airfoils was developed. Finally, a fabrication process for micro-machined beams with micro-scale cross sections, and meso-scale spans, was developed. Each of these is discussed in more detail.

6.1.1. Boundary Layer Scaling in the Rarefied Flow Regime

This thesis began with an effort to develop scaling laws for predicting the breakdown of equilibrium gas dynamics in flow over a flat plate. The results of this study showed that the Blasius boundary layer solution could be modified to incorporate non-equilibrium effects. Previous work had attempted to incorporate these effects as a perturbation on the no-slip solution, showing no changes in skin friction or heat transfer.

The boundary layer equations were re-formulated, incorporating a non-equilibrium parameter K_1. After re-formulating the equations, the equations were solved numerically using a boundary layer solver. The results show that both skin friction and heat transfer will decrease as a result of non-equilibrium effects. Equally interesting, the self-similar structure of the laminar boundary layer will disappear.

The scaling laws developed for the Blasius solution could also be applied to Falkner-Skan flow over a wedge. These results show that as the angle of attach increases, the decreases in skin friction and heat transfer due to slip become more significant. They also show that, for stagnation flow, the self-similarity of the no-slip case is recovered.

6.1.2. Development of a Low-Turbulence, Low-Pressure Wind Tunnel

Testing in the flow regimes where these effects appear required simultaneous development of a specialized test facility and an integrated micro-airfoil and force sensor. The need to test airfoils with a span of around 1 cm, with minimal sidewall effects, led to the development of a tabletop wind-tunnel facility. A 100-1 contraction section was selected to give low turbulence. Based on computational fluid dynamics results, an extremely short contraction section was selected, and used in the tunnel. The resultant design gave uniform flow over a range of pressures from 0.15 to 1.0 atmospheres, and flow velocities from 30 to 100 m/s, or a range of 2 orders of magnitude of Reynolds numbers.

These results demonstrate that variable-pressure testing can be used at low Reynolds numbers. They also show that a 100-1 contraction for a wind-tunnel can be used where space allows, expanding the range of possible tunnel designs.

6.1.3. Fabrication of Micro-Machined Airfoil Structures

An integrated micro-device, with a 1 cm span airfoil and piezoresistive force sensors, was designed and fabricated. The major challenge in design of the integrated micro-device was creating a long beam structure, and integrating the fabrication process with placement in the tunnel. The ability to create structures with micro-scale cross-sections, and meso-scale lengths, required extensive analysis of the structural constraints. Based

on this analysis, a fabrication process was designed to allow fabrication and installation of test structures. Test structures were created with thicknesses on the order of microns, and spans of up to 1 cm. This allowed fabrication of the integrated device to proceed. The structures obtained from this process are unique in incorporating a micro-scale cross section with a meso-scale span.

6.1.4. Limitations on Testing

However, the test structures broke under extremely light aerodynamic loads, and during calibration. Because of this, aerodynamic tests could not be conducted using the designed force sensors. Based on the analysis presented in chapter 5, the most likely explanation for the failure is vortex shedding.

There is no obvious fix for this. Thickening the test structures would increase aerodynamic loading, as vortex shedding would occur. For future work, we suggest that the airfoil and the tunnel both be downsized by a factor of 2, which would increase the level of complexity of the tests. The airfoil thickness should be increased to 50 microns or larger. We also suggest that extensive simulation of the airfoils be conducted with a code incorporation both unsteady and equilibrium effects in the planning of future experiments. The tunnel itself should be tested for flow in the tangential direction that may not have previously been tested. Finally, we suggest that any future tunnel be designed with the ability to pump down to low pressures very slowly, to minimize forces on the airfoil.

6.2. Impacts of Downsizing Tunnel

Halving the span of the tunnel will improve the strength of the airfoils by a factor of four, based on the structural constraints outlined in Chapter 4. However, validating the

revised tunnel will increase in complexity. The smaller scale of the tunnel will require non-intrusive optical measurements, such as particle image velocimetry, to be used. This will require that the test section be made of materials that are both optically transparent, and chemically resistant, such as glass. This will require large changes to the test section design.

It will also require that a method for seeding the flow be installed. Additional validation of the PIV system will be required to ensure correct operation at low pressures, since the seed particles may have Knudsen numbers in the slip regime. PIV seed particles used in imaging of micro-fluidic systems are typically 1-20 microns. (Santiago, 1998). At a pressure of 0.1 atm, this would give a Knudsen number based on diameter of 0.05-1.0, meaning the particles themselves would be subject to non-equilibrium effects.

6.3. Re-thinking Micro-scale flight: Structural limitations

The results of the failure analysis in Chapter 5 suggest that structural concerns, instead of fluid mechanics based concerns, may place a lower limit on micro-flight. If we assume that thickness and wingspan both scale with a characteristic length L, then equation (5.9) becomes:

$$C_L\big|_{max} \propto \frac{L^2 \sigma_{yield}}{\rho U^2} \tag{6.1}$$

While we expect the velocity U to decrease as we go to smaller scales, it is unlikely to decrease in a manner directly proportional to L. Therefore, equation (6.1) suggests that we cannot directly scale down structures for micro-scale flight. Instead, wings, whether flapping or fixed, must become relatively stubbier and thicker. Such wings would be heavier and less efficient, which would have consequences for the entire air

vehicle. While development of a complete scaling law for allowable dimensions of micro-scale flight goes beyond the immediate scope of this thesis, we suggest that investigating structural loading on insect flight may provide a starting point for understanding this issue.

6.4. Additional Future Work

Because it is not clear that future experiments could be conducted, the potential uses of the work done in this thesis outside of non-equilibrium fluid mechanics should be considered. The scaling developed for the flat-plate laminar boundary layer may be expandable to cover a much wider array of laminar slip flows. These solutions should be investigated in greater depth for the insight they may provide, not only into micro-scale flows, but also into flight mechanics in the upper atmosphere.

The tunnel developed for this experiment is extremely specialized, and it is unlikely that an identical facility will be needed for future work. However, some of the lessons learned in its design may be applied to the design of other experimental facilities. The CFD design work, as well as the experimental validation, shows that an extremely high contraction ratio is feasible for use in low-Reynolds number test facilities. This result may be useful in future tunnel design.

The methodology for low-pressure testing should also be developed in greater depth. As the interest in micro- and nano-scale fliers grows, understanding flow phenomena at small scales will become more important. Theoretically, testing at low pressures allows a test to be conducted at a length scale ten times that of conventional testing. This may allow the scaling up of models of insect flight in ways that improves flow visualization, allowing new insights into the mechanism of insect flight. This represents a reversal of

the trends of 100 years of wind-tunnel testing, where the objective was to test large objects, such as aircraft, at smaller scales.

The ability to rapidly contract, and accelerate, low Reynolds number flows into a uniform stream without separation, or inducing turbulence, may be useful in micro-fluidics. The ability to move samples without the dispersion and shear stress introduced by the parabolic velocity profiles of channel flows is one of the reasons for the popularity of electro-kinetics in microfluidics. Being able to achieve a similar profile in pressure-driven flows may be a useful tool in sample handling.

The fabrication process used in this thesis are extremely specialized, but may have applications in the creation of micro-machined hot-wire anemometers and other small scale micro-structures. However, without a more complete understanding of why the devices are failing, it is difficult to recommend use of this process.

REFERENCES

Arkilic, E. B. (1997) Measurement of the Mass Flow and Tangential Momentum Accomodation Coefficient in Silicon Micromachined Channels. *Ph.D. Thesis*, MIT, Cambridge.

Balakrishnan, R., Agarawl, R., and Yun, K. (1999). BGK-Burnett equations for flow in the continuum-transition regime. Journal of Thermophysics and Heat Transfer. Vol. 13(4), pp. 397-410.

Baldwin, L., Sandborn, V., and Laurence, J. (1960). Heat Transfer from Transverse and Yawed Cylinders in Continuum, Slip, and Free Molecule Air Flows. Journal of Heat Transfer. Vol. 82(2), pp. 77-88.

Batchelor, G. K. (1953) *Theory of Homogenous Turbulence*. Cambridge University Press, Cambridge.

Baysal, O., and Aslan, R. A.. (2002) Computing Separated Flows in MEMS Devices, ASME Paper FEDSM2002-31157

Bayt, R. (1999) Analysis, fabrication and testing of a MEMS-based micro-propulsion system. *Ph.D. Thesis*, MIT, Cambridge.

Bird, G. A. (1994) *Molecular Gas Dynamics and the Direct Simulation of Gas Flows*. Clarendon Press, Oxford.

Blasius, H. (1908) Grenzschichten in Flüssigkeiten mit kleiner Reibung. Zeitschrift für Mathematik und Physik. Vol. 56, pp. 1-37

Breuer, M., Bernsdorf, J., Zeiser, T., Durst, F. (2000) Accurate computations of the laminar flow past a square cylinder based on two different methods: lattice-Boltzmann and finite-volume. International Journal of Heat and Fluid Flow. Vol. 21(2), pp. 186-196.

Brugger, J., Buser, R. A., de Rooji, N. F. (1992) Silicon cantilevers and tips for scanning probe microscopy. Sensors and Actuators A Vol 34, pp. 193-199.

Cai, C., Boyd, I. D., and Candler, G. V. (2000) Direct Simulation Methods for Low-Speed Microchannel Flows. Journal of Thermophysics and Heat Transfer, Vol. 14(3), pp. 368-378.

Chambers, B., and Lee, T. T. (1997), A numerical study of local and average natural convection Nusselt numbers for simultaneous convection above and below a uniformly heated horizontal thin plate. Journal of Heat Transfer, Vol. 119(1) , pp. 102-108.

Chen, J. M., and Fang. Y. C. (1996) Strouhal numbers of inclined flat plates. Journal of Wind Engineering and Industrial Aerodynamics, Vol 61, pp. 99-112.

Chui, B. W., Kenny, T. W., Mamin, H. J., Terris, B. D., and Rugar, D. (1998) Independent Detection of Vertical and Lateral Forces with a Sidewall-Implanted Dual Axis Piezoresistive Cantilever. Applied Physics Letters. Vol. 72 (11), pp.1388-1390.

Clausius, R. (1857) Ueber die Art der Bewegung welche wir Wärme nennen. Annalen der Physik Vol. 100, pp. 353-380.

Diez F. J., and Dahm W.J.A., (2004), Design and fabrication of unsteady electrokinetic microactuator arrays for turbulent boundary layer control. Journal of Micromechanics and Microengineering. Vol.14 (10) pp. 1307-1320.

Ellington, C. P. (1999) The Novel Aerodynamics of Insect Flight: Applications to Micro-Air Vehicles. Journal of Experimental Biology. Vol. 202 (23), pp. 3439-3448.

Epstein, A.H., Senturia, S.D., Al-Midani, O, Anathasuresh, G., Ayon, A., Breuer, K., Chen, K-S, Ehrich, F.E., Esteve,E., Frechette, L., Gauba, G., Ghodssi, R., Groshenry, C., Jacobson, S., Kerrebrock, J.L., Lang, J.H., Lin, C-C., London, A., Lopata, J., Mehra, A., Mur Miranda, J.O., Nagle, S., Orr, D.J, Piekos,.E., Schmidt, M.A., Shirley, G., Spearing, S.M., Tan, C.S., Tzeng, Y-S and Waitz, I.A. (1997) "Micro-Heat Engines, Gas Turbines, and Rocket Engines- the MIT Microengine Project" AIAA Paper 97-1773.

Erbacher, C., Bessoth, F. G., Busch, M., Verpoorte, E., Manz, A., (1999) Towards Integrated Continuous-Flow Chemical Reactors. Mikrochimica Acta, Vol. 31(1-2), pp. 19-24.

Falkner, V.M., and Skan, S. W. (1931) Solutions of the boundary-layer equations. Philophical Magazine, Vol. 12 (80): 865-896.

Feynmann, R. P. (1992) There's Plenty of Room at the Bottom. Journal of Micromechanics and Microengineering, Vol. 1(1), pp. 60-66.

"FLUENT/UNS user's guide. Release 3.2". (1995) Fluent, Inc., Lebanon, N. H.

Fréchette, L. G., Jacobson, S. A., Breuer, K. S., Ehrich, F. F., Ghodssi, R,, Khanna, R., Wong, C. W.. Zhang, X., Schmidt, M. A., and Epstein, A. H. (2005) High-speed microfabricated silicon turbomachinery and fluid film bearings . Journal of Microelectromechanical Systems, Vol. 14 (1). pp. 141-152

Gad-el-Hak, M. (2001) The Fluid Mechanics of Microdevices- The Freeman Scholar Lecture. Journal of Fluids Engineering, Vol. 121(1), pp. 5-33.

Gaede, W. (1913). Die äubere reidbung der gase. Annaken der Physikm Vol 41, pp. 289.

Gallis, M. A., and Torcynski, J. R. (2004) An Improved Reynolds-Equation Model for Gas Damping of Microbeam Motion. Journal of Microelectromechanical Systems, Vol. 13(4), pp. 653-659.

Gambert, B. (1978) Low Reynolds Number TAC-Slip Flow Past a Circular Cylinder. Proceedings, 11th Rarefied Gas Dynamics Symposium.

Harley, J. C., Huang, Y., Bau, H. H., and Zemel, J. N. (1995) Gas flow in micro-channels. Journal of Fluid Mechanics. Vol. 284, pp. 257-274.

"High Accuracy Instrumentation Amplifier AMP02" (2003) Analog Devices, Norwood, MA

Ho, C. M., and Tai, Y. C. (1998) Micro-Electro-Mechanical Systems (MEMS) and Fluid Flows. Annual Review of Fluid Mechanics, Vol. 30, pp. 579-612.

Ho, S., Nassef, H., Pornsin-Sirirak, T. N., Tai, Y. C., and Ho, C. M. (2003). Unsteady Aerodynamics and Flow Control for Flapping Wing Flyers. Progress in Aerospace Science, Vol. 39(8), pp. 635-681.

Holman, J. P. (1984) *Experimental Methods for Engineers*. McGraw-Hill, New York.

Hu, D., Tung, Y. C. Wei, H. H. Grotberg, J. B., Skerlos, S. J., Kurabayashi, K., Takayama, S. (2002) Use of Air-Liquid Two-Phase Flow in Hydophobic Microfluidic Channels for Disposable Flow Cytometers. Biomedical Microdevices, Vol. 4(2), pp. 141-149.

Incropera, F. P., and DeWitt, D. P. (2001) *Introduction to Heat Transfer*. Wiley and Company, New York.

Kaplan, C. R. and Oran, E. S. (2002). Nonlinear Filtering for Low-Velocity Gaseous Microflows. AIAA Journal. Vol. 40(1), pp. 82-90.

Karnidakes, G. E., and Beskok, A. (2002) *Microflows*. Springer, N. Y.

Khaled, A., and Vafai, K. (2004) The effect of the slip condition on Stokes and Couette flows due to an oscillating wall: exact solutions. International Journal of Non-Linear Mechanics. Vol 39(5), pp. 795-809.

Knudsen M. (1909) Die Gesetze der molecular Stromung und die inneren Reibungstromung der Gase durch Rohren. *Ann. Phys. (Leipzig)* Vol. 28:75-130

Kogan, M. N., (1969) *Rarefied Gas Dynamics*, Plenum Press, New York, 1969.

Kundt, A., and Warburg, E. (1875) Über Reibung und Wärmeleitung verdünnter Gase (On friction and heat conduction of diluted gases), Annalen der Physik Vol. 155, 337

Lee, W., Wong, M. and Zohar, Y. (2002) Pressure Loss in Constriction Microchannels. Journal of Microelectromechanical Systems, Vol. 11(3), pp. 236-244.

Lefebvre, A. H., (1998). *Gas Turbine Combustion*, Taylor & Francis Group, Philadelphia, PA

Lin, T. C., and Schaaf, S. A., (1951), Effect of Slip on Flow Near a Stagnation Point and in a Boundary Layer, NACA Technical Note 2568, Washington, DC.

Liu, V. C. (1959) On the Drag of a Flat Plate at Zero Incidence in Almost-Free Molecule Flow. Journal of Fluid Mechanics. Vol. 5, pp. 481-496.

Lumley, J. L, and McMahon, J. F. (1967) Reducing Water Tunnel Turbulence by Means of a Honeycomb. Journal of Basic Engineering, Transactions of the ASME, Series D. Vol 89D(4), pp. 754-770.

Lempert, W. R., Jiang, N., Sethuram, S. and Samimy, M., 2002, Molecular Tagging Velocimetry Measurements in Supersonic Micro Jets, AIAA Journal, 40(6), pp. 1065-1070.

Madou, M. (1997) *Fundamentals of Microfabrication*, CRC Press, New York.

Maxwell, J. C., (1879) On Stresses in Rarefied Gases Arising from Inequalities of Temperature, Philosophical Transactions of the Royal Society of London, Vol. 170, p. 231-256.

Maxwell, J. C. (1965) *The Scientific Papers of James Clerk Maxwell.* Dover Publications, Inc. New York.

McMichael, J. M. and Francis, M. S. (1997) Micro Air Vehicles- Towards a New Dimension in Flight. DARPA, Washington.

Meinhart, C. D., and Zhang, H. (2000) The Flow Structure Inside a Microfabricated Inkjet Printer Head. Journal of Microelectromechanical Systems, Vol. 9(1), pp. 67-75.

Millikan, R. A. (1923) Coefficients of Slip in Gases and the Law of Reflection of Molecules from the Surfaces of Solids and Liquids. Physical Review, Vol. 21(3), pp. 217–238

Meinhart, C., Wereley, S., and Santiago, J. (1999). PIV measurements of a microchannel flow. Experiments in Fluids Vol 27(5), pp. 414-419.

Miki, N., Shimoyama, I.; (2002) Dynamics of a microflight mechanism with magnetic rotational wings in an alternating magnetic field. Journal of Microelectromechanical Systems, Vol. 11(5), pp.584-591

Mikhail, M. N., and Raibird, W. J. (1978) Optimum Design of Wind Tunnel Contractions. AIAA Paper 1978-819.

Miura, H. (1983) Slip-Flow of a Viscous-Fluid Past an Inclined Flat-Plate, Journal of Engineering Mathematics, Vol. 17(1): pp. 41-53.

Miyagi, T. (1964) Oseen Flow Past a Flat Plate Inclided to a Uniform Stream. Journal of the Physical Society of Japan, Vol. 19 (6): pp. 1063-& 1964

Panton, R. (1996) *Incompressible Flow*. Wiley, New York.

Peterson, K. E. (1982) Silicon as a Mechanical Material. Proceedings of the IEEE, Vol. 70(5), pp. 420-457.

Pong, K., Ho, C., Liu, J., and Tai, Y. C. (1994) Non-linear pressure drop in uniform microchannels. In *ASME, FED- Vol. 197, Application of Microfabrication to Fluid Mechanics*, pp. 51-56.

Raccurt, O., Tardif, F., Arnaud d'Avitaya, F., and Vareine, T. (2004) Influence of liquid surface tension on stiction of SOI MEMS. Journal of Micromechanics and Microengineering, Vol. 14(7), pp. 1083-1090..

Roylance, L. M., and Angell, J. B. (1979) A batch-fabricated silicon accelerometer. IEEE Trans. Electron Devices, vol. ED-26, pp.1911-1917.

Santiago, J. G., Wereley, S. T., Meinhart, C. D., Beebe, D. J., and Adrian, R. J., (1998) A particle image velocimetry system for microfluidics. Experiments in Fluids, Vol 25(4), pp. 316-319.

Scavazze, K. (2003) *Summer Research Report*, University of Michigan, Ann Arbor.

Schaaf, S. A., and Sherman, F. S. (1954) Skin Friction in Slip Flow. Journal of Aeronautical Sciences. Vol. 21, pp. 85-90.

Senturia, S. (2000) *Microsystem Design*, Kluwer Academic Publishers, New York.

Smith, C. S. (1954) Piezoresistive effect in germanium and silicon. Physical Review, Vol. 94, pp. 42-49.

Sun, Q. and Boyd, I.D., (2004) Flat-Plate Aerodynamics at Very Low Reynolds Number. Journal of Fluid Mechanics, Vol. 502, 199-206.

Sun, Q., Boyd, I. D., and Candler, G. V., (2004) A hybrid continuum/particle approach for modeling subsonic, rarefield gas flow. Journal of Computational Physics, Vol. 194 (1), pp. 256-277.

Sun, Q. (2003) "Information Preservation Methods for Modeling Micro-Scale Gas Flows", Ph.D. dissertation, University of Michigan.

Sunada, S., Sakaguchi, A., and Kawachi, K, (1997) Airfoil Section Characteristics at a Low Reynolds Number. Journal of Fluids Engineering, Vol. 119(1), pp. 129- 135.

Sze, S. M. (1994) *Semiconductor Sensors*. John Wiley and Sons, New York.

Timiriazeff, A., (1913) The inner attrition of thinned gas and on the connection of the shearing strain and of the temperature on the limitations between metals and gas, Annalen der Physik Vol. 40, pp. 975-995

Uberoi, M. S. (1956) Effect of Wind-Tunnel Contraction on Free Stream Turbulence. Journal of the Aeronautical Sciences, Vol. 23(8), pp. 754-764.

Ugural, A. C., and Fenster, S. K. (1995) *Advanced Strength and Applied Elasticity*. Prentice Hall PRT, New York.

Waits C.M., Modafe A., Ghodssi R. (2003). Investigation of gray-scale technology for large area 3D silicon MEMS structures. Journal of Micromechanics and Microengineering. Vol. 13(2), pp. 170-177

Wang, C. Y. (2002) Low Reynolds Number Slip Flow in a Curved Rectangular Duct. Journal of Applied Mechanics, Vol. 69(2), pp. 189-194.

Wang, Z. J. (2005) Dissecting Insect Flight. Annual Review of Fluid Mechanics, Vol. 37, pp. 183-210.

White, F. M, (1991) *Viscous Fluid Flow*. McGraw-Hill, Inc. New York.

Yang, J. M., Ho, C. M., Yang, X., and Tai, Y. C. (2001) Micromachined Particle Filter with Low Power Dissipation. Journal of Fluids Engineering, Vol. 123(4), pp.899-908.

Yazdi, N., Ayazi, F., and Najafi, K. (1998) Micromachined Inertial Sensors. Proceedings of the IEEE, Vol. 86 (8), pp. 1640-1659.